Self-Triggering of Radio Signals from Cosmic Ray Air Showers

Zur Erlangung des akademischen Grades eines
Doktors der Naturwissenschaften
von der Fakultät für Physik der
Universität (TH) Karlsruhe

genehmigte

Dissertation

von

Dipl. Phys. Thomas Asch
aus Herrenberg

Tag der mündlichen Prüfung: 07. November 2008
Referent: Prof. Dr. H. Gemmeke
Korreferent: Prof. Dr. J. Blümer

Abstract

LOPES$^{\mathrm{STAR}}$ is a prototype detector for future experiments on the observation of radio emission of ultra high energy cosmic rays. Absolutely calibrated measurements of the electric field strength with the LOPES$^{\mathrm{STAR}}$ detector were performed in coincidence with the well-established air shower detector KASCADE-Grande. The experimental configuration allowed a simultaneous observation of east-west and north-south polarised components of the electric field per antenna used.

This thesis discusses in detail the influence of background sources on the detector configuration as well as the resulting self-trigger system. The implemented trigger suppresses strong background signals from the industrial environment on the site of the Forschungszentrum Karlsruhe (rejection $> 99.9\,\%$) and is the basis for a hardware self-trigger. Therefore, the system is adequate for any other detector site.

Two different calibration methods are performed and cross-checked to convert the measured raw data into an electric field strength. Both methods result in the same frequency dependent calibration values within their uncertainties. Furthermore, the analysis of the radio emission of ten high quality shower events results in the most probable scale parameter of $d_0 = (137 \pm 18)\,\mathrm{m}$. The comparison of selected events with Monte Carlo simulations on an event-by-event basis points out a good correspondence within the given uncertainties and confirms the geosynchrotron model. The overall angular resolution of the arrival direction results in only a few degrees. The presented methods and algorithms are developed for the trigger system and the analysis and are now standard tools for the data analysis in the LOPES collaboration.

Zusammenfassung

Triggersystem für Radiosignale aus kosmischer Strahlung

Das LOPES$^{\mathrm{STAR}}$ Experiment ist ein Prototyp Detektor für zukünftige Experimente zum Nachweis der Radioemission aus Luftschauern der höchsten Energien. Im Vordergrund stehen dabei die Entwicklung und Optimierung eines unabhängigen Triggersystems für Radiosignale, eine absolute Kalibration des Messaufbaues sowie ein besseres Verständnis der Korrelation zwischen Radiosignalen und rekonstruierten Schauergrößen etablierter Luftschauerexperimente.

Zu diesem Zweck wurden 10 logarithmisch-periodische Dipolantennen auf der Fläche des bewährten Luftschauerexperimentes KASCADE-Grande installiert. Jede Antenne detektiert gleichzeitig die Nord-Süd und die Ost-West polarisierte Komponente des elektrischen Feldes in einem Frequenzbereich von $40-80\,\mathrm{MHz}$. Die Positionen der Antennen auf dem Gelände des Forschungszentrums Karlsruhe bilden die Punkte eines gleichseitigen Dreiecks, welches zur Richtungsbestimmung durch Triangulation benutzt wird. Alle Antennen bedecken zusammen eine Fläche von ungefähr $300 \times 350\,\mathrm{m}^2$ und sind in zwei Gruppen mit vier Antennen und einer weiteren Gruppe mit zwei Antennen organisiert. Ein von KASCADE-Grande gesendetes Signal startet automatisch die Datenauslese aller 10 Antennen, falls ein Luftschauer mit einer Energie $E > 10^{16}\,\mathrm{eV}$ detektiert wurde. Gleichzeitig werden die Eigenschaften der Sekundärteilchen bis zu einer Energie von $E < 10^{18}\,\mathrm{eV}$ am Erdboden von KASCADE-Grande auf einer Fläche von $700 \times 700\,\mathrm{m}^2$ nachgewiesen.

Zusätzlich wurde ein identischer Messaufbau mit drei Antennen im Rahmen des Pierre Auger Observatoriums in Argentinien installiert, um die dort vorherrschenden Untergrundeffekte und Umwelteinflüsse zu untersuchen. Es zeigte sich, dass die typischen Untergrundeffekte im Mittel eine Größenordnung im Amplitudenspektrum geringer ausfallen als auf dem industriell geprägten Gebiet des KASCADE-Grande Experimentes. Das Pierre Auger Observatorium bedeckt eine Fläche von ungefähr $3000\,\mathrm{km}^2$ und bietet damit ideale Bedingungen für ein großflächiges Antennenfeld zur kontinuierlichen Detektion der Radioemission aus Luftschauern bei Energien über $10^{18}\,\mathrm{eV}$.

Die Entwicklung und Optimierung einer Strategie zur Selbsttriggerung für Radiosignale wurde auf Basis von extern getriggerten Daten von KASCADE-Grande in Software realisiert. In einem ersten Schritt wurden die transienten Störsignale von technischen Anlagen sowie kontinuierliche Radio und TV Signale, die mit dem Messaufbau detektiert werden, analysiert und charakterisiert. Das entwickelte System zur Selbsttriggerung unterdrückt dabei durch plausibel motivierte Parameter Störsignale innerhalb einer Polarisationsrichtung. Die akzeptierten Radiosignale aus Luftschauern und Untergrundsignale werden unter Ausnutzung der geometrischen Anordnung der Antennen (Koinzidenzbedingung) weiter separiert. Radiosignale aus sehr geneigten Luftschauern (Zenitwinkel $\theta > 60°$) sowie zivilisationsbedingte Störungen werden auf diese Weise unterdrückt.

Nach Anwendung des implementierten Selbsttriggers auf den ausgewählten Datensatz ergibt sich eine Unterdrückung von Störsignalen von über 99,9 %. Für einen Energiebereich des Primärteilchens von $5 \cdot 10^{17}\,\mathrm{eV} < E < 10^{18}\,\mathrm{eV}$ ergibt sich die Effizienz zu über 90 %. Die Reinheit eines Datensatzes ist definiert als das Verhältnis der akzeptierten Schauerereignisse zu der Anzahl aller akzeptierten Ereignisse (Schauer- und Untergrundereignisse) und ergibt sich zu 6 %. Das Triggersystem zeigt eine gute Reduktion von Untergrundereignissen sowie eine gute Akzeptanz von Schauerereignissen unter den gegebenen Messbedingungen im Rahmen von KASCADE-Grande. Mit dieser Arbeit ist die Machbarkeitsstudie des vorgestellten Selbsttriggers erbracht.

Eine absolute Kalibration des Messaufbaues ist notwendig, um die Rohdaten in ADC-Werten in eine elektrische Feldstärke zu konvertieren. Dies bildet die Grundlage für die Verifikation der erzielten Resultate aus der Korrelationsanalyse. Zwei unabhängige Methoden wurden durchgeführt, um die absolute Kalibration des LOPES$^{\mathrm{STAR}}$ Detektors zu verifizieren. Zum einen wurden die charakteristischen Eigenschaften aller verwendeten Einzelkomponenten präzise im Labor vermessen und mathematisch so kombiniert, dass das Gesamtsystem beschrieben wird. Zum anderen wurde eine externe Referenzantenne benutzt, welche ein wohldefiniertes Signalspektrum emittiert. Ein entsprechender Vergleich der erzielten frequenzabhängigen Kalibrationskonstanten zeigte eine sehr gute Übereinstimmung beider Methoden innerhalb ihrer Fehlergrenzen. Der resultierende Gesamtfehler auf die gemessene Feldstärke kann damit zu $\sigma_{|\vec{E}|} = 7.2\,\%$ für das LOPES$^{\mathrm{STAR}}$ Experiment angegeben werden.

Die gewählte Nähe des LOPES$^{\mathrm{STAR}}$ Experimentes zum Luftschauerexperiment KASCADE-Grande bietet beste Voraussetzungen für Korrelationsanalysen. Es wurden strenge Bedingungen an die Qualität der Rekonstruktion von Schauerereignissen durch KASCADE-Grande und LOPES$^{\mathrm{STAR}}$ gestellt. Der resultierende Datensatz enthält zehn Schauerereignisse für weitere Untersuchungen.

Eine Parametrisierung des Radiosignals in Abhängigkeit der charakteristischen Größen eines Luftschauers erlaubt ein Vergleich der Ergebnisse verschiedener Experimente. Gleichzeitig kann für Einzelereignisse mit rekonstruierter Geometrie die Energie des Primärteilchens abgeschätzt werden. Unter Berücksichtigung beider Polarisationsrichtungen (Nord-Süd und Ost-West) wurde eine Parametrisierung der Radiosignale durchgeführt: in Abhängigkeit vom geomagnetischen Winkel α (Winkel zwischen Erdmagnetfeld und Schauerachse), der Energie des Primärteilchens E und dem lateralen Skalenparameter d_0. Aus den Untersuchungen folgt ein Skalenparameter von $d_0 = (137 \pm 18)\,\mathrm{m}$ und eine lineare Beziehung zur Energie des Primärteilchens (kohärente Radioemission).

Die Grenzen der Winkelauflösung werden durch verschiedene Faktoren, wie Zeitauflösung oder Abstand und Anzahl der genutzten Antennen, bestimmt. Der verwendete Aufbau erlaubt eine Bestimmung der Winkelauflösung auf zwei unterschiedliche Methoden. Bei der ersten Methode wird unter Annahme einer ebenen Schauerfront auch dieselbe Richtung für Schauerachse und Radiosignal angenommen. Es wird durch Triangulation die Richtung der Radiosignale bestimmt und die Differenz zur rekonstruierten Richtung von KASCADE-Grande gebildet. Daraus ergibt sich eine Winkelauflösung für den Azimutwinkel φ und Zenitwinkel θ von $\Delta\varphi \approx \Delta\theta \approx 7^\circ$ mit einer systematischen Verschiebung von $\Delta\varphi \approx 2^\circ$ und $\Delta\theta \approx -1^\circ$. Die zweite Methode nutzt künstlich erzeugte Störsignale, die Ähnlichkeit zu Radiosignalen aufweisen. Verworfene Untergrundsignale

mit einem Zenitwinkel $\theta \approx 90°$ werden benutzt, um die Häufigkeitsverteilung des Azimutwinkels zu untersuchen. Diese Methode kann dabei keine Aussage über die Winkelgenauigkeit des Zenitwinkels geben, da dieser als konstant angenommen wird. Setzt man voraus, dass die Quellen dieser schauerähnlichen Signale während der Messdauer weder ihre Position noch ihre Signalform ändern, dann erreicht man mit dem LOPES$^{\mathrm{STAR}}$ Detektor mit mindestens drei und höchstens vier Antennen eine Winkelauflösung von $\Delta\varphi \approx 0.6°$.

Eine weitere Untersuchung der Schauereigenschaften der gewählten zehn Schauerereignisse zeigt ein klares Defizit aus südlicher Richtung. Luftschauer aus dieser Richtung weisen einen geringen geomagnetischen Winkel auf und emittieren gemäß dem Geosynchrotron Modell, ein Modell zur Beschreibung der Radioemission aus Luftschauern, nur schwache Radiosignale.

Während der zur Verfügung stehenden Messdauer wurden zwei Luftschauer von allen zehn installierten Antennen detektiert. Diese Schauer wurden ausgewählt, um die Lateralverteilung auf Basis von Einzelereignissen mit deren Monte Carlo Simulationen zu vergleichen. Es zeigt sich hierbei eine gute Übereinstimmung mit dem Geosynchrotron Modell und den darauf aufbauenden Simulationen. Eine Ausnahme bilden dabei Signalen nahe der Schauerachse. Jedoch wird die Stärke der Radiosignale in den verschiedenen Polarisationen qualitative richtig reproduziert.

LOPES$^{\mathrm{STAR}}$ ist ein absolut kalibrierter Detektor für Radiosignale aus kosmischer Strahlung. Das vorgestellte Triggersystem unterdrückt transiente und kontinuierliche Störsignale und akzeptiert dabei Radiosignale aus Luftschauern. Zur Zeit wird im Rahmen von LOPES$^{\mathrm{STAR}}$ ein Hardwaretrigger in Betrieb genommen, welcher eine auf diese Elektronik angepasste Version des Triggersystems beinhaltet. Dieser wird zuerst auf dem Gelände des Forschungszentrums Karlsruhe und anschließend im Rahmen des Pierre Auger Observatoriums in einer Testumgebung mit drei Antennen installiert und verifiziert. LOPES$^{\mathrm{STAR}}$ bietet damit ideale Voraussetzungen, um dem Ziel eines Antennenfeldes in der Größe von mehreren zehn Quadratkilometern näher zu kommen. Dies ist notwendig, um den Effekt der Radioemission aus Luftschauern und deren Korrelation mit einer Vielzahl von Luftschauerparametern besser untersuchen zu können. Die in dieser Arbeit erzielten Ergebnisse werden im geplanten Radioexperiment im Rahmen des Pierre Auger Observatoriums umgesetzt und tragen dazu bei, das Geosynchrotron Modell zu verifizieren.

Contents

Chapter 1

Introduction

The discovery of cosmic rays is related to the balloon experiments of Victor Hess. He measured the altitude dependence of the discharge rate of electroscopes and detected that the intensity of ionising radiation rises with increasing height at about 1000 m above the ground. He concluded that the origin of this radiation is not from the Earth [Hess 12].

High energy cosmic rays initiate showers of secondary particles in the atmosphere of the Earth by interacting with the nuclei of air molecules. The secondary particles propagate through the atmosphere with a velocity almost close to the speed of light as a disc of particles. This phenomenon of extensive air showers was first understood and studied in detail by Pierre Auger and collaborators [Auge 39].

Many processes are related to the generation and development of extensive air showers. In particular, the emission processes in the radio frequency range of the lightest charged particles are of interest for this thesis as well as the establishing of new complementary detection techniques for high energy cosmic rays in astro-particle physics.

Radio pulses from cosmic rays were first experimentally discovered by Jelly and collaborators [Jell 65] and, were soon verified by several experiments in the late 1960s. In the following years the activities almost completely stopped due to difficulties with radio interferences, uncertainty about the interpretation of the results and the success of other detection methods (e.g. scintillator and fluorescence).

The observation of radio emission of extensive air showers is performed with the LOPES$^{\mathrm{STAR}}$ experiment by using an array of ten antennas at the location of the well-calibrated extensive air shower experiment KASCADE-Grande. This allows to perform coincident investigations on the properties of the shower particles and the radio emission. The LOPES$^{\mathrm{STAR}}$ antennas measure absolutely calibrated the north-south & east-west polarised components of the electric field. The configuration of the experiment combined with the benefit of KASCADE-Grande gives the possibility to develop a digital self-trigger system on the radio emission of cosmic rays.

Chapter 2 gives an introduction to extensive air showers and describes the processes of radio emission and their Monte Carlo simulations. An overview of the configuration of the experiment is presented in chapter 3. Two independent and consistent calibration methods are introduced and discussed in chapter 4. A detailed discussion about the requirements of a self-trigger system and the resulting strategy are presented in chapter 5. Finally, the parametrisation of the electric field strength and an event-by-event analysis are presented in chapter 6.

Chapter 2

High Energy Cosmic Rays

The investigation of cosmic rays is one of the most active fields in astro-particle physics. Origin, acceleration, and transport of the cosmic rays through interstellar and intergalactic space are not fully understood even 100 years after their discovery. Large detector arrays with high duty cycle and a combination of multiple detection techniques are needed to solve these open questions.

This chapter gives a brief introduction to the observed energy spectrum of cosmic rays and the mechanisms behind extensive air showers. Furthermore, the geosynchrotron model as a model of the emission of radio signals is described and discussed on the basis of Monte Carlo simulations.

2.1 Cosmic Ray Flux

Cosmic rays are primarily nuclei with kinetic energies covering 12 orders of magnitude from a hundred MeV to several hundred EeV. The integrated flux decreases strongly with increasing energy and spans more than 30 decades, so that numerous particles per $\mathrm{cm}^2 \cdot \mathrm{s}$ reach the Earth at low energies, but only one particle per km^2 and century at the highest energies.

The energy spectrum of the cosmic rays is almost featureless. Extending from $10^9\,\mathrm{eV}$ up to $10^{20}\,\mathrm{eV}$ the spectrum follows a power law $E^{-\gamma}$ with a spectral index of $\gamma \approx 2.7$. In order to point out deviations from the power law fall off, the flux, shown in fig. 2.1, has been multiplied by $E^{2.5}$.

A power law fall off is expected in the case of stochastic acceleration of charged particles at astrophysical shocks as proposed by Fermi [Ferm 49]. The Fermi mechanism works most efficiently in the case of diffuse shock acceleration when particles encounter the wave front of the shock several times. In addition, it explains the acceleration during supernova explosions, where material of several solar masses is ejected at a speed larger than the speed of sound in the interstellar medium and results in a strong shock wave that propagates radially. This acceleration mechanism combined with the propagation processes through the medium can qualitatively explain the whole energy range of the energy spectrum observed on Earth.

The two visible changes of the spectral index, shown in fig. 2.1, one at $E \approx 3 \cdot 10^{15}\,\mathrm{eV}$ [Kuli 59] and the other at $E \approx 4 \cdot 10^{18}\,\mathrm{eV}$ [Bird 93] are referred to within the astrophysics community as the *knee* and the *ankle* of the spectrum in analogy to the shape of a leg. All the spectral features might be interpreted as a change of the acceleration mechanism at the sources, as a propagation effect or as a change of the hadronic interaction cross section with increasing energy.

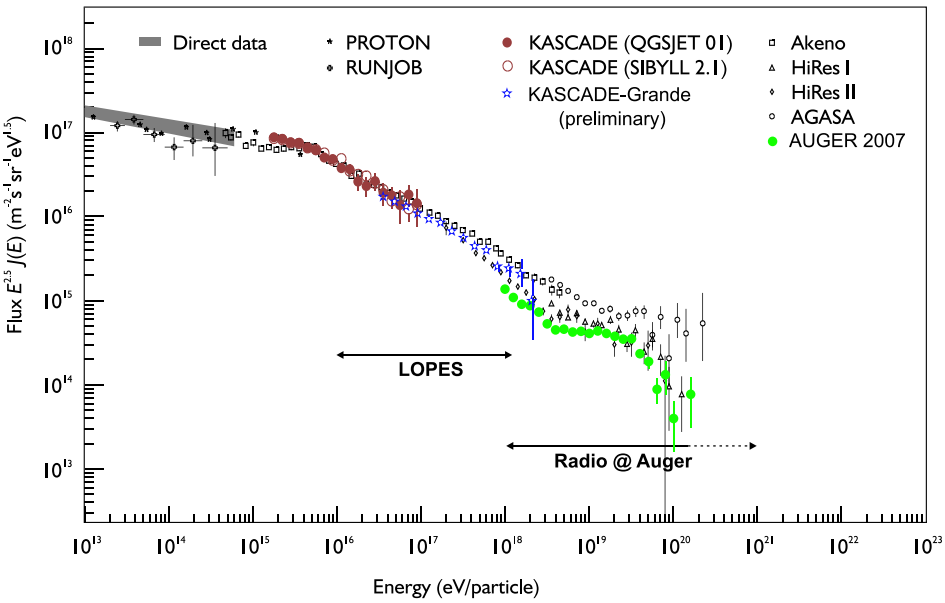

Figure 2.1: The flux of the cosmic rays is multiplied by $E^{2.5}$ to underline the features of the energy spectrum. The energy range of the LOPES experiment and the upcoming radio detector at the Pierre Auger Observatory are indicated by the arrows.

The knee might be considered to be an acceleration feature. The energy of the cosmic ray is proportional to the charge of the particle. The maximum energy that can be reached by Fermi shock acceleration follows $E_{\max} \approx b_s \cdot Z \cdot B \cdot L$, where b_s is the shock velocity, Z is the charge of the particle, B is the magnetic field strength, and L corresponds to the Larmor radius (radius of gyration). Thus, the knee is explained as a drop of the acceleration possibilities for different particles. Possible acceleration sites are supernova remnants.

The knee also might be interpreted as a propagation result due to a change in the regime of diffusion in the galactic magnetic field [Ptus 05, Cand 02]. The KArlsruhe Shower Core and Array DEtector (KASCADE) experiment has shown that the contribution to the flux from protons fall off earlier than from helium [Ulri 03].

Around 10^{17} eV there might be a second steepening of the spectral index observed — the *second knee* [Marc 05]. The experimental status does not allow to determine this energy well, but the KASCADE-Grande and the other experiments will clarify the characteristics of this energy range of the cosmic ray flux in the near future.

The ankle is a rise of the spectral index at energies above $4 \cdot 10^{18}$ eV. The experimental evidence is less strong than at lower energies due to the already very low particle flux and the large detection area needed. The most probable models assume that the extragalactic component then dominates the flux of particles and that the galactic component dies out, due to missing acceleration mechanisms in our galaxy. The position of the ankle would be the energy where the two components equally contribute to the total flux.

The last feature of the energy spectrum is a cut-off at energies above $5 \cdot 10^{19}$ eV and was independently predicted by Greisen [Grei 66] and Zatsepin & Kuz'min [Zats 66], the so-called GZK-effect. The energy of these cosmic rays is now high enough to interact

with the Cosmic Microwave Background (CMB) and they lose the main part of their energy due to the following interaction:

$$\begin{aligned} \gamma_{\mathrm{CMB}} + p \rightarrow \Delta^{+}_{1232\,\mathrm{MeV}} &\rightarrow \mathrm{n} + \pi^{+} \qquad (\mathrm{BR}\ 33\,\%) \\ &\rightarrow \mathrm{p} + \pi^{0} \qquad (\mathrm{BR}\ 66\,\%)\ (\mathrm{GZK\text{-}effect}) \end{aligned}$$

The numbers in brackets denote the approximated Branching Ratios (BR). The γ_{CMB} photons have a temperature of 2.7 K and fill up the universe as a uniform background radiation measured first by Penzias & Wilson [Penz 65].

Acceleration and propagation of cosmic rays at high energies is one of the puzzles that have not been yet solved in astro-particle physics. Up to energies of several 10^9 eV they are of solar origin, but above this energy due to the maximum acceleration power in the Sun and the leakage of day-night variations of the measured flux, they must have another source outside of the solar system.

The first evidence that cosmic ray particles were charged was given by east-west asymmetries caused by their deflection in the magnetic field of the Earth. Up to energies of a few 10^{18} eV the arrival directions are completely isotropic. The cosmic rays of the highest energies are affected by galactic and extragalactic magnetic fields. Only above an energy of 10^{18} eV, particles cannot be confined by the $\approx 3\,\mu$G magnetic field of our galaxy anymore and tracking back these particles might be possible. Their arrival direction and origin might be reconstructed depending on the intergalactic magnetic fields and the distance to the source, due to the fact that the deflection angle is less than 5° for nearby astrophysical objects assuming particle energies of approximate 10^{19} eV.

The explanation of sources of ultra high energy cosmic rays has a long history. Even before the sources were identified, it was assumed that nearby radio galaxies, which contain Active Galactic Nuclei (AGN) were very good accelerating sites. AGN are supermassive black holes with a mass 6 orders of magnitude larger than the solar mass. In the region close to the black hole a big amount of matter is accreted and parts of it are released in the form of jets. The maximum energy that might be reached in these astrophysical objects is 10^{21} eV [Bier 87]. The acceleration sites for the ultra high energy cosmic rays can be interpreted as a beam dump: Where the jet hits an intergalactic cloud of matter from galaxies or the region very close to the black hole or even in remnants of the fossil jets of old AGNs.

2.2 Extensive Air Showers

In analogy to a fixed-target experiment one can consider the atmosphere acting as a (inhomogeneous) calorimeter and the incoming cosmic rays as the beam particles. At large altitudes the depth of penetration of the first interaction strongly fluctuates due to the low density of the atmosphere. The electromagnetic cascade initiated in the first interactions from the pion ($\pi^{\pm}, \pi^{0}$) and kaon ($\mathrm{K}^{\pm}, \mathrm{K}^{0}$) decays is important for the detection of the radio emission of cosmic rays.

Heitler developed a simple cascading model for the electromagnetic component ($e^{\pm}$ and γ particles) [Heit 49]. It describes the main characteristics by the development of an extensive air shower and is introduced here for simplification.

The energy of the primary particle E_0 is larger than the critical energy E_c, which is needed to interact with the particles in the atmosphere. The basic processes are bremsstrahlung and pair production. Two particles always result from one interaction and in addition, it is assumed that both particles are equal in energy. After a number of interactions n the total number of particles corresponds to 2^n with an energy per particle of $E_0/2^n$. One interaction occurs after a splitting length of $\lambda = X_0 \ln 2$, where X_0 is the radiation length for air. The maximum number of interactions is proportional to $\ln(E/E_c)$. The air shower develops and reaches its maximum at an atmospheric depth of $X_{\max} = \lambda \log_2(E_0/E_c) \propto \ln(E_0)$ with the maximal number of particles $N_{\max} = E_0/E_c$ [Stan 04].
Note: The electromagnetic radiation length in the air corresponds to $X_0 \approx 37\,\mathrm{g/cm^2}$.

At the atmospheric depth $X_{\max}$ the shower development reaches a maximum for the number of particles $N_{\max}$ and afterwards the number exponentially decreases due to bremsstrahlung and ionisation loses. The longitudinal shower development can be described by the parametrisation by Gaisser-Hillas [Gais 77]:

$$N(X) = N_{\max} \cdot \left(\frac{X - X_0}{X_{\max} - X_0} \right)^{\frac{X_{\max} - X_0}{\lambda}} \cdot \exp\left(\frac{X_{\max} - X}{\lambda} \right)$$

This parametrisation describes the number of particles N in dependence on the atmospheric depth X. The two parameters, $X_{\max}$ and λ, result from a fit to the shape of the shower front.

The distribution in the atmosphere of the secondary particles form up an extensive air shower that is described by three main components: Electromagnetic (e^+, e^- and γ), muonic (μ^+ and μ^-), and hadronic (mainly: $\pi^\pm, \pi^\circ$, n, p, $\mathrm{K}^\pm$ and K°). Electromagnetic particles are the most numerous ones and carry the main part of the total energy ($\approx$ 97 %). The remaining energy is shared by the other components (muonic part: $\approx 1.7\,\%$).

Any air shower that is initiated by an atomic nuclei as the primary particle starts from its **hadronic component**. The hadronic component consists of the strong interacting particles in the air shower, fragments of nuclei, single nucleons and mesons, for example. The hadronic component corresponds to about 1 % of all the particles arriving on the ground. The first collision typically produces more than fifty secondaries, which carry most of the energy in the early shower stage. These particles are emitted closely to the original particle direction due to high longitudinal momentum. The lateral spread extends only a few tens of meters around the shower axis at the observation level.

The **muonic component** consists of all the muons that are produced during the shower development. Charged mesons, pions or kaons for example, derive from the hadronic component and have a short life time. If no interaction occurs during their propagation, then they will decay to lighter mesons or directly to muons.

$$
\begin{aligned}
\pi^{\pm} &\rightarrow \mu^{\pm} + \nu_{\mu} \\
\mathrm{K}^{\pm} &\rightarrow \mu^{\pm} + \nu_{\mu} && (\mathrm{BR}\ 64\,\%) \\
&\rightarrow \pi^{0} + \pi^{\pm} && (\mathrm{BR}\ 21\,\%) \\
&\rightarrow 3\pi^{\pm} && (\mathrm{BR}\ \ 5\,\%) \\
&\rightarrow \pi^{0} + \mu^{\pm} + \nu_{\mu} && (\mathrm{BR}\ \ 3\,\%) \\
\mu^{\pm} &\rightarrow e^{\pm} + \nu_{e} + \nu_{\mu}
\end{aligned}
$$

The life time of relativistic muons ($\tau \approx 2.2\,\mu\mathrm{s}$) is much longer than the life time of the hadronic component and most of the muons reach the surface of the Earth (depending on the zenith angle and the primary energy of the cosmic ray). They can lose their energy in several ways: Ionisation, bremsstrahlung, direct $e^{\pm}$ pair production and photonuclear interactions.

The **electromagnetic component** consists of the lightest particles in the shower (electrons and positrons) and the photons. The total number of charged particles is dominated by this component. The neutral or charged mesons, derived from the hadronic component, decay by 99 % to photons or muons.

$$
\begin{aligned}
\pi^{0} &\rightarrow \gamma\gamma \\
\pi^{\pm} &\rightarrow \mu^{\pm} + \nu_{\mu}
\end{aligned}
$$

The charged pions live about 10^8 times longer than the neutral pions, which might lead to a smaller contribution to the electromagnetic component. The two resulting energetic photons from the π^0 decay create electrons (pair production). These electrons generate photons by bremsstrahlung.

$$
\begin{aligned}
\gamma &\rightarrow e^{+}e^{-} && (\text{pair production}) \\
e^{\pm} &\rightarrow e^{\pm} + \gamma && (\text{bremsstrahlung})
\end{aligned}
$$

A cascade of electromagnetic particles is initiated until the energy falls below a critical energy E_c (Heitler model). The critical energy for the electromagnetic component in the air corresponds to $E_c \approx 80\,\mathrm{MeV}$. Then the energy loss due to ionisation becomes dominant and no further particles are produced. At this stage the cascade starts to die out and the exponential decrease takes effect (parametrisation from Gaiser-Hillas).

Besides the creation and loss of particles in the longitudinal direction, the electromagnetic component suffers Coulomb scattering. The Molière theory describes the laterally spread out of particles and contains the Molière radius R_m as a characteristic quantity of extensive air showers [Moli 47, Moli 48].

The lateral distribution of electrons on the observation level is described by the NKG function [Grei 56, Kama 58] (named after Nishimura, Kamata, and Greisen) and follows:

$$
\rho(d_{\mathrm{axis}}) = \frac{N_e}{2\pi \cdot R_m^2} \cdot \left(\frac{d_{\mathrm{axis}}}{R_m}\right)^{s-\alpha} \cdot \left(1 + \frac{d_{\mathrm{axis}}}{R_m}\right)^{s-\beta} \cdot \frac{\Gamma(\beta - s)}{\Gamma(s)\Gamma(\beta - \alpha \cdot s)}
$$

The electron density $\rho(d_{\text{axis}})$ is calculated from the measured number of electrons N_e on the observation level and the distance to the shower axis d_{axis}. The parameter s (or shower age) is fitted to the lateral particle distribution, measured on the ground and describes the lateral shape, whereas the parameters α and β are used as a normalisation factor.

An estimation of the primary energy can be performed on the basis of the total particle number determined by the NKG function, whereas the primary mass can be estimated from the ratio of the measured muon number to the electron number (N_μ/N_e) [Haun 03a].

2.3 Radio Emission

In addition to the energy loss of particles of the electromagnetic component, further secondary effects are expected from these numerous particles in extensive air showers. They excite nitrogen molecules in the air by ionisation and thereby lose part of their energy. The de-excitation of the molecules is partly emitted as fluorescence light and can be observed with telescopes on the ground level, as done at the Pierre Auger Observatory [Blue 03, Abra 04].

Electromagnetic radiation is emitted when charged particles pass through an insulator at a speed greater than the speed of light in that medium, the so-called Cherenkov radiation. The refractive index of the air $n_{\text{air}} \approx 1.000292$ ($\lambda = 589\,\text{nm}$) is only slightly larger than the one of the vacuum $n_{\text{vac}} = 1$. This is a large background source for fluorescence measurements [Nerl 05], but it contributes only little to the emission in the radio frequency range.

It was Askaryan who proposed an effect leading to radio emission in the air and especially in dense media [Aska 62, Aska 65]. The electromagnetic cascade generates $e^{\pm}$ pairs by pair production. The positrons might annihilate with the electrons of the air molecules. Furthermore, the electrons from the air molecules might be regenerated and may contribute to the electromagnetic component. This leads to a negative charge excess that travels faster towards the Earth than the speed of light in the air and additionally emits Cherenkov radiation. The emission will be coherent for wavelengths smaller than the shower disc thickness.

Finally, the radio signal can be observed on the ground due to the fact that the atmosphere is radio transparent. The origin of radiation in the radio frequency range in the air is most likely connected to the magnetic field of the Earth and was suggested as a geomagnetic production by Hazen and collaborators [Haze 69]. The first analytical model that took the charge excess and the geomagnetic emission mechanism into account was developed by Kahn & Lerche [Kahn 66].

2.3.1 Geosynchrotron Model

The magnetic field of the Earth might be approximated as a magnetic dipole. All the particles of an extensive air shower penetrate through this magnetic field $\vec{\mathbf{B}}$ with a velocity $\vec{\mathbf{v}}$. Particles with a charge q are deflected due to the Lorentz force $\vec{\mathbf{F}}$:

$$\vec{\mathbf{F}} = q\left(\vec{\mathbf{v}} \times \vec{\mathbf{B}}\right)$$

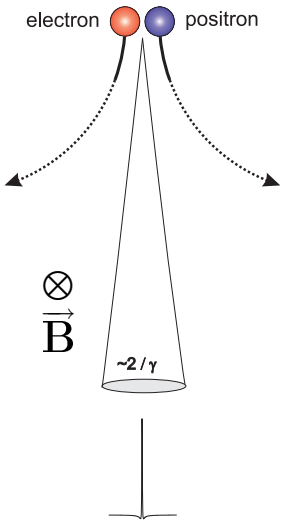

Figure 2.2: Positron and electron propagate through the magnetic field $\vec{\mathbf{B}}$ of the Earth and are deflected due to the Lorentz force. The accelerated and charged particles emit electromagnetic radiation (radio frequency range) in the direction of motion.

The influence of the Lorentz force $\vec{\mathbf{F}}$ on the lightest charged particles is illustrated in fig. 2.2 with a vertical direction of motion and a magnetic field pointing into the picture plane.

Any accelerated charged particle (charge q, mass m, energy E) contributes to electromagnetic radiation due to the synchrotron radiation. The amount of radiation loss follows $-\Delta E_{\text{sync}} \propto \left(\frac{E}{mc^2}\right)^4$ for a complete gyration cycle of the particle in the magnetic field. Thus, only the lightest particles ($e^{\pm}$) contribute to radio emission. The effect for muons is weaker due to their higher mass 8 orders of magnitude ($m_\mu \approx 207 \cdot m_e$). The electromagnetic radiation is emitted in the radio frequency range (for air) and in forward direction with an emission cone proportional to the inverse Lorentz factor ($\propto \gamma^-1$).

This synchrotron radiation in relation to the geomagnetic field of the Earth is called **geosynchrotron radiation**.

The observation of radio emission from extensive air showers has a number of advantages compared to the established measurement techniques, like the observation of fluorescence light or the detection of secondary particles on the ground.

The geosynchrotron radiation is almost independent of the observing conditions, except during thunderstorms. The additional electric fields during thunderstorm conditions might accelerate or decelerate the charged particles and radio emission is amplified or attenuated [Buit 07].

A much higher duty cycle by radio observations is possible due to day and night measurements, whereas optical observations are limited by the light of the Sun or the Moon and clouds. The possible duty cycles at the Pierre Auger Observatory and during the LOPES experiment are larger than 95 %.

The atmosphere of the Earth is almost transparent for radiation in the radio frequency domain and the emission of extensive air showers is not attenuated. Thus, radio emission

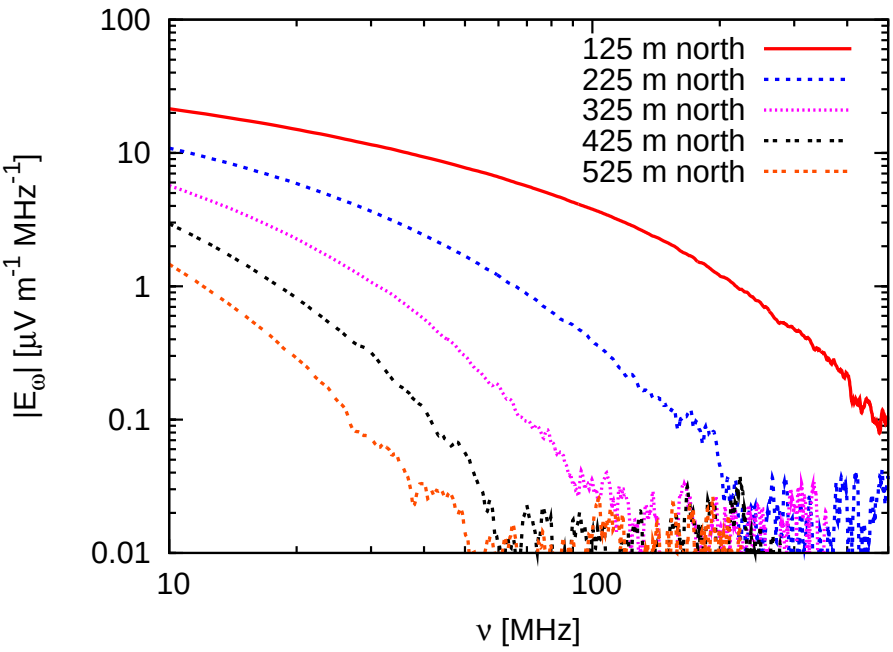

Figure 2.3: Monte Carlo simulated field strength $|E_\omega|$ in the frequency domain for a vertical shower with a primary energy of 10^{17} eV. The shown distances correspond to different observation distances to the shower axis by moving to the north. The steep fall off (double logarithmic scale) levels off numerical noise at large frequencies [Hueg 07].

from highly inclined air showers is observed, whereas the secondary particles have almost died out on the ground level [Petr 07]. Such investigations might help to study highly inclined air showers and air showers that are induced by high energy neutrinos.

2.3.2 Monte Carlo Simulations

Falcke & Gorham developed a complete model to describe the radio emission in the context of the geomagnetic field [Falc 03]. Analytical approaches are available to describe the shower evolution in relation to its atmospheric depth. The combination of these approaches with Monte Carlo simulations allows to parametrise the radio emission of extensive air showers as given in eq. 2.1 [Hueg 05a, Hueg 05b].

$$\begin{aligned} |\mathbf{E}(r,\varphi_0,E_p,X_{\max})| =& f E_0 \left(\frac{E_p}{10^{17}\,\mathrm{eV}}\right)^{0.96} \\ & \cdot \exp\left(-\frac{200\,\mathrm{m}\cdot(\alpha(X_{\max}-1)+l(r,\varphi_0)}{\alpha(X_{\max})\cdot l_\theta}\right) \\ & \cdot \exp\left(-\frac{\frac{f}{\mathrm{MHz}}-10}{47.96\cdot\exp\left(-l(r,\varphi_0)\right)}\right) \end{aligned} \tag{2.1}$$

This parametrisation includes a change of the scale factor l_θ with respect to the shower maximum $X_{\max}$ expressed as the ratio $\alpha(X_{\max}) = l_\theta(X_{\max})/l_\theta(631\,\mathrm{g/cm^2})$. The scale

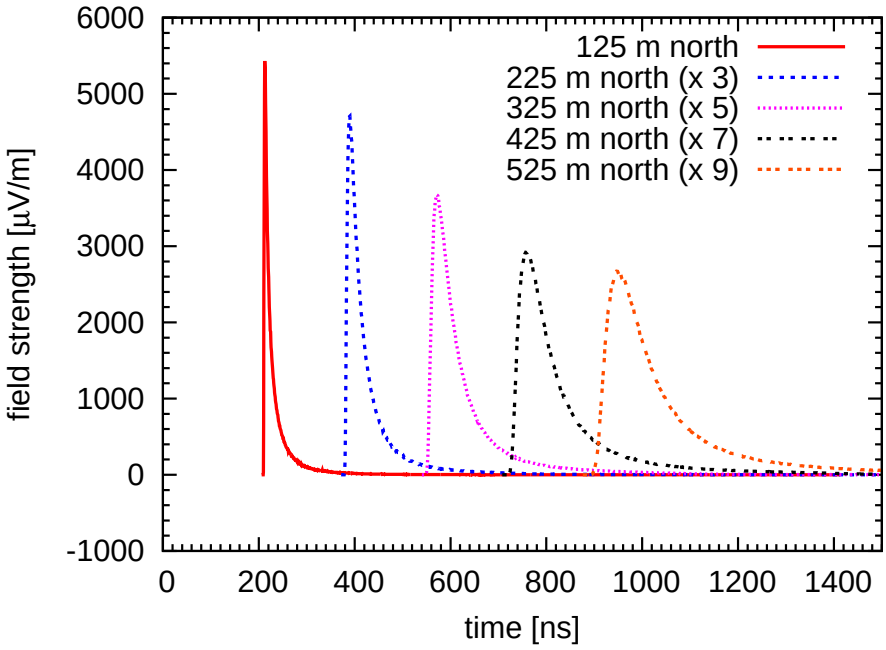

Figure 2.4: The simulated field strength in the time domain of the same simulated shower event as shown in fig. 2.3. The illustrated pulses are scaled for a better comparison and represent different distances to the shower axis by moving to the north [Hueg 07].

parameter $l(r,\varphi) = r\sqrt{1-\cos^2(\varphi_0-\varphi)\sin^2\theta}$ is the transformation from the ground-based to the shower-based coordinate system. Here φ and θ specify the shower azimuth and zenith angle, r corresponds to the observer distance from the shower centre and φ_0 corresponds to the azimuth angle of the observer. The electric field strength of eq. 2.1 can be approximated as linear in relation to the energy E_p of the primary particle and follows a power law relation with an index of $\kappa \approx 0.8 - 1.0$ due to the position of the observer in relation to the shower core.

The exact shower evolution of the electrons and positrons is provided by the air shower simulation package CORSIKA [Heck 98] and plays an important role for sophisticated Monte Carlo simulations. The lateral distribution of the particles, the shower-to-shower fluctuations, the energy content as well as the particle numbers are available for simulation of radio emission [Hueg 07].

At this point of the Monte Carlo simulations we were able to investigate in detail the differences between the simulated data and the measured data and were able to verify the geosynchrotron model. Such a simulated shower event is illustrated in the frequency domain in fig. 2.3 as well as in the time domain in fig. 2.4. These data are based on proton induced air showers with an energy of $E = 10^{17}\,\mathrm{eV}$. The zenith and azimuth angles are $\theta = 30°$ and $\varphi = 180°$ (north direction). The shown distances to the shower axis result from a movement of the observer towards the north.

The introduced Monte Carlo simulation based on CORSIKA might be regarded as an approach in a microscopic way of modelling the radio emission in extensive air showers and is being studied by Kalmykov and collaborators as well [Kalm 06]. A macroscopic

point of view, the magnetic field of the Earth induces a net electric current in the electron-positron plasma of the electromagnetic component by deflecting the lightest charged particles (Lorentz force) in opposite directions, is being investigated as well [Scho 08].

The calculated pulses have a small negative pulse shape in this macroscopic model, which is neglected in the Monte Carlo simulations, but is now being considered [Hueg 08]. Since all the Monte Carlo studies are still under development, a experimentally verification of the different approaches has to be performed with recent and future experiments.

2.3.3 Past and Recent Experiments

The experimental verification started in the 1960s after the predictions of Askaryan [Aska 62, Aska 65]. The first discovery of radio pulses in correlation with cosmic ray air showers at a frequency of $f = 44\,\mathrm{MHz}$ and a bandwidth of $\Delta f = 2.75\,\mathrm{MHz}$ is related to Jelly and collaborators [Jell 65]. In the following years emission from 2 MHz up to 520 MHz was found. The experimental and theoretical results were summarised in a detailed review by Allan [Alla 71].

A parametrisation results from this review, which is determined by the measurements of the radio emission combined with the theoretical expectations at this time as given in eq. 2.2.

$$\epsilon_f = 20 \cdot \left(\frac{E_p}{10^{17}\,\mathrm{eV}}\right) \cdot \sin\alpha \cdot \cos\theta \cdot \exp\left(-\frac{d_{\mathrm{axis}}}{d_0(f,\theta)}\right) \left[\frac{\mu\mathrm{V}}{\mathrm{m}\cdot\mathrm{MHz}}\right] \tag{2.2}$$

Where E_p is the energy of the primary particle, α the angle between the shower axis and the geomagnetic field lines (geomagnetic angle), θ is the zenith angle and d_{axis} corresponds to the distance between the antenna and the shower axis (reference frame of the shower). The scale parameter d_0 was determined at about 110 m at $f = 55\,\mathrm{MHz}$ considering $\theta < 35°$.

The historical experiments were limited by the existing technology. Measurements with a very small bandwidth of a few MHz were performed and no digital electronics for data storing or sufficient trigger concepts were available. Improvements by other detection techniques (e.g. scintillator and fluorescence) had the consequence of stopping further experimental investigations on radio emission of extensive air showers.

In fact, if a coincidence of several particle detectors was detected an analogue trigger took a picture of the screen of an oscilloscope. These photographs were used to analyse the observed radio emission. The received amount of background (mono-frequent and transient signals) could not be suppressed by digital tools and lowered the quality of the data. Measurements were often only done at night when commercial TV and radio stations were turned off [Week 01].

The field of radio emission from cosmic ray air showers revived with the technical and theoretical improvements. Since the work of Falcke & Gorham [Falc 03] many new experiments have been installed to observe the geosynchrotron radiation. These experiments follow new approaches with digital electronics state-of-the-art, for example the CODALEMA experiment [Ardo 05] and the LOPES experiment with its different configurations like LOPES10 [Horn 06], LOPES30 [Nehl 08a] as well as LOPES$^{\mathrm{STAR}}$ [this thesis].

The LOPES experiment measures the radio emission of cosmic ray air showers ($E_p < 10^{18}\,\mathrm{eV}$) in coincidence with the well-established extensive air shower experi-

ment KASCADE and KASCADE-Grande, respectively [Anto 03, Nava 04]. The proof-of-principle with this kind of detection technique was shown [Falc 05]. A parametrisation of the radio pulse height ϵ_{est} of the signal measured in the east-west polarisation ($40 - 80\,\text{MHz}$) as a function of the geometry of the air shower and the energy of the primary particle E_p, simular to eq. 2.2, was investigated and is given in eq. 2.3 [Horn 06].

$$\begin{aligned}\epsilon_{\text{est}} =&(11 \pm 1) \cdot ((1.16 \pm 0.03) - \cos\alpha) \cdot \cos\theta \\ &\cdot \exp\left(-\frac{d_{\text{axis}}}{(236 \pm 81)\,\text{m}}\right) \cdot \left(\frac{E_p}{10^{17}\,\text{eV}}\right)^{(0.95\pm0.04)} \left[\frac{\mu\text{V}}{\text{m} \cdot \text{MHz}}\right]\end{aligned} \tag{2.3}$$

A comparison of eq. 2.2 with eq. 2.3 points out several differences, e.g. the resulting scale parameter $d_0 = (236 \pm 81)\,\text{m}$ differs by a factor of 2, whereas the parametrisation of the geomagnetic angle α follows different approaches. A more detailed discussion about the parametrisation of the measured field strength of the past experiments and the results from the LOPES$^{\text{STAR}}$ experiment is presented in the analysis chapter 6.

So far the comparison of theories and experimental results are not complete nor fully understood. A larger antenna array with good calibration, refined analysis of the data, and sufficient self-trigger system to suppress transient signals and radio interferences (e.g. TV transmitters) is necessary. LOPES$^{\text{STAR}}$, as described in the next chapter, is a main building block on this path.

Chapter 3

LOPES^{STAR}

3.1 Introduction

The LOfar PrototypE Station (LOPES) is installed on the site of the Forschungszentrum Karlsruhe to record radio emission emitted by Cosmic Rays (CRs). The measurements are performed in coincidence with the well-established extensive air shower experiment KASCADE-Grande. In a first step 10 and later additional 20 short dipole antennas with an inverted V-shape (LOPES30) were installed to observe the east-west polarised component of the electric field and are externally triggered by KASCADE-Grande [Horn 06]. Later a rearrangement of the LOPES30 antennas was performed to be able to measure the north-south & east-west polarised component of the electric field with at least 15 antennas. The LOPES30 configuration is set up within the KASCADE-Array, which limits the signal quality due to the emitted electromagnetic noise of the particle detectors.

The LOPES Self Triggered Array of Radio detectors (LOPES^{STAR}) is the enhancement of LOPES30 to optimise detection techniques for radio emission of high energy cosmic rays, in particular to provide a self-trigger system [Gemm 06]. In addition, it is a prototype detector for large-scale arrays, like the Pierre Auger Observatory.

Based on theory and simulations cosmic ray particle produces a broadband signal in the range of a few MHz up to over 100 MHz. The LOPES^{STAR} experiment records a frequency band from 40−80 MHz with an array of 10 antennas for the north-south & east-west polarised components. The measured signals are convoluted with the characteristics of the electronics used. A reconstruction of the spectrum is only possible within the observed frequency range.

This chapter describes the detector layout and configuration as well as all the components of the signal chain. Furthermore, an overview of the KASCADE-Grande experiment is given, the external trigger used is described, and the developed and optimised digital methods for the data analysis of LOPES^{STAR} are presented.

3.2 Detector Layout

3.2.1 Forschungszentrum Karlsruhe

LOPES^{STAR} is installed inside the area of the KASCADE-Grande experiment (see fig. 3.1) so that the radio background generated by the particle detectors (KASCADE-Array) is not measured. Each marked position (red triangle) corresponds to one antenna measuring east-west and north-south polarisation. The 10 antennas are arranged in three clusters. Two clusters (D17 and D30) consist of four antennas and one cluster (D19) consists of two antennas. The name convention of the clusters is simply given by the

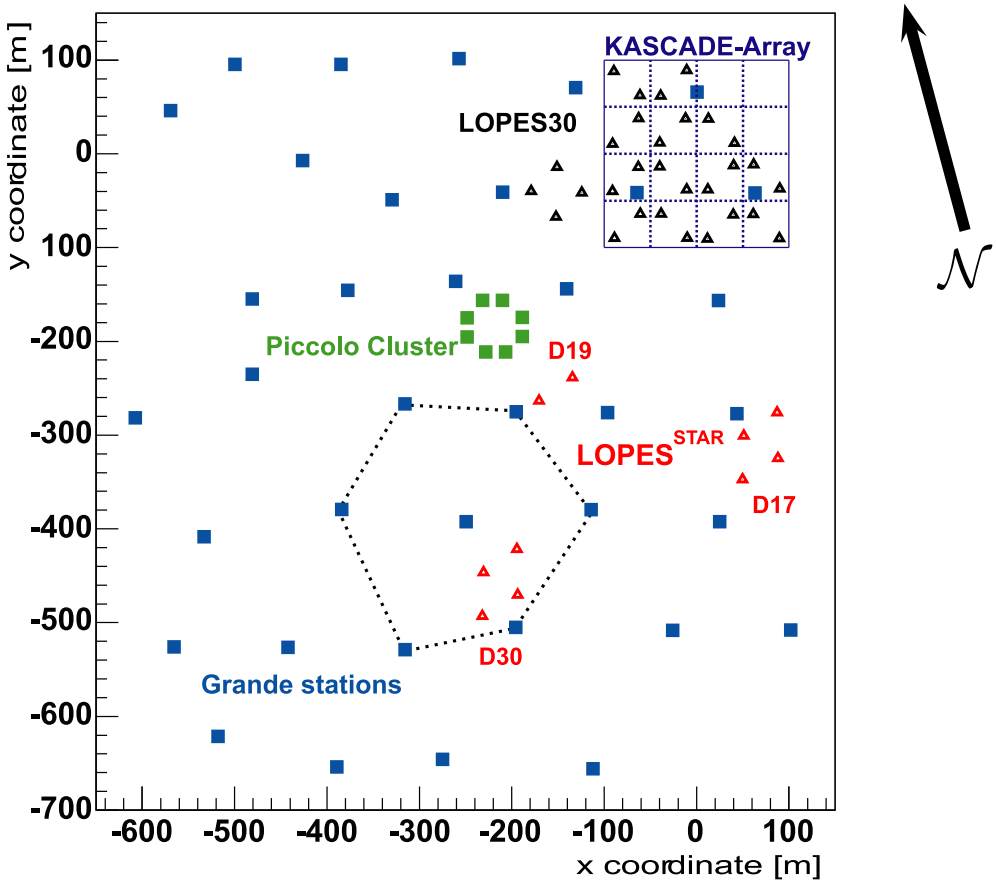

Figure 3.1: Layout of the cosmic ray experiments KASCADE-Grande (Array, Grande, and Piccolo), the radio detector LOPES30 as well as LOPES^{STAR} (red triangle), and the external radio trigger constraint (7-out-of-7-coincidence) from KASCADE-Grande (dashed black line).

identification number of the nearby KASCADE-Grande station, which is also the housing of the Data AcQuisition (DAQ) system.

The antenna positions in cluster D17 and D30 are part of a vertex of an equilateral triangle (see fig. 3.1 & 3.2 and table 3.1). The chosen geometry is part of the self-trigger concept with a baseline b of $b_{D17} = 70\,\mathrm{m}$ and $b_{D30} = 65\,\mathrm{m}$. By evaluating the timing of signals in each antenna a coincidence constraint can be performed as well as a fast estimation of the arrival direction.

The name convention for the LOPES^{STAR} antennas in each cluster (see table 3.1) is defined by their azimuth φ orientation in degrees (clockwise, north: $\varphi = 0°$), except the centred antenna (CTR) next to the DAQ system.

These 10 antennas measure absolutely calibrated the north-south & east-west polarised component of the radio emission of cosmic ray air showers if an external trigger signal is given by the KASCADE-Grande experiment. The provided trigger corresponds to an energy threshold of about $10^{16}\,\mathrm{eV}$ of the primary particle. It is expected to detect clear

	x / m	Δx/m	y / m	Δy/m	z / m	Δz/m
D17 – CTR	43.764	0.004	-284.214	0.006	126.803	0.006
D17 – 060	106.322	0.019	-248.751	0.014	126.235	0.024
D17 – 120	107.956	0.036	-319.652	0.019	127.982	0.027
D17 – 180	43.488	0.075	-356.203	0.065	126.878	0.076
D30 – CTR	-191.754	0.014	-469.506	0.017	126.826	0.018
D30 – 240	-233.720	0.024	-495.219	0.019	128.327	0.020
D30 – 300	-233.634	0.021	-444.444	0.019	127.604	0.022
D30 – 360	-191.601	0.017	-419.977	0.019	127.218	0.018
D19 – CTR	-192.121	0.014	-271.226	0.023	127.298	0.024
D19 – 030	-164.956	0.023	-219.832	0.024	128.010	0.035

Table 3.1: The geometrical position and their uncertainty of the LOPES$^{\mathrm{STAR}}$ antennas in relation to the reference frame of KASCADE-Grande and the z coordinate in relation to sea level.

radio pulses in the time domain at an energy of the primary particle of $E > 10^{17.5}\,\mathrm{eV}$ for the LOPES$^{\mathrm{STAR}}$ configuration (LPDA and electronics) [Krom 08]. Thus, most of the recorded data will show no signal of the radio emission but they are used to develop methods to reduce background signals.

Antenna Positions

The positions of the LOPES$^{\mathrm{STAR}}$ antennas were determined with a Differential Global Position System (DPGS) and transformed to the reference frame of KASCADE-Grande. One of the two hand-held units (type: ProMark2, Magellan) was mounted at the 21^{th} LOPES30 antenna [Hake 06]. The positions of the antennas were measured in relation to this well-known reference point with the second hand-held unit. The commercial analysis software (Ashtech Solutions, version 2.6, Magellan) determined the positions of the antennas and their uncertainties. The listed values in table 3.1 are already transformed to the reference frame of KASCADE-Grande. The positioning uncertainties are neglected in the following error propagations with respect to the obvious higher uncertainties of reconstructed quantities (e.g. position of the shower core: $\Delta x \approx \Delta y \approx 7\,\mathrm{m}$ [Coss 08]).

The orientation of the measured polarisation components are aligned with the corresponding point of the compass in the north-south and in the east-west direction.

3.2.2 External Trigger Source

A convenient way to start developing a self-trigger system, is the usage of a well-defined external trigger based on particle detectors. KASCADE-Grande provides such an external trigger source in the framework of the LOPES$^{\mathrm{STAR}}$ experiment with an energy threshold of about $10^{16}\,\mathrm{eV}$. If seven KASCADE-Grande stations (cluster 13 – see below) have a trigger in each station within a defined coincidence time window, a trigger signal is sent to all 10 LPDAs. The dashed black line in figure 3.1 marks six of the specified seven KASCADE-Grande stations. An additional one is placed in the middle of this

Figure 3.2: Part of the antenna cluster D30. The triangular structure of the antenna positions and the north-south & east-west polarisation are clearly visible.

hexagon. A well-defined data set results from these measurements in combination with the results of the reconstruction from KASCADE-Grande.

KASCADE-Grande

An introduction to the KArlsruher Shower Core and Array DEtector (KASCADE) is given in the references [Anto 03, Nava 04].

KASCADE-Grande is an extensive air shower experiment to study cosmic rays in the primary energy range of $10^{16}-10^{18}$ eV. It is located at the Forschungszentrum Karlsruhe, 110 m above sea level ($49°N, 8°S$), and consists of the KASCADE experiment (with the Field Array and the Muon Tracking Detector), the Grande array and the Piccolo array (see fig. 3.1).

KASCADE-Array The KASCADE-Array covers $200 \times 200\,\mathrm{m}^2$ and is composed of 252 stations with a grid spacing of 13 m. In each station, four e/γ detectors (respectively two in the outer stations) are positioned on a lead/iron plate (10 cm Pb and 4 cm Fe), corresponding to 20 radiation lengths and resulting in an energy threshold for vertical muons of 230 MeV in the μ detector below the plates. The stations are organised in 16 clusters of 16 stations each (except the four inner ones consisting of 15), whereas the inner clusters have no μ detectors. A detailed description of all the detector components, their energy dependent thresholds and uncertainties is given in [Anto 03].

Grande-Array The Grande-Array detectors have been obtained by re-assembling the electromagnetic detectors of the former EAS-TOP experiment [Agli 93]. The Grande array consists of 37 stations each of $10\,\mathrm{m}^2$ of plastic scintillators over a surface of $700 \times 700\,\mathrm{m}^2$. The detectors form a triangular grid with an average spacing of 137 m. A part of the Grande array overlaps with the KASCADE-Array. Five 700 m cables connect each of the stations with the central DAQ of KASCADE-Grande [Pier 07].

Grande Trigger The 37 Grande stations are organised in 18 trigger clusters of 7 stations each, with 6 forming a hexagon and 1 central station. Several trigger constraints for each trigger cluster are defined: 4-out-of-7-coincidence (4/7) and 7-out-of-7-coincidence (7/7). A mean trigger rate of $f \approx 5\,\mathrm{Hz}$ (4/7) and $f \approx 0.05\,\mathrm{Hz}$ (7/7) is obtained. The Grande trigger decisions are made in the central DAQ, where all the signal cables arrive.

The efficiencies of different trigger conditions have been studied by averaging over various simulations of the experiment [Haun 03b]. For this purpose, air showers induced by different primaries (proton and iron) and at different energies as well as the experiment response have been simulated (the detector and the different trigger conditions). The 7/7 trigger condition reaches full efficiency at about $10^{16}\,\mathrm{eV}$.

The operating experience of the KASCADE-Grande collaboration has shown that the event reconstruction is reliable, if the 7/7 cluster 13 trigger is active. Due to this experience and the close location to all the LOPES$^{\mathrm{STAR}}$ antennas the cluster 13 trigger was chosen as an external trigger source.

The antenna field D19 and D30 receive the trigger signal via a 70 m cable (type RG58). The trigger signal for D17 is transmitted via an optical fibre ($\lambda = 820\,\mathrm{nm}$) with respect to the distance ($\approx 200\,\mathrm{m}$) to the Grande DAQ.

Reference Frame The reference frame for the ground coordinates is located in the centre of the KASCADE array inside the Forschungszentrum Karlsruhe (110 meter above sea level, latitude: 49° north, longitude: 8° east). The azimuth angle φ is counted clockwise (north: $\varphi = 0°$) and the y-axis is rotated 15° clockwise with respect to the north [Pier 07]. The zenith angle θ is zero for vertical incoming particles and $\theta = 90°$ corresponds to a horizontal arrival direction.

The listed geometrical positions of all the LOPES$^{\mathrm{STAR}}$ antennas in table 3.1 are given in this reference frame.

Shower Reconstruction from KASCADE-Grande The KASCADE collaboration provides its reconstruction results for the LOPES collaboration to investigate correlations between the measured radio signals and the detected shower quantities based on particle measurements. The reconstruction from KASCADE-Grande is calculated with KRETA (Kascade Reconstruction for ExTensive Air showers).

The results from the third reconstruction level from KRETA (version V11702) are used for the present studies.

3.2.3 Pierre Auger Observatory

The future development of the radio detection technique aims at setting up an independent radio detector in the framework of the Pierre Auger Observatory [Blue 03, Abra 04]. The key feature of the observatory is its hybrid detection technique. On the one hand

the fluorescence light of excited nitrogen is detected with 24 optical telescopes (FD) positioned on the boundary of a 3000 km^2 array. On the other hand secondary particles are measured on the ground with water Cherenkov tanks (SD) spaced by a distance of 1.5 km. The whole experiment is located in the southern hemisphere in Argentina near the town of Malargüe (province of Mendoza). The Pierre Auger Observatory reaches full efficiency at primary particles energy of $E \approx 10^{18}$ eV and is able to observe particles up to the highest energies above 10^{20} eV.

Improving the radio detection technique requires boundary conditions in particular accessibility and availability of established cosmic ray experiments. The KASCADE-Grande experiment is convenient to access, but the energy range is limited to $E \leq 10^{18}$ eV due to the instrumented area. In contrast, the Pierre Auger Observatory is far away, expensive to access, but provides a higher energy threshold of 10^{18} eV.

The consequence is the following strategy: The prototype detector LOPES^{STAR} is developed, set up, and verified in coincidence with KASCADE-Grande, which is convenient to access on the site of the Forschungszentrum Karlsruhe. The obtained results are combined with results from other investigations of the radio technique to instrument an area of about 20 km^2 within the Pierre Auger Observatory.

In a first step a detector system simular to the one at the Forschungszentrum Karlsruhe was installed within the SD array (antenna cluster D42) of the Pierre Auger Observatory. Each of the three antennas measure the north-south & east-west polarised component of the electric field strength. In a first data taking period, the background was measured to compare interferences of the different environments and the robustness of the equipment was tested (see chapter 5).

3.3 Signal Chain

The signal chain consists of all the electronic components used by the receiving part of the system up to the storage of the raw data. This section describes the complete LOPES^{STAR} configuration. A more detailed discussion about the spectral characteristics of the components will be given when the calibration is described (see chapter 4).

3.3.1 Logarithmic-Periodic Dipole Antenna

The Logarithmic-Periodic Dipole Antenna (LPDA) was chosen to measure one polarisation (north-south or east-west) of the electric field. This antenna type fits the requirements of radio detection of high energy cosmic rays [Krom 08].

The main characteristic of the LPDA is described by its direction sensitivity. For low zenith angles $\theta < 60°$ the antenna gain is about 3.5 dBi, whereas for $\theta > 60°$ the signal is strongly suppressed. The interferences from surrounding buildings and machines complicate the detection of radio emission from zenith angles $\theta > 60°$. The major part of the man-made background signals reaches the detector horizontally and is suppressed by the LPDA in an early stage of data processing. The arriving direction of radio emission of CR particles are randomly distributed over the sky. Radio emission of highly inclined air showers is easy to detect due to the low attenuation of the atmosphere of the Earth in the radio frequency range but is suppressed by the direction sensitivity of this type of antenna.

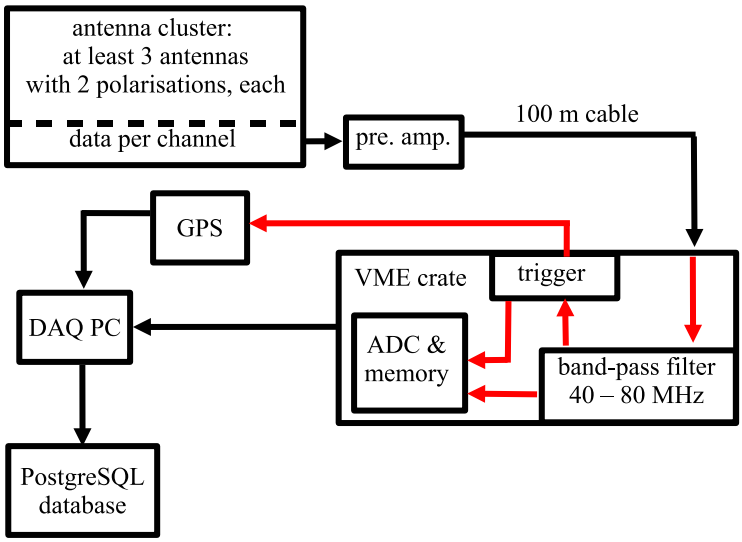

Figure 3.3: Block diagram of the signal chain for each antenna cluster. An external trigger signal from KASCADE-Grande is used.

The LPDA has a real impedance at the signal output, which is an important detail for an absolute calibration. An additional benefit of the chosen geometry of the LPDA is its first order band-pass filter ($f \approx 30 - 90\,\mathrm{MHz}$), due to the length of the dipole arms (antenna geometry).

Two LPDAs are combined by rotating one LPDA by 90° and fixing both in the centre. The resulting antenna measures the north-south and east-west polarisation simultaneously and is named in the following LOPES$^{\mathrm{STAR}}$ antenna or short LPDA. Three out of four LPDAs of cluster D30 are seen in photography 3.2.

3.3.2 Analogue Electronics

The signal of each channel is raised by a factor of $a_{\mathrm{LNA}} \approx 22\,\mathrm{dB}$ by a Low Noise pre-Amplifier (LNA). After transmission via a 100 m cable (type RG213) the signal is attenuated by the cable by $a_{\mathrm{RG213}} \approx -5\,\mathrm{dB}$. The following $40 - 80\,\mathrm{MHz}$ band-pass filter (32^{nd} order) re-amplifies the signal by $a_{\text{band-pass}} \approx 37\,\mathrm{dB}$. The LNA and band-pass filter are developed for the requirements of LOPES$^{\mathrm{STAR}}$ [Krom 08].

The Radio Frequent (RF) signal is digitised by a 12 bit Analogue Digital Converter (ADC) with a sampling frequency of 80 MHz (type SIS3300, Struck GmbH). The digitised data is then transferred via an optical fibre to a VME-PCI bus interface (type SIS1100/3100, Struck GmbH) to a standard Personal Computer (PC). The enclosure for the band-pass filter, the ADC with the sampling clock, and the communication board is provided by a standard VME-Crate[1]. The block diagram in figure 3.3 illustrates the signal chain.

[1] Versa Module Europa

3.3.3 Digital Electronics

The LOPES^{STAR} electronics fulfils the constraints of sub-sampling in the second Nyquist zone [Nyqu 02]. The upper band-pass limit of 80 MHz is twice the lower band-pass limit of 40 MHz. Thus, the digitisation of a 40 MHz bandwidth signal with 80 MHz contains the full information of the band limited signal.

The resulting sub-sampled data are stored in a 128 kB ring buffer. The raw data are stored within a PostGreSql data base together with a timestamp from the Global Position System (GPS) clock (type GPS167LCD-MP, Mainberg), if a trigger[2] occurs. The timestamp is specified by the manufacturer with an accuracy of $\Delta t = 100\,\mathrm{ns}$ and is recorded for a combined reconstruction of the data of all the clusters and for event correlation with KASCADE-Grande. Raw data are stored on a central RAID[3]-5 storage via the Local Area Network (LAN). Due to the usage of a central data base server, a common software interface to read and write data in parallel and consistently has been created (see fig. 3.3).

3.4 Digital Data Analysis

The raw data are recorded in a defined time window of $\Delta t = 25.6\,\mu\mathrm{s}$. The contained time information of the radio emission is limited by the observed bandwidth.

The challenge of a digital data analysis is to deconvolve, calibrate and reconstruct the measured signals. The functionality of the analysis methods, as described in the following, are summarised in the software package star-tools and developed in the framework of this thesis.

Methods and algorithms developed are meanwhile standard tools for the data analysis in the LOPES collaboration and can be summarised as follows:

Fast Fourier Transform The fast Fourier transform determines the spectrum of the amplitude and phase distribution and reverse.

Up-Sampling The up-sampling algorithm increases the sampling frequency artificially by a given factor. This method does not correspond to an interpolation of the time samples, but uses the known frequency limits of sampling.

Envelope Calculation The calculation of the envelope signal of radio frequent data is an important method in the context of the self-trigger system to compare the signal with a threshold or to define pulse parameters.

Suppression of Radio Frequency Interferences Radio frequency interferences are present all the time and measured by the system. Mono-frequent background signals can be sufficiently suppressed by this algorithm.

Observed Time Window The amount of observed time samples corresponds to a time period (sampling frequency of 80 MHz) and to a frequency resolution of the am-

[2] In this case the external trigger from KASCADE-Grande is used. Additionally, any other trigger source might be used (e.g. signal generator).

[3] Redundant Array of Independent Disks; Version 5: All the stored data is redundant to failure of one hard disc, after hot-swap normal operation is resumed.

plitude and phase spectrum. The optimal length is an important factor for the suppression of radio frequency interferences.

3.4.1 Fast Fourier Transform

Each antenna observes a 40−80 MHz band limited signal, which is digitised by a sampling rate of 80 MHz in the time domain. To analyse the characteristics of the radio emission in the frequency domain a Fourier transformation has to be performed. Therefore, the open source and optimised algorithm FFTW[4] (version 3) was chosen to calculate the Fast Fourier Transform (FFT) [Frig 05].

The implementation of the FFT and the inverse FFT methods fulfil Plancherel's theorem. The theorem predicts that the energy of the signal in the Fourier domain is identical to the energy in the time domain, if formula 3.1 is conserved. This is an important detail for algorithms which manipulate the signal in the frequency domain, like background rejection or calibration.

$$\int_{-\infty}^{\infty} |f(t)|^2 \, dt = \int_{-\infty}^{\infty} |F(\omega)|^2 \, d\omega \tag{3.1}$$

The common challenge by applying an FFT is to reduce the influence of the points of discontinuity, due to the FFT requirement of infinitely long time samples. The time data are put together periodically. The points of discontinuity appear by crossing the last sample and the first one. The so-called leakage effect results in non-zero values of $\cos(\omega t)$ after its Fourier transform at frequencies other than ω. The solution is to multiply a well-defined window function $w(t)$ by the time data $s(t)$ to achieve a periodic function. The amplitude distribution $H(f)$ is a convolution of the transformed time data $S(f)$ with the transformed window function $W(f)$.

$$h(t) = s(t) \cdot w(t) \overset{\text{FFT}}{\Longrightarrow} H(f) = S(f) \otimes W(f) \tag{3.2}$$

Various window functions, like Hamming-, Hann- or Cosine-Window, are investigated and their effects are summarised and described by Nuttall [Nutt 81]. The most simple window function is a rectangular function with $w(t) = 1$. Its Fourier transform is $W(f) = \frac{\sin(x)}{x} = \text{sinc}(x)$ and influences the data strongly. The other window functions mentioned are established by working with narrow bandwidth signals and manipulate all the time samples. It is not convenient to manipulate all the samples of broadband signals ($\Delta f_{\text{STAR}} = 40$ MHz), because the influence on the periodic character of the signal is mainly dominated by the samples at the boundaries of the time data. All the time data used in the present studies are Fourier transformed by using a Gaussian window function with a standard deviation of $\sigma = 2.5$ (mean value = 0). Half of the Gaussian function is multiplied by the data at the beginning and at the end, whereas the central part stays the same.

3.4.2 Up-Sampling

All the information of a band limited signal is contained with a sampling frequency higher than twice the highest frequency of interest, the so-called sub-sampling in the second

[4] Fastest Fourier Transform in the West

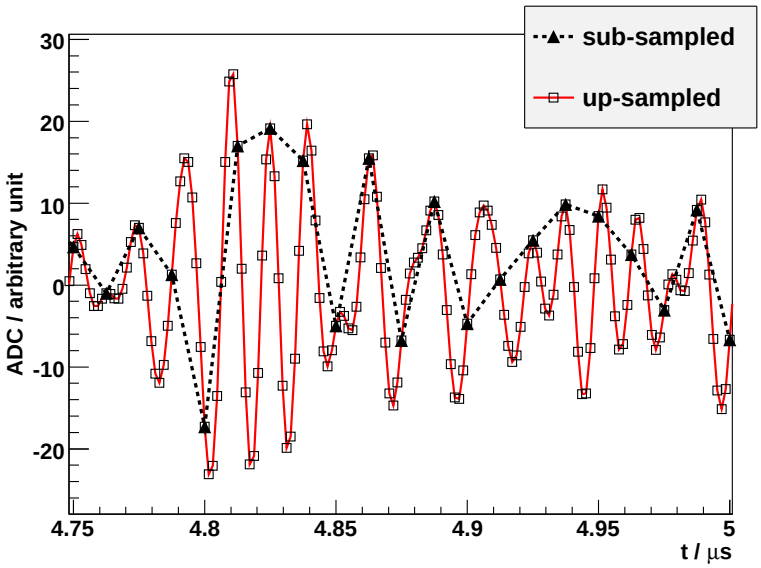

Figure 3.4: Raw sub-sampled data points disposed by up-sampled data (by factor $z = 8$) in the frequency domain. All the data points shown are linked by a straight line.

Nyquist Zone [Nyqu 02]. But one has to preserve boundary conditions: The upper band limit has to be twice the lower band limit. Therefore, a sampling rate of twice the upper band limit is sufficient to keep all the information of the signal. The band-pass filter of LOPES^{STAR} from $40 - 80$ MHz and the ADC sampling rate of 80 MHz used fulfil these sub-sampling requirements.

The advantage of sub-sampling is given by the reduction of the necessary amount of storage for the raw data, as well as the possibility to use electronics with low power consumption, due to the lower sampling frequency. Often, the digital data in the time domain is approximated by linear interpolation or a histogram. But especially in the case of sub-sampled data an up-sampling is necessary by a factor $z = 2$ to 4. Up-sampling by $z = 2$ corresponds to doubling the sampling rate and fulfils the well-established sampling theorem of Shannon [Shan 98]. The classical way of sampling data is performed by using a sampling frequency twice the size of the highest frequency of interest (160 MHz in the case of LOPES^{STAR}).

The up-sampling can be performed in the time or frequency domain. Both methods lead to an increase of the bandwidth and are described in the following.

time domain Up-sampling by z corresponds to set $z - 1$ zero values between each data point. The new data are convoluted with a low pass filter. The critical frequency $f_{\text{low pass}}$ of the filter is a function of z and results in $f_{\text{low pass}} = f_{\text{up}} \cdot z$, with the upper band-pass frequency f_{up}.

frequency domain Each amplitude and phase spectra contain $\frac{n}{2}$ entries for symmetric reasons of the FFT. Up-sampling by $z > 0$ is realised by setting $\frac{n}{2}$ zero values in one block next to lower band-pass limit f_{low}. Additional $(z - 2) \cdot \frac{n}{2}$ zeros in one

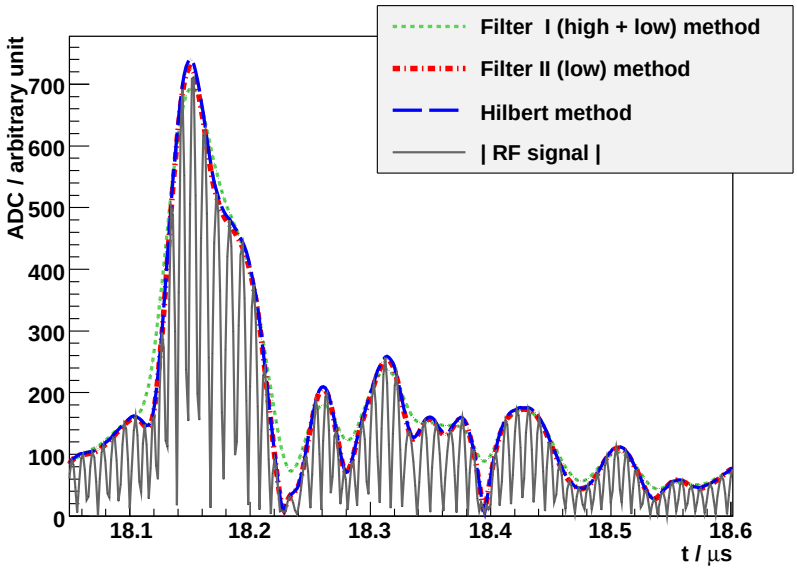

Figure 3.5: Different methods to calculate an envelope signal: Filter I, Filter II, and Hilbert method. The absolute values of the up-sampled Radio Frequent (RF) data are given by the solid black line.

block are put next to f_{up}. The inverse FFT results directly in the up-sampled data. The frequency domain method is used in the following.

The accuracy of the up-sampling is only limited by the band-pass used in the analogue signal chain. If this filter does not fulfil the sub-sampling constraints, additional frequency components are convoluted into the frequency band of interest, manipulate the original data and limit the total accuracy of this method.

An example of up-sampling in the frequency domain is illustrated in figure 3.4. Each sub-sampled data point overlays with one point of the up-sampled data. One can notice as well that the original trace has an inflexion point between each sub-sampled data point. The dot-dashed black line is given by the sub-sampled data points connected by a straight line – what the human brain does obviously. On the other hand the solid red curve corresponds to up-sampled data points connected by a straight line, as well. Only the up-sampled data describe the real behaviour of the data in the time domain.

3.4.3 Envelope Calculation

The recorded RF signal corresponds to the filter response function of the band-pass filter used. The geosynchrotron model predicts pulses with a length of about $10-100\,\mathrm{ns}$. Interferences of the same time length or even longer are present, depending on the specific background sources which influence the antenna cluster. Due to the fact that these background signals are broadband, a rejection can only be performed in the time domain by characterising the RF data. The envelope signal is used for that parametrisation.

Different methods can be used to evaluate the envelope signal in software based on up-sampled data. Three typical methods are discussed here and illustrated in fig. 3.5.

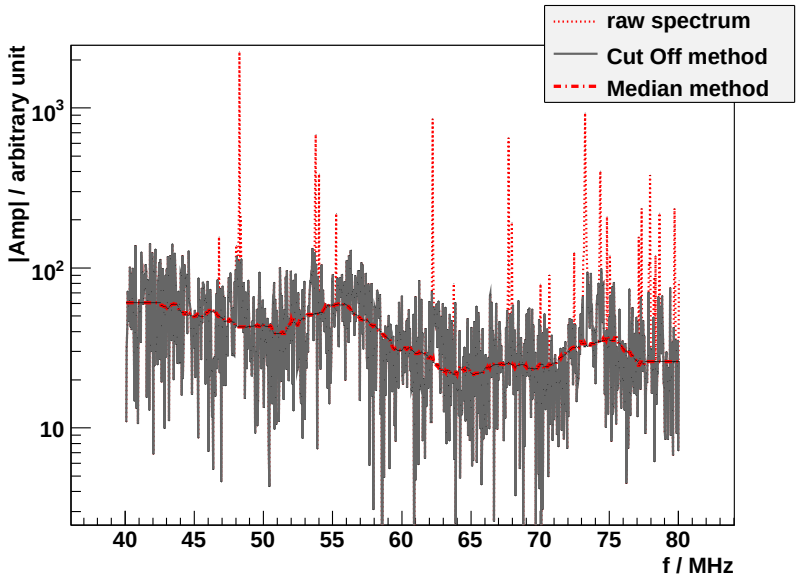

Figure 3.6: Amplitude distribution of the raw spectrum (dashed red line), the Cut Off method (solid black line), and the Median method (dot-dashed red line) to suppress Radio Frequency Interferences (RFI).

From the engineering point of view the RF data have to be squared and filtered by a low pass filter (e.g. LOPES$^{\mathrm{STAR}}$ $f_{\mathrm{low}} = 40\,\mathrm{MHz}$) – Filter II method.

Squaring in the time domain corresponds to a convolution of the signal with itself in the frequency domain. The demodulation of modulated carrier signals in the observed bandwidth can partly be suppressed by applying a high pass filter of $f_{\mathrm{high}} \approx 500\,\mathrm{kHz}$ in addition. The appearing cross demodulations of the convolution are not completely suppressed – Filter I method.

Another method of calculating an envelope is given by using the Hilbert transformation [Brac 00] – Hilbert method. The Hilbert transform H occurs in practice as the imaginary part $s_{\Im}(t) = H\{s_{\Re}(t)\}$ of measured data $s_{\Re}(t)$. After FFT the phases are manipulated. The negative frequency components are shifted by $+90°$ and the positive frequency components are shifted by $-90°$. Afterwards the phase distribution is multiplied by i. This has the effect of restoring the positive frequency components while shifting the negative frequency ones by additional $+90°$, which results in their negation. The envelope calculation $s_{\mathrm{env}}(t)$ follows equation 3.3.

$$s_{\mathrm{env}}(t) = \sqrt{(s_{\Re}(t))^2 \cdot (H\{s_{\Re}(t)\})^2} = \sqrt{(s_{\Re}(t))^2 \cdot (s_{\Im}(t))^2} \tag{3.3}$$

A comparison of the described methods is shown in fig. 3.5. It illustrates the Filter II and the Hilbert methods describe the RF signal well, whereas the Filter I method, with the additional high pass filter, modifies the signal, as expected. In the present studies the more precise and analytical defined Hilbert method is used to calculate an envelope.

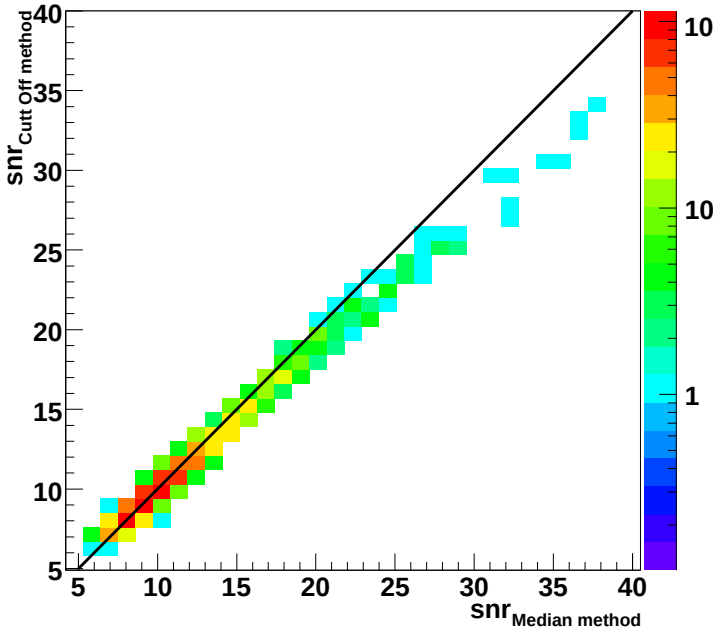

Figure 3.7: Comparison of the Median method ($\mathrm{snr}_{\mathrm{Median\ method}}$) with the Cut Off method ($\mathrm{snr}_{\mathrm{Cut\ Off\ method}}$). The signal-to-noise ratios (snr) are calculated on the basis of the samples (snr $\propto$ voltage).

3.4.4 Suppression of Radio Frequency Interference

Two main classes of background signals have to be distinguished. First, there are broadband interferences, which result in sharp peaks in the time domain. Rejection and suppression of such transient signals need a characterisation of the timing signal combined with a statistical analysis. And second, there are mono frequent sources (e.g. radio or TV transmitters), which show narrow peaks in the frequency domain. These Radio Frequency Interferences (RFI) correspond to a noise floor in the time domain. One obviously has to manipulate the amplitude distribution and leave the phase untouched to suppress RFI.

Two methods of suppression are discussed here and are shown in fig. 3.6 and 3.7. A straightforward approach is to define a dynamic threshold in the amplitude distribution and cut off all the amplitudes above this threshold. The Cut Off method is based on a LOPES30 algorithm [Sing 07]. A moving median filter M is applied to the amplitude distribution $A_{\mathrm{med}}(f) = M\{A_{\mathrm{orig}}(f)\}$. The length m of the sliding window of M is a function of time samples (n) used and follows $m = 64 \cdot \frac{n}{1024}$. The normalised spectrum is independent of hardware characteristics and is calculated by $A_{\mathrm{norm}}(f) = A_{\mathrm{orig}}(f)/A_{\mathrm{med}}(f)$. A threshold is defined by using A_{norm} without the narrow peaks and applied to the whole distribution. The corrected spectrum A_{cor} is used to divide A_{orig}, which results in a RFI suppressed spectrum A_{sup}. The solid grey line in fig. 3.6 illustrates the part

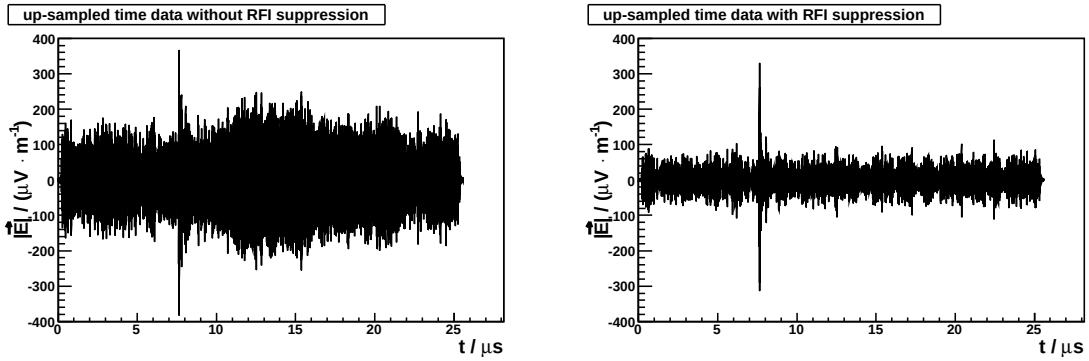

Figure 3.8: Influence of the RFI suppression (median method) on the time data. The noise in the time domain decreases significantly by this method. The searched signal is visible at $\approx 7.5\,\mu$s in both figures.

of the spectrum after the Cut Off method (dotted red line). An inverse FFT of A_{sup} corresponds to the RFI suppressed time data.

Man-made narrow band transmitters carry modulated information in the sideband of the carrier frequency. Two TV transmitters and several radio transmitters are located within the observed frequency band, e.g. the strong TV transmitter Raichberg, as mentioned in section 3.4.5, with its picture carrier at $f = 62.25\,$MHz and its audio carrier $f = 67.75\,$MHz. In Germany, as well as in large parts of the world, the Phase Alternating Line (PAL) broadcast television system is used for colour encoding. As defined in the PAL system, the picture information is amplitude modulated in a $\Delta f = 5\,$MHz sideband of the picture carrier. The audio information (mono signal) is located exactly 5.5 MHz above the picture carrier signal and is frequency modulated. The second audio channel (stereo signal) is again 242.19 kHz above the mono signal and is also frequency modulated.

Keeping the PAL system in mind, the RFI suppression by the Cut Off method suppresses only the carrier signal strength, but leaves the sideband untouched. All the modulated information is still present in the time domain as noise. With respect to the modulated sideband information, the whole spectrum can be replaced by the median filtered one – Median method (see dot-dashed red line in fig. 3.6, sliding window $m = 128 \cdot \Delta f = 5\,$MHz). The median follows the system characteristics present in the amplitude distribution. The carrier frequencies and the remaining sideband modulated information are suppressed. Due to random background processes, like galactic noise, fluctuations in the spectrum are smoothed out by the median method.

In fig. 3.7 the comparison of the Cut Off and Median method are shown. The signal-to-noise ratio (snr) was calculated for both methods on the same data set and based on the samples (snr $\propto$ voltage). The methods are equal up to snr less than 20 and the Median method suppresses RFI signals more significantly for higher snr values. In the following the RFI suppression with the Median method is used.

Figure 3.8 impressively illustrates the significant reduction of the noise in the time domain by applying the RFI suppression (median method) on calibrated and up-sampled data.

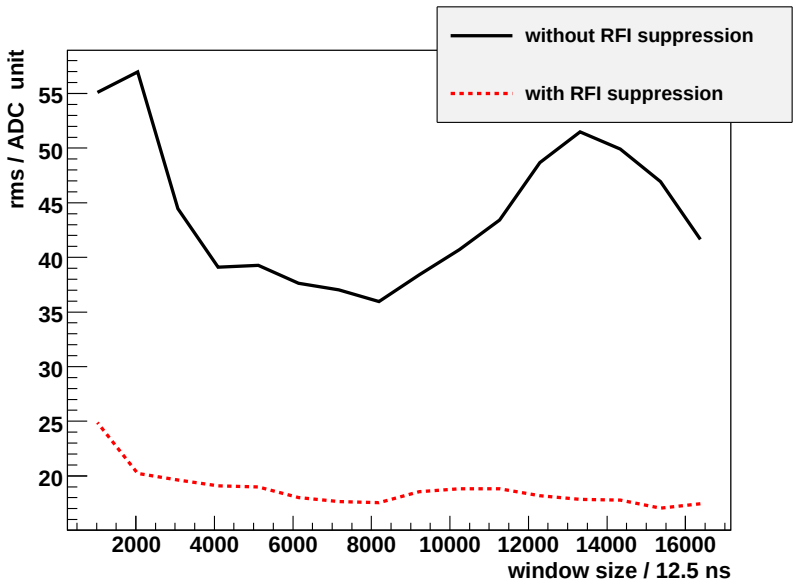

Figure 3.9: The solid line represents the root mean square (rms) for different window sizes of the raw time data, whereas a suppression of the radio interferences was applied to the data and is marked by the dashed line (antenna cluster D30). No significant decrease of the rms for window sizes larger than 2048 samples (optimal length).

3.4.5 Observed Time Window

The n measured time samples used correspond to a time length of $\Delta t = n \cdot 12.5\,\text{ns}$ (sampling rate $f = 80\,\text{MHz}$). This results directly in a frequency resolution of $\delta f = \frac{\Delta f \cdot f}{2 \cdot \Delta t} = \frac{40\,\text{MHz}}{2 \cdot n}$ for the amplitude and phase distribution.

The expected radio emission signal is short-time ($\approx 10 - 100\,\text{ns}$), which means broad in the frequency domain. Therefore, a low resolution is sufficient. On the one hand some interferences are not characterised by a broadband signal. Narrow band background signals could be suppressed much better with a good frequency resolution. On the other hand a longer measuring time also means adding up more interferences to the real shower signal during recording.

A good balance between sufficient frequency resolution and a high signal-to-noise ratio (snr) has to be found. The analysis of data with $n_{\text{max}} = 16 \cdot 1024 = 16\text{k}$ samples by varying the time length yields to an optimal resolution with a time window of $\Delta t = 2048 \cdot 12.5\,\text{ns} = 25.6\,\mu\text{s}$. Figure 3.9 illustrates the calculated rms over the different chosen window sizes which are averaged over all the channels of one event for antenna cluster D30.

Note: Only window sizes which are supported by the ADC module were chosen.

The solid line is mainly characterised by two bumps. This feature is due to the TV transmitter[5] at 62.25 MHz (picture carrier) and 67.75 MHz (audio carrier) in the observed band width. The line synchronisation signal of terrestrial TV programs is emitted every

[5] Transmitter Raichberg, mounted on top of the mountain having the same name in the Swabian Mountains.

63.943 µs and is visible as an enormous burst in the time data. When recording 16k samples about 3 synchronisation bursts are expected and also seen in the data. If no background suppression is performed the synchronisation burst(s) is in the data and increases the rms by chance. By increasing the window size, the spectral resolution increases, too, and the suppression of interferences changes. Figure 3.9 points out that an optimal window size is achieved by using a window length of $n = 2048 = 2\text{k}$ samples. Every larger window size does not improve the suppression of interferences significantly. Only the computation time increases by $n \log_2(n)$, where n is the number of samples.

Chapter 4

Calibration

4.1 Introduction

The recorded data are deconvolved from the frequency characteristics of the electronics and depend on the direction of the incoming signal (characteristics of the antenna). The data have to be absolutely calibrated for comparison with other experiments and with simulations. Additionally, the resulting field strength has to be normalised to the effective bandwidth of the system. The digital methods used in this chapter (e.g. Fourier Transform) are described in detail in sec. 3.4.

This chapter gives a theoretical description of the processed signal chain and describes the procedures of two independently performed absolute calibration methods: End-to-End and Step-by-Step calibration. Furthermore, the frequency dependence of the electronic components used are discussed and the effective bandwidth is calculated.

4.2 Theoretical Description

The theoretical description gives an overview of the formulae used to describe the detector calibration. Thus, characteristics of the electromagnetic field, the antenna, and the signal chain have to be discussed in more detail.

4.2.1 Electromagnetic Field

The energy flux of an electromagnetic field is described by the Poynting vector $\vec{S}\ \left[\frac{\mathrm{W}}{\mathrm{m}^2}\right]$ for free space propagation:

$$\vec{S} = \vec{E} \times \vec{H} \tag{4.1}$$

where $\vec{E}$ is the electric and $\vec{H}$ the auxiliary magnetic field. The emitting radio source is several hundred meters or even kilometres above the receiving antenna, so the far-field approximation for the radio frequency range is valid. The impedance of free space is defined by $\tilde{Z}$:

$$\tilde{Z} = \frac{|\vec{E}|}{|\vec{H}|} = \frac{E}{H} = \sqrt{\frac{\mu_0}{\epsilon_0}} = \mu_0 \cdot c \approx 120\pi\,\Omega \approx 377\,\Omega \tag{4.2}$$

where E and H are the absolute values of the corresponding field and c is the speed of light. Equation 4.1 combined with the far-field approximation and eq. 4.2 results in eq. 4.3.

$$S = \frac{1}{\mu_0 \cdot c} E^2 \tag{4.3}$$

The received power per area $\tilde{P}$ $\left[\frac{\mathrm{W}}{\mathrm{m}^2}\right]$ of an isotropic radiator (emitting power P_{tot}) is described by:

$$\tilde{P} = \frac{P_{\mathrm{tot}}}{4\pi r^2} \tag{4.4}$$

where r is the distance between emitter and receiver.

4.2.2 Antenna

The output power P_{ant} of the receiving antenna follows eq. 4.5.

$$P_{\mathrm{ant}} = A_{\mathrm{eff}}(f, \theta) \cdot S \tag{4.5}$$

The effective area A_{eff} is defined by the geometry of the antenna type used and depends on the frequency f as well as on the zenith angle θ

$$A_{\mathrm{eff}} = \frac{\lambda^2}{4\pi} \cdot G(f, \theta) = \frac{c^2}{4\pi f^2} \cdot G(f, \theta) \; . \tag{4.6}$$

The antenna gain $G(f, \theta)$ is a function of the frequency and the zenith angle. The gain G has to be determined in units of dBi (dB in relation to the isotropic radiator) otherwise eq. 4.6 and 4.5 are not valid. The values for $G(f, \theta)$ have been measured or result from antenna simulations.

The received power per polarisation varies with a $\cos^2(\varphi)$ depending on the azimuth angle φ of the incoming signal.

4.2.3 Signal Chain

On the one hand P_{ant} is mainly characterised by the amplification and attenuation (both are dependent on the frequency) in the various parts of the signal chain and finally results in the P_{ADC}, which is finally digitised (eq. 4.7).

$$P_{\mathrm{ADC}} = P_{\mathrm{ant}} \cdot \frac{a_{\mathrm{amp}}(f) \cdot a_{\mathrm{filter}}(f)}{a_{\mathrm{cable}}(f) \cdot a_{\mathrm{ins}}(f)} \tag{4.7}$$

On the other hand P_{ADC} corresponds to a voltage, due to the impedance of the system (Z) — Ohm's law, and is digitised with a 12 Bit ADC (voltage range: $\pm 0.5\,\mathrm{V}$, see eq. 4.8).

$$P_{\mathrm{ADC}} = \frac{U_{\mathrm{ADC}}^2}{Z} = \frac{\mathrm{ADC}^2}{a_{\mathrm{ADC}}^2(f) \cdot Z} \tag{4.8}$$

Here $a_{\mathrm{ADC}} = \frac{4096}{1\mathrm{V}}$ is the conversion factor and $Z = 50\,\Omega$ is the impedance of the system.

In addition, P_{ADC} passes through the complete system and corresponds to the raised and attenuated P_{ant} signal (see eq. 4.5 and 4.7). The LNA ($a_{\mathrm{amp}}(f)$) and band-pass filter ($a_{\mathrm{filter}}(f)$) amplify the signal, whereas the cables ($a_{\mathrm{cable}}(f)$) and the insertion loss of the LPDA ($a_{\mathrm{ins}}(f)$) attenuate it. The frequency dependence of the amplification functions $a(f)$ have been measured in the laboratory.

4.2.4 Calibration Equation

An overall calibration equation is obtained by combining the discussed formulae. The energy flux of the electromagnetic field (eq. 4.3) is received by each of the observed polarisation channels (eq. 4.5). The resulting power P_{ant} is manipulated in the signal chain and digitised (eq. 4.8 and 4.7). Finally, the combination of eq. 4.3 and eq. 4.5 — 4.8 yields to the calibration equation 4.9.

$$\left|\vec{E}_{\mathrm{LPDA}}\right| = \sqrt{\frac{\tilde{Z}}{Z}} \cdot \frac{a_{\mathrm{cable}}(f) \cdot a_{\mathrm{ins}}(f)}{a_{\mathrm{amp}}(f) \cdot a_{\mathrm{filter}}(f) \cdot a_{\mathrm{ADC}} \cdot \sqrt{A_{\mathrm{eff}}(f,\theta)}} \cdot \mathrm{ADC} \tag{4.9a}$$

$$= 2f\sqrt{\frac{\mu_0 \pi}{Zc}} \cdot \frac{a_{\mathrm{cable}}(f) \cdot a_{\mathrm{ins}}(f)}{a_{\mathrm{amp}}(f) \cdot a_{\mathrm{filter}}(f) \cdot a_{\mathrm{ADC}} \cdot \sqrt{G(f,\theta)}} \cdot \mathrm{ADC}$$

$$= \frac{1}{\mathrm{corr}(f)} \cdot \frac{1}{\sqrt{G(f,\theta)}} \cdot \mathrm{ADC} \tag{4.9b}$$

$$\frac{1}{\mathrm{corr}(f)} = 2f\sqrt{\frac{\mu_0 \pi}{Zc}} \cdot \frac{a_{\mathrm{cable}}(f) \cdot a_{\mathrm{ins}}(f)}{a_{\mathrm{amp}}(f) \cdot a_{\mathrm{filter}}(f) \cdot a_{\mathrm{ADC}}} \tag{4.9c}$$

Thus, the $\mathrm{corr}(f)$ values are the correction values to calibrate the amplitude spectrum in a frequency dependent way. The End-to-End and Step-by-Step calibration methods use different aspects of the calibration equation 4.9 to convert ADC counts into field strength [μV/m] and are discussed in the following.

4.3 End-to-End Calibration

The End-to-End calibration method measures the frequency dependent correction values for the complete system. A reference source was placed at a well-known position above the LPDA and the measured spectrum was corrected by taking the propagation of the emitted signal and the direction sensitivity of the antennas into account.

4.3.1 Configuration

The signal chain of the calibration reference system consists of several parts: A biconical antenna (VSQ 1000), an amplifier (DPA 4000), and a signal generator (RSG 1000). All three parts are commercial products of the Schaffner company (Augsburg) and are used for the amplitude calibration of LOPES30 [Hake 06, Nehl 08b]. The biconical antenna is linearly polarised and has a nearly constant directivity close to its main lobe. This fact is important since it results only in a small loss, if the radio source is slightly off target. The reference source is originally designed for the frequency range of $300-1000\,\mathrm{MHz}$, but the antenna is specified and accredited for the broader frequency range of $30-1000\,\mathrm{MHz}$ as well. The signal generator was set to a rate of $1\,\mathrm{MHz}$ and produces an accredited harmonic wave spectrum. The calibrated amplitude spectrum in a distance of $10\,\mathrm{m}$ to the source is given by the manufacturer and is illustrated in figure 4.1 for the observed frequency range.

The centre of the reference source was mounted vertically in a distance of $r \approx 11\,\mathrm{m}$ above the centre of the LPDA and aligned in parallel to the measured polarisation.

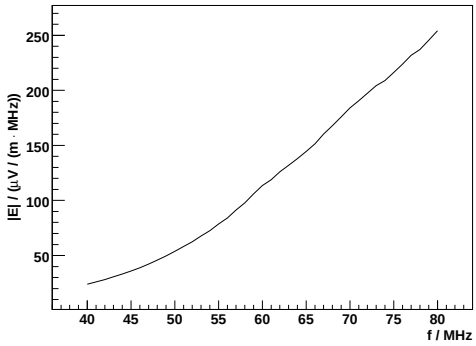

Figure 4.1: The emitted field strength in a distance of 10 m from the reference source given by the manufacturer (linear interpolation).

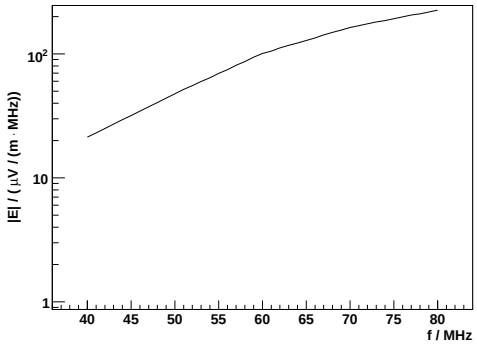

Figure 4.2: The resulting field strength after propagation from the reference source to the LPDA in logarithmic scale (linear interpolation).

80 data records with a time period of $\Delta t = 16,384 \cdot 12.5\,\text{ns} = 204.8\,\mu\text{s}$ were taken at antenna cluster D30 for each of the 8 channels. During the measurement the alignment of the reference source was ensured by tightening long lines which were fixed at the poles of the biconical antenna.

4.3.2 Analysis

LPDA Direction Sensitivity

On the one hand, the electric field expected at the LPDA $\left|\vec{E}_{\text{LPDA}}\right|$ is calculated by taking into account the propagation of the signal from the biconical antenna to the LPDA. Free space propagation is assumed for simplification. The resulting amplitude spectrum is illustrated in figure 4.2.

On the other hand, the direction sensitivity of the LPDA $G_{\text{eff}}(f, \theta)$ has to be considered to perform a general amplitude calibration. The direction dependent gain G_{eff} of the electric field plane ($\vec{E}$ plane) is shown in fig. 4.3.

The calibration equation 4.9 changes under these circumstances:

$$\left|\vec{E}_{\text{LPDA}}\right| \cdot \sqrt{G_{\text{eff}}(f, \theta)} = \frac{1}{\text{corr}(f)} \cdot \text{ADC}\,. \tag{4.10}$$

Determination of Correction Values

Only recorded data with no ADC overflow were analysed in the following. The frequency dependent correction values $\text{corr}(f)$ convert the Fourier transformed ADC data into an absolute amplitude calibrated spectrum and (applying inverse FFT) into absolutely calibrated time data, respectively. The calibrated harmonic wave spectrum of the reference source consists of 1 MHz spaced points. Figure 4.1 shows these points connected by a straight line. A typical un-calibrated spectrum is presented in fig. 4.4. The included upper right plot shows a zoom in on the frequency range (linear scale) of the discrete

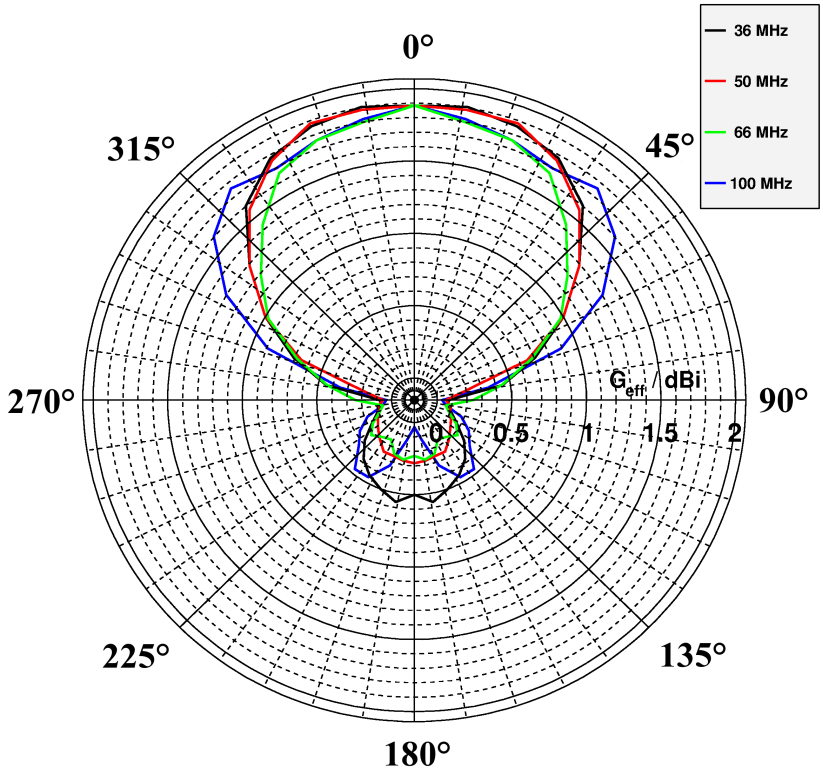

Figure 4.3: Direction sensitivity of the LPDA for different zenith angles θ of the electric field $\vec{E}$ plane (data derived from [Krom 08]).

calibration signal. The small peaks are broadened, due to the limited spectral resolution of $\Delta f = \frac{40\,\mathrm{MHz}}{2 \cdot 16{,}384\,\mathrm{samples}} = 1.22\,\mathrm{kHz}$.

Each correction value $\mathrm{corr}(f)$ is determined by the ratio of the expected signal $S_{\mathrm{exp}}(f)$ to the measured signal $S_{\mathrm{mes}}(f)$ in units of $\left[\frac{\mu\mathrm{V}}{\mathrm{m} \cdot \mathrm{MHz}}\right]$ as given in eq. 4.11.

$$\mathrm{corr}(f) = \frac{S_{\mathrm{mes}}(f)}{S_{\mathrm{exp}}(f)} = \frac{\mathrm{FFT}\{\mathrm{ADC}\}}{\left|\vec{E}_{\mathrm{LPDA}}\right| \cdot \sqrt{G_{\mathrm{eff}}(f,\theta)}} \tag{4.11}$$

Additionally, an integral of the peak is correlated to the received field strength, due to the broadening of the calibration peaks (spectral resolution). The correction values for $f_{\mathrm{low}} = 40\,\mathrm{MHz}$ and $f_{\mathrm{high}} = 80\,\mathrm{MHz}$ were not calculated in order to exclude edge effects of the band-pass filter, due to the steep fall off at the boundary frequencies.

Quality Cuts on Correction Values

The distribution of all the $1/\mathrm{corr}(f)$ values in a frequency range from $41 \leq f \leq 79$ shows a long tail (see fig. 4.5). This points to falsely determined correction values. RFI sources from machines or man-made radio (e.g. police radio) during the measurement are responsible for low values. The background signal is constructively overlaid with

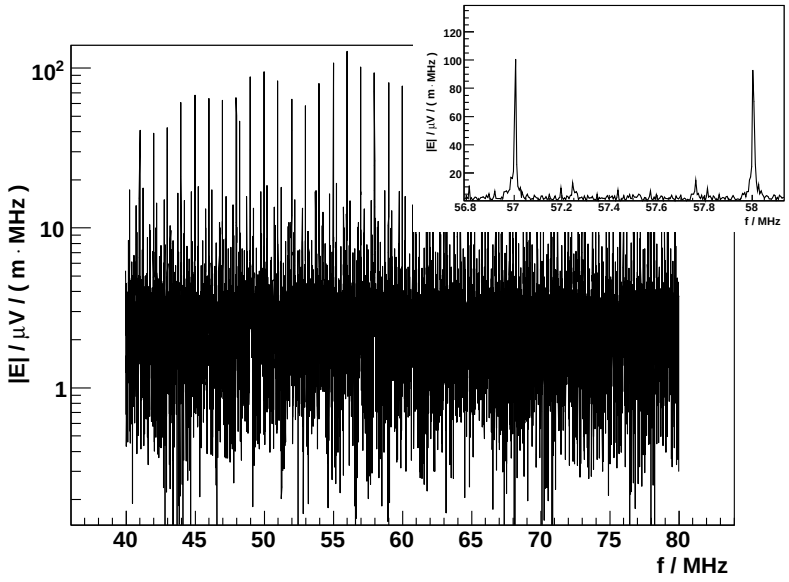

Figure 4.4: The un-calibrated harmonic wave spectrum (steps of 1 MHz) of the reference source measured with the LPDA in logarithmic scale. The upper right spectrum is zoomed in the frequency axis and shows the broadened peaks due to the spectral resolution.

the calibration peak. Thus, the integral is overestimated and $1/\mathrm{corr}(f)$ decreases. In contrast, if the polarisation alignment between reference source and measured channel varies, due to a rotation of the biconical antenna, $1/\mathrm{corr}(f)$ increases. A quality cut that rejects all the values that fulfil $1/\mathrm{corr}(f) > 2.5$ is applied to the data (dashed line in fig. 4.5) to suppress this effect.

The frequency dependence of the rejected correction values are pictured in fig. 4.6. The distribution points out that especially for $f > 70\,\mathrm{MHz}$ the $1/\mathrm{corr}(f)$ are falsely determined as it appears as a bump in the figure. The illustrated statistical error indicates the fluctuations during the measurement. Only half of the observed frequency peaks ($f > 70\,\mathrm{MHz}$) of all the calibration measurements appear in fig. 4.6, the other half of the determined correction values are accepted by the quality cut. Further measurements are necessary to investigate systematic effects in more detail.

4.3.3 Results

The accepted $1/\mathrm{corr}(f)$ values versus frequency are pictured in fig. 4.7. The $1/\mathrm{corr}(f)$ error bars are determined by statistics, while the uncertainty in frequency is fixed to $\sigma_f = \pm 0.5\,\mathrm{MHz}$, due to the frequency resolution of the reference spectrum. The average statistical uncertainty of all the accepted $\mathrm{corr}(f)$ values is $\bar{\sigma}_{\mathrm{corr,stat}} < 1.5\,\%$. The influence of RFI and noise (background fluctuations) is very low, with respect to the applied quality cut.

The absolute uncertainties σ_{corr} combine several error sources. The main part is given by the accredited reference source with a systematic error of $\sigma_{\mathrm{ref,sys}} = 2.5\,\mathrm{dB}$ from the

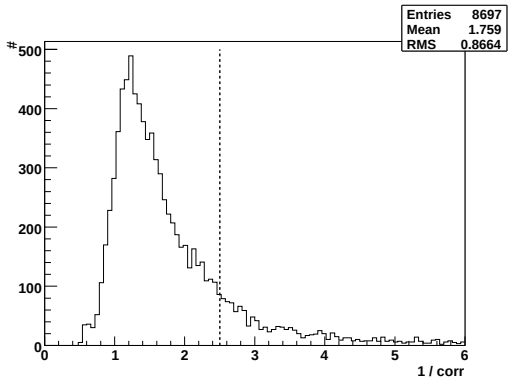

Figure 4.5: The 1/corr(f) distribution of all the analysed records with the applied quality cut (dashed black line).

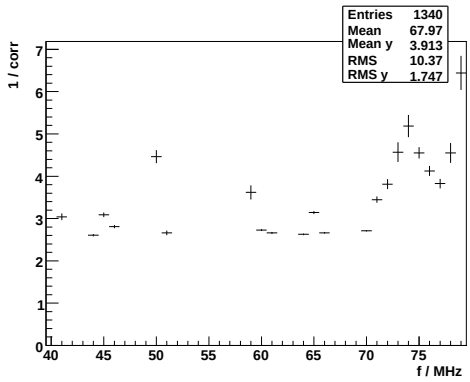

Figure 4.6: The rejected 1/corr(f) values with statistical error versus frequency ($\sigma_f = \pm 0.5\,\mathrm{MHz}$).

manufacturer. In addition, the systematic error $\sigma_{\mathrm{G,sys}}$ of the antenna gain $G(f, \theta)$ was estimated at $\sigma_{\mathrm{G,sys}} = 0.8\,\mathrm{dB}$, as well as the uncertainty of the amplitude distribution (band-pass filter and LNA) $\sigma_{\mathrm{filter+amp,sys}} = 0.2\,\mathrm{dB}$ [Krom 08]. The contribution of the square root of G (see eq. 4.10) results in a $\sigma_{\sqrt{\mathrm{G}},\mathrm{sys}} = 0.4\,\mathrm{dB}$. Therefore, the overall uncertainty results in $\sigma_{\mathrm{corr}(f)} = 44.4\,\%$ for the End-to-End calibration method.

The corr(f) distribution with an overall error band is shown in figure 4.8. The spectrum is clearly dominated by the large uncertainty of the reference source. A negative slope of the correction values is visible, as expected by the frequency dependent attenuation of the cables used.

Half of the measured correction values are rejected ($f > 70\,\mathrm{MHz}$) and hint to systematic problems of the experimental set-up. Furthermore, the resulting correction values, illustrated in fig. 4.8, show ripples within their uncertainties, which might be related to the procedure and its configuration. The presented analysis of the End-to-End calibration method is based on only one measurement. Calibration measurements have to be repeated on a regular time base to investigate seasonal, environmental, and systematic effects in detail and will help to increase the statistics and reduce the uncertainty of the correction values.

Conclusion

The End-to-End calibration method is a good instrument to calibrate the complete system including environmental effects. With respect to the surrounding conditions (area, weather, etc), the mounting of the reference source becomes challenging. Another reference source with much lower systematic uncertainty is needed to improve this calibration as a stand-alone method. Furthermore, if single components of the signal chain are replaced by spares or upgraded modules, the complete system has to be calibrated again. The End-to-End calibration is a sufficient tool to control and to estimate the absolute environmental effects on the system.

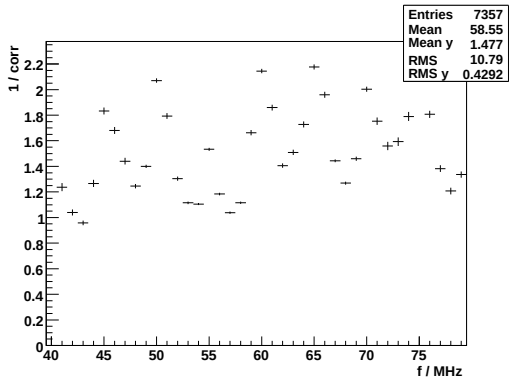

Figure 4.7: The frequency dependency of the accepted correction values with their statistical error. The frequency uncertainty is fixed to $\pm 0.5\,\mathrm{MHz}$ due to the characteristics of the reference antenna.

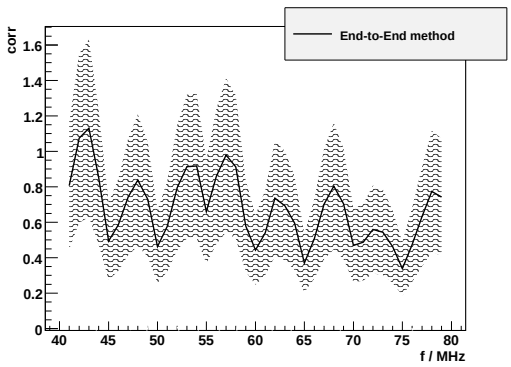

Figure 4.8: The resulting correction values are connected by a straight line. The shown error band corresponds to the absolute uncertainty obtained by this method.

4.4 Step-by-Step Calibration

The Step-by-Step calibration method takes into account each component used and determines the overall correction values $\mathrm{corr}(f)$. Therefore, each part of the electronics is characterised by its amplitude and phase spectrum. The advantage of the LPDA is the real $50\,\Omega$ impedance at the output of the antenna. Thus, the calibration equation 4.9 is used directly. The $\mathrm{corr}(f)$ values are defined by equation 4.9c and result in the following:

$$\mathrm{corr}(f) = \frac{1}{2f} \cdot \sqrt{\frac{Zc}{\mu_0 \pi}} \cdot \frac{a_{\mathrm{amp}}(f) \cdot a_{\mathrm{filter}}(f) \cdot a_{\mathrm{ADC}}}{a_{\mathrm{cable}}(f) \cdot a_{\mathrm{ins}}(f)} \,. \tag{4.12}$$

The equation shows that $\mathrm{corr}(f)$ is proportional to the amplification or the attenuation spectra of the LNA, the band-pass filter, the cables, and the insertion loss of the LPDA. The constant factor is determined by the physical constants (μ_0 and c) and the conversion constants ($Z = 50\,\Omega$, $a_{\mathrm{ADC}} = \frac{4096}{1\,\mathrm{V}}$).

4.4.1 Component Characteristics

The absolute gain spectra of all the components are shown in figure 4.9. The characteristics of the LPDA, the band-pass filter and the pre-amplifier have been determined in a laboratory measurement [Krom 08]. Positive values correspond to amplification, whereas negative values attenuate the signal. The overall sum is shown by the solid red curve.

Cable Attenuation

Each polarisation of the LPDA is connected via a RG213 cable of 100 m length. An additional RG58 cable of 4 m length connects the incoming RG213 cable to the filter board within the VME crate. The frequency dependent attenuation was taken from the

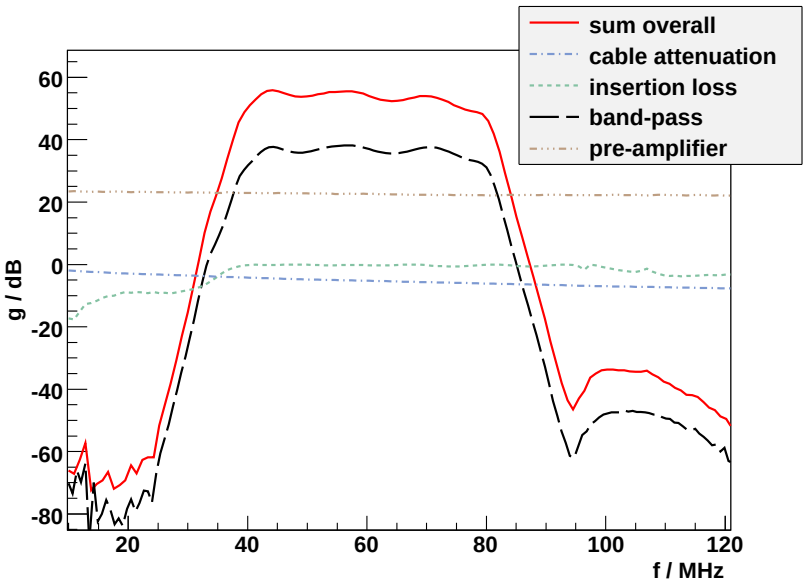

Figure 4.9: Gain distribution of the different electronic components used in the signal chain of LOPES$^{\mathrm{STAR}}$.

data-sheet[1]. The attenuation is documented in steps of 10 MHz. A linear interpolation is performed for frequencies in between. The combined attenuation of the RG213 and RG58 cable a_{cable} is illustrated by the dot-dashed blue line in figure 4.9. The calibration software handles each length of the cables used separately.

Insertion Loss

One requirement of the antenna development was a low insertion loss and therefore, a sufficient matching between the impedances of the antenna and the electronics. This is necessary to transfer all of the received signals into the system. Otherwise the reflected part of the signal is transmitted to the antenna. The reflection coefficient S_{11} describes the mismatch between the impedances of the antenna and the system. The insertion loss a_{ins} is directly related to the reflection coefficient by $a_{\mathrm{ins}} = 1 - |S_{11}|^2$ and marked by a dashed dark green line in fig. 4.9.

Band-pass

The system response function is mainly dominated by the applied $40-80$ MHz band-pass filter. The gain of the filter a_{filter} is shown in fig. 4.9 and marked with the long-dashed black line. A ripple in the observed frequency range is visible, corresponding to the filter design. On the one hand, the filter steepness has to be very high to suppress RFI from adjacent transmitter bands (e.g. FM-band $88 - 108$ MHz). The filter is a combination of high and low pass filter with a steepness of ≈ 65 dB/octave at the barrier frequencies

[1] manufacturer: Bedea

(see fig. 4.9). On the other hand, the chosen filter design has to match the required real impedance of 50 Ω. Both criteria have to be balanced and result in the ripple.

Pre-Amplifier

The Low Noise pre-Amplifier (LNA) shows a smooth gain spectrum a_{amp} over a large frequency range as shown in fig. 4.9 (dashed and triple dotted light brown line). This broadband amplifier also matches the required 50 Ω at the connection to the band-pass filter. The limiting factor of such a LNA is the noise temperature of the electronics. The electronics noise temperature is more than one order of magnitude lower than the mean temperature of the galaxy [Krom 08]. This is proven by the fact, that, at best conditions, the galactic noise is visible in the data as presented in sec. 5.2.

4.4.2 Results

As described in section 4.3.3, the major uncertainty of the calibration is related to the reference source used and the knowledge of the receiving antenna. The Step-by-Step calibration method uses the LPDA characteristics derived from model measurements and the amplitude spectrum of the electronic components measured in a laboratory. The estimated error of the gain G of the LPDA corresponds to $\sigma_{\mathrm{G,sys}} = 0.8\,\mathrm{dB}$. The accuracy of the $\mathrm{corr}(f)$ determination is limited by the equipment used for measuring the components in the Step-by-Step calibration. The error of the combined measurement of band-pass filter and LNA was estimated at $\sigma_{\mathrm{filter+amp,sys}} = 0.2\,\mathrm{dB}$. The uncertainty of the insertion loss is not explicitly mentioned, but is considered in the uncertainty of the antenna gain $\sigma_{\mathrm{G,sys}}$.

The overall sum of the correction values determined with the Step-by-Step calibration method is illustrated in figure 4.10 with an error band indicating the absolute uncertainty. A detailed discussion of the comparison of both presented calibration methods is given in the following section.

The Step-by-Step calibration method is flexible and an independent procedure. Single components could easily be replaced or added to the signal chain. Furthermore, no overall calibration is necessary. In addition, the antenna characteristics have to be known precisely (necessary for both methods) and might be obtained by simulations or laboratory measurements.

4.5 Comparison and Results

The comparison between the determined $\mathrm{corr}(f)$ values of both calibration methods is shown in figure 4.10. The Step-by-Step uncertainties are limited by the equipment used. The illustrated error bands correspond to the absolute uncertainty of these methods (dashed blue and solid black line). The resulting uncertainty values of the Step-by-Step method are doubled for a better illustration.

The large uncertainty of the End-to-End calibration is dominated by the influence of the reference source used. The resulting ripples might be related to systematic or environmental effects, but that could not be distinguished or analysed in detail due to one performed measurement. Further End-to-End calibration measurements are necessary to investigate such effects in detail with high statistics. Nevertheless, the achieved accuracy

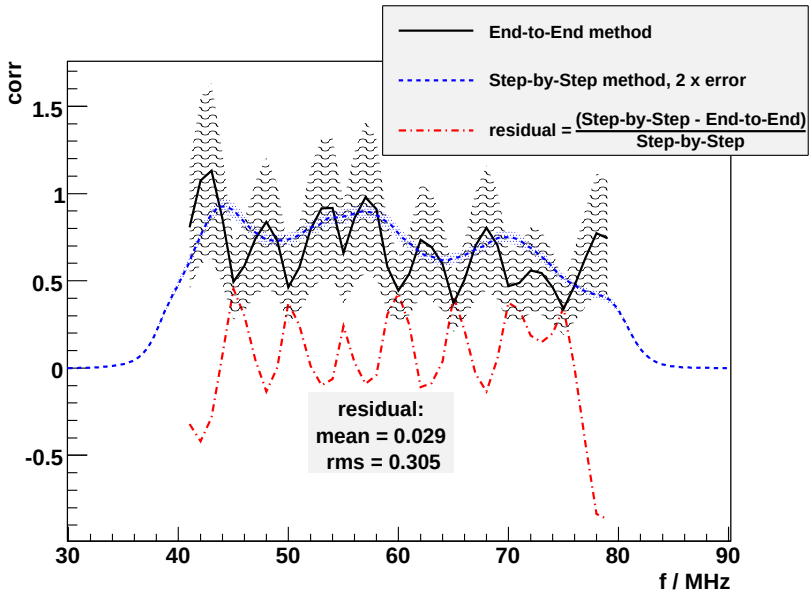

Figure 4.10: The comparison of the End-to-End and Step-by-Step calibration methods. Both methods conform to each other within the estimated uncertainties. The resulting uncertainty of the correction values of the Step-by-Step method are doubled for better comparison.

is sufficient enough to verify both methods and point out, that the performed calibration procedures work well.

Both methods almost match within the resulting uncertainties. A more quantitative way to analyse this is given by the residual. This is defined by the difference of both corr(f) values for each frequency as pictured in fig. 4.10 (dashed-dotted red line). The resulting mean of 0.029 describes the good correspondence of both methods. Taking the error of $\approx 30\,\%$ into account the systematic offset is negligible. In conclusion, the investigations of calibration processes have shown that the system is well-understood, due to the same results from different methods.

Calibration procedures have to be performed on a regular time basis to monitor the stability and performance of a detector. A cross-check by operating different calibration methods is important. Only a combination of different approaches will help to understand the systematics of the procedures and the detector.

4.6 Effective Bandwidth

A comparison of absolutely calibrated radio emission of cosmic rays with results from other experiments has to be performed on a comparable basis. Different detectors measure different bandwidths. The first experiments on that field measured a bandwidth of $\Delta f_{\mathrm{exp}} = 2.45\,\mathrm{MHz}$ [Jell 65]. The measured and calibrated field strength values were divided by the effective bandwidth Δf_{eff} of their system. This normalisation of the mea-

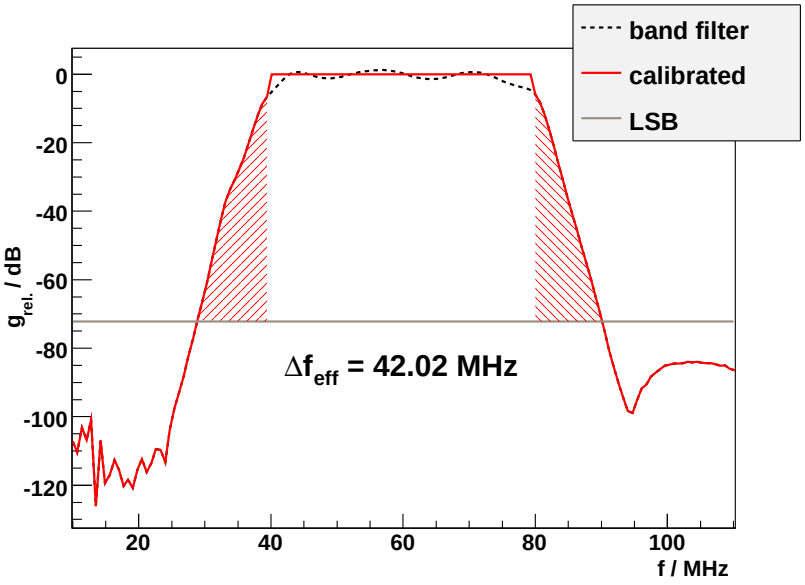

Figure 4.11: The calculation of the effective bandwidth of LOPES$^{\mathrm{STAR}}$. The relative gain $g_{\mathrm{rel.}}$ is related to the normalised gain to the tranmission range of the band-pass filter.

sured signal is valid as long as $\Delta f_{\mathrm{exp}} \ll \Delta f_{\mathrm{theo}}$ is fulfilled, where Δf_{theo} is the expected bandwidth of the radio signal from theory.

The effective bandwidth Δf_{eff} is defined by the following formula:

$$\Delta f_{\mathrm{eff}} = \int_0^\infty g_{\mathrm{rel}}(f)\, df \tag{4.13}$$

where $g_{\mathrm{rel}}(f)$ is the amplification spectrum of the band-pass filter after calibration. Figure 4.11 shows the band-pass filter characteristics (dashed black line), normalised to the transmission range of the band-pass filter ($40-80\,\mathrm{MHz}$), and additionally the correction for the ripple (solid red line). The effective bandwidth of LOPES$^{\mathrm{STAR}}$ is calculated by using eq. 4.13 and results in $\Delta f_{\mathrm{eff}} = 42.02\,\mathrm{MHz}$.

The influence of the antenna in this context is negligible, due to the fact that the LPDA acts as a first order band-pass with a barrier frequency of $30-90\,\mathrm{MHz}$ [Krom 08]. The mean gain of the band-pass filter of about 37 dB dominates the system.

The integration limits are given by the Least Significant Bit (LSB[2]). The ADC used digitises a voltage range of $\pm 0.5\,\mathrm{V}$ with a resolution of 12 Bit. The LSB limit translated to dB results in $g_{\mathrm{rel,LSB}} = -20 \cdot log_{10}\left(2^{12}\right) = -72.2\,\mathrm{dB}$ (solid grey line in fig. 4.11).

Sub-sampling requires a sampling rate twice the highest frequency of interest. The barrier frequencies of the band-pass filter ($-6\,\mathrm{dB}$) were designed at 40 MHz and 80 MHz as shown in figure 4.11. Therefore, the effective bandwidth of the filter is about 5 % larger. Frequencies beyond the barrier frequencies are convoluted in the frequency range

[2] A voltage signal lower than 1 LSB $= \frac{1\,\mathrm{V}}{12\,\mathrm{Bit}} = \frac{1\,\mathrm{V}}{4096} = 244\,\mu\mathrm{V}$ corresponds to 1 ADC count and is stored in the least bit.

of interest (red shaded area in fig. 4.11). This 5 % effect is almost negligible due to the estimated uncertainty of the environmental effects on the LPDA.

Future developments of band-pass filters have to take into account that the barrier frequencies are equal to the LSB limit (of the ADC module used). Otherwise, parts of the frequency spectrum will be convoluted into the base band and increase the uncertainties in the reconstruction and in the calibration.

4.7 Calibration of LOPES^{STAR}

The results from the comparison of different calibration methods showed that the electronics and the LPDA characteristics are understood. The data shown in units of $\frac{\mu V}{m}$ are calculated in the following way:

- The arrival direction (φ, θ) is reconstructed by using clearly correlated time pulses on the basis of single antenna clusters.
- The direction sensitivity of the antenna is taken into account.
- The determined corr(f) values (Step-by-Step method) are applied.
- The inverse Fourier transform results in the absolutely calibrated signal in the observed bandwidth per channel (polarisation) — $|\vec{E}_{\mathrm{NS}}|$ and $|\vec{E}_{\mathrm{EW}}|$ $\left[\frac{\mu V}{m}\right]$
- The normalised signal is defined by dividing the calibrated signal by the effective bandwidth Δf_{eff} — $\epsilon = \frac{|\vec{E}|}{\Delta f_{\mathrm{eff}}}$ $\left[\frac{\mu V}{m \cdot \mathrm{MHz}}\right]$

The total field strength corresponds to the vectorial addition of the absolutely calibrated signals of the north-south & east-west polarised components of the electric field and is defined by:

$$|\vec{E}| = \sqrt{|\vec{E}_{\mathrm{NS}}|^2 + |\vec{E}_{\mathrm{EW}}|^2}\,. \tag{4.14}$$

The applied correction for the direction sensitivity of the LPDA also takes into account the undetected field strength of the vertical polarised component of the signal. Whereas the uncertainty of the reconstructed field strength increases with increasing zenith angle, due to large attenuation resulting from the direction sensitivity of the antenna for high zenith angles.
Note: The calibration method, due to the LPDA characteristics, is limited to zenith angles $\theta < 60\,^\circ$ [Krom 08].

The absolute uncertainty of the field strength is estimated at $\sigma_{|\vec{E}|} = 7.2\,\%$, due to the environmental effects of the LPDA of $\sigma_{\sqrt{\mathrm{G}},\mathrm{sys}} = 0.4\,\mathrm{dB}$ and the electronics uncertainties of $\sigma_{\mathrm{filter+amp,sys}} = 0.2\,\mathrm{dB}$ (compare with the error discussions in section 4.4 and 4.3).

Chapter 5

Self-Trigger

5.1 Introduction

The main challenge of the LOPES^{STAR} experiment is to provide an independent self-trigger system for the radio emission of high energy cosmic rays. A short overview of the background situations for different antenna clusters is given in the first part of this chapter. The main part is dedicated to the self-trigger system and finally, the obtained results from the correlation analysis based on the reconstruction of KASCADE-Grande are presented.

5.1.1 Analogue Self-Trigger

The LOPES^{STAR} antenna clusters were installed over a time period of 18 months (summer 2005 – winter 2006). The described external trigger from KASCADE-Grande is available since autumn 2006.

In a first step an approach of an analogue electronic self-trigger was developed [Krom 08]. The functionality of the analogue channel trigger is briefly described by the following:

- The RF data are rectified and high & low pass filtered to suppress RFI (compare with Filter II method as described in sec. 3.4.3).
- The envelope signals of the RF data are determined from the north-south and east-west polarisation channel, respectively, and are added up per antenna.
- An adjusted threshold, which is the same for all the antennas, is compared with the combined envelope signals of each LPDA. If the signal exceeds the threshold, the analogue channel trigger condition is fulfilled.

If the detected pulses of all three LPDAs are accepted by this channel trigger then the coincidence constraint of the analogue trigger is performed by taking into account the geometrical configuration (equilateral triangle).

During a time period of 9 months (before the external trigger was ready for use) LOPES^{STAR} was only triggered by the analogue trigger. An offline comparison of the recorded timestamps with the ones recorded by KASCADE-Grande showed no coincidence.

In a next step, only the logical output of the analogue trigger (true or false) was recorded for every sample in the observed time window when an external trigger occurred. The reconstructed KASCADE-Grande events with the highest energies ($E > 5 \cdot 10^{17}$ eV)

were used to find recorded shower signals containing a clearly visible radio pulse in the time domain (expected are about 5 events during one month of data taking).

The shower events found were investigated in detail in order to study the behaviour of the analogue trigger during the observed time window. A shower event is rejected if the analogue trigger signal is false during the recorded time window. A background event is accepted if the analogue trigger signal is already on before the signal of the shower is visible. In addition, a shower event might be recorded by chance. The correct analogue trigger signal (true) corresponds to a trigger signal that is delayed and obviously correlated with the external trigger signal as well as with the observed time signal. The investigations showed that none of the 5 detected strong shower events were accepted by the analogue trigger. The accepted data of the analogue trigger were only background events. The fixed trigger threshold, the background suppression, and the combined envelope signal are not sensitive enough to detect radio signals on the site of the Forschungszentrum Karlsruhe.

5.1.2 Digital Self-Trigger

Further developments or improvements of the analogue trigger were stopped due to the insufficient background rejection and shower acceptance. A new analysis of the falsely accepted background events (analogue trigger) pointed out several disadvantages:

fixed threshold The added up envelope signals are compared with a fixed threshold for all the LPDAs. Each channel (polarisation) of the LPDAs has its own background influence due to the different distances to the background sources which results in an individual noise floor in the time domain. It is not possible to balance the threshold between sufficient background rejection (high threshold) and the detection of radio emission of low energy particles (low threshold).

A dynamic threshold is needed to achieve a trigger rate that is moderate for the electronics used. Therefore, the time signal for each data channel is monitored to determine a dynamic threshold and to take the individual background variations into account.

sum of envelope signals Most of the observed background events are transient signals which are emitted on the site of the Forschungszentrum Karlsruhe. Depending on the arrival direction (azimuth angle) of the background events only one channel detects the main part of the transient signal. The adding up of the envelope signals of the two polarisation channels increases the background signal, which is often much higher in amplitude than the wanted signal of the radio emission.

Each polarisation channel has to be observed separately to reject transient background signals per channel.

background suppression A simple background suppression is not sufficient if only the demodulated RF signal is filtered. A more complex method is necessary to suppress RFI signals (e.g. the median method of the RFI suppression as described in sec. 3.4.4), whereas transient signals have to be characterised and rejected in the time domain.

A detailed investigation of the required conditions of the self-trigger followed. The (digital) self-trigger, as described in the following, is motivated by these results and the listed disadvantages of the previous approach [Asch 07]. Externally triggered data are used to develop and to optimise self-trigger conditions in software to implement it later in a hardware[1] based self-trigger system.
Note: Recorded time windows, due to any given trigger signal, are named **triggered event**. Thus, triggered events can be background events or shower events.

5.2 Background Situation

The background conditions have to be well understood in order to reject falsely accepted background events. These conditions are not equal or constant over time for each LPDA and vary strongly with the detector site. Man-made signals in the MHz frequency range are constantly present or appear frequently from sources like exhausters, passing cars, or air conditioning systems. Furthermore, insufficient shielding of electronics acts as an emitting electromagnetic background source of frequencies in the observed spectrum (e.g. PCs or digital devices emit frequencies related to their internal bus clocks).

Two kinds of background signals have to be distinguished. On the one hand the sources are characterised by peaks in the spectrum due to mono frequent signals (modulated or not). In the time domain the overall noise increases in relation to the signal strength of these sources. On the other hand background sources emit broadband signals which are characterised by pulses in the time domain and result in an offset in the amplitude spectrum (frequency domain).
Note: All the illustrated amplitude spectra in this chapter are calibrated data without RFI suppression.

5.2.1 Forschungszentrum Karlsruhe

Long term measurements and background studies have been performed on the site of the Forschungszentrum Karlsruhe. In figure 5.1 an averaged spectrum illustrates the mono frequent sources in the observed bandwidth for the east-west polarised component of one antenna from cluster D17. The time range of $\Delta t = 600\,\mathrm{s}$ was recorded at noon and clearly shows two TV transmitters (TV: Ch2 and Ch4) and one picture carrier of the TV Ch3. Furthermore, the Industrial, Scientific and Medical (ISM) radio band ($40.66 - 40.70\,\mathrm{MHz}$) at the lower band limit is explicitly visible. The ISM bands[2] were internationally reserved for the use of RF electromagnetic fields for industrial, scientific and medical purposes other than communications.

Another method to analyse and monitor the background is given by the dynamic spectrum. Figure 5.2 shows the amplitude spectrum versus the time of one channel of antenna cluster D30. The horizontal lines correspond to mono frequent signals, whereas vertical lines illustrate broad band background signals at that time.

The industrial environment on the site of the Forschungszentrum Karlsruhe defines more or less the worst conditions for detection of radio emission of high energy cosmic

[1] In this context the hardware is given by a Field Programmable Gate Array (FPGA).
[2] In total 12 frequency bands were defined, spread from the lower MHz up to several GHz (e.g. Bluetooth and IEEE 802.11 (WLAN)).

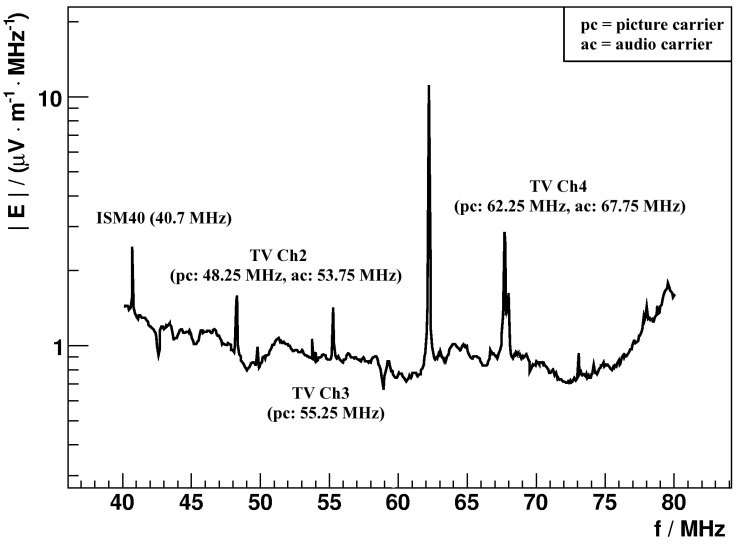

Figure 5.1: An averaged amplitude spectrum (Δt = 600 s, LOPES$^{\mathrm{STAR}}$ cluster D17, antenna 60, east-west channel). Several mono frequent carrier signals of different sources are clearly visible.

rays. The time dependent background variation limits the sensitivity of the complete detector system and the threshold of any self-trigger system. Radio pulses with a sufficient signal-to-noise ratio (snr) are necessary to distinguish between shower signal and background signal. The necessary shower energy was estimated at $E > 5 \cdot 10^{17}$ eV [Krom 08] and corresponds well to the results from the self-trigger and from the analysis chapter of these investigations.

5.2.2 Pierre Auger Observatory

The reverse background situation is given on the site of the Pierre Auger Observatory. The rural region in the southern Argentinian pampa offers a very quiet radio environment. The nearest industrial complexes are several tens of kilometres away and only the nearby roads with lorries and cars or power lines are considered as background sources.

A detector system with 3 antennas, simular to the one on the site of the Forschungszentrum Karlsruhe, was used for background studies. One of the resulting dynamic spectra, shown in fig. 5.3, illustrates the sensitivity of the system to galactic noise (see sec. 5.2.3) due to the cycle of the Earth and the changing field of view (periodic time structure). Almost no mono frequent background sources (horizontal lines) or broadband emission (vertical lines) are recorded in the observed time. A comparison of fig. 5.2 and 5.3 points out that mean radio background on the site of the Pierre Auger Observatory is one order of magnitude lower than on the site of the Forschungszentrum Karlsruhe (note: Different scaling in the two figures).

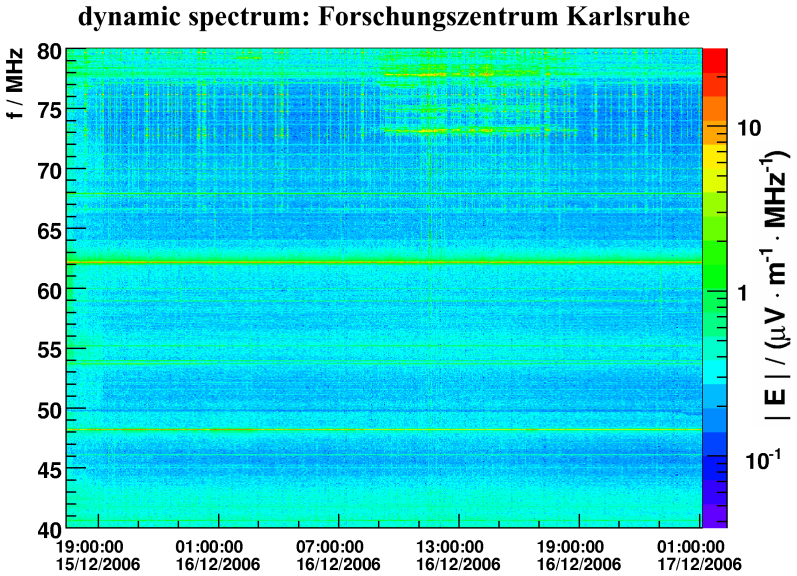

Figure 5.2: The dynamic spectrum in cluster D30 on the site of the Forschungszentrum Karlsruhe. Horizontal lines show mono frequent signals whereas vertical curves correspond to broad band background signals. The amplitude values are coded in colour.

5.2.3 Galactic Noise

If all the man-made background sources are negligible, the galactic noise is the limiting sensitivity factor of a receiving system. The noise temperature $T_{\text{gal.}}$ varies with time due to the observation direction (e.g. possible view into the galactic centre). The Consultative Committee on International Radio (CCIR) has averaged the atmospheric, the industrial and the galactic noise spectrum over long term measurements.

The connection between the temperature of the galactic noise $T_{\text{gal.}}$ and the received power P_{ant} is described by:

$$P_{\text{ant}} = 4 \cdot k_B \cdot T_{\text{gal.}} \cdot \Delta f \tag{5.1}$$

where k_b is the Boltzmann constant and $\Delta f = 40\,\text{MHz}$ is the bandwidth of the system. Equation 5.1 and typical noise temperatures are taken from [Roth 02] and listed in the following.

$$\begin{aligned} 10\,\text{MHz} \quad & T_{\text{gal.}} = (0.2 \ldots 2) \cdot 10^6\,\text{K} \\ 100\,\text{MHz} \quad & T_{\text{gal.}} = (0.6 \ldots 6) \cdot 10^3\,\text{K} \\ 1000\,\text{MHz} \quad & T_{\text{gal.}} = (3 \ldots 7)\,\text{K} \end{aligned}$$

The received power $P_{\text{ant}} = A_{\text{eff}}(f, \theta) \cdot S$ (eq. 4.5) has to be equal to eq. 5.1. Solving this equation, the resulting field strength $|\vec{E}|$ becomes:

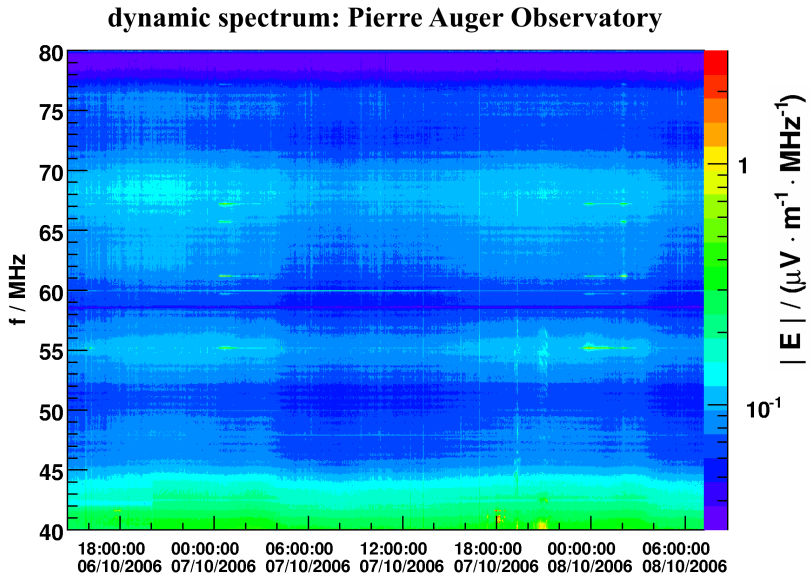

Figure 5.3: The dynamic spectrum of one polarisation of an antenna from cluster D42 on the site of the Pierre Auger Observatory (see fig. 5.2, note: Different scaling).

$$|\vec{E}(f)| = \sqrt{\frac{4 \cdot k_B \cdot \mu_0 \cdot c \cdot \Delta f}{A_{\text{eff}}(f,\theta)}} \cdot \sqrt{T_{\text{gal.}}(f)}$$
$$|\vec{E}(f)| = \sqrt{\frac{16\pi \cdot k_B \cdot \mu_0 \cdot f^2 \cdot \Delta f}{c \cdot G(f,\theta)}} \cdot \sqrt{T_{\text{gal.}}(f)} \tag{5.2}$$

A randomly triggered time window on the site of the Pierre Auger Observatory and a comparison with the galactic noise estimation is illustrated in fig. 5.4. The dashed red line shows the estimated galactic noise (with error band based on the given temperature range), whereas the solid blue line is a straight line fit to the recorded amplitude spectrum. On average the observed spectrum is lower than the expected galactic noise due to the orientation of the field of view of the antenna at the time of measurement. The amplitude variation over time is shown in fig. 5.3.
Note: For the antenna gain $G(f,\theta)$ a mean gain of $\bar{G}(f,\theta = 30\,^\circ) = 4\,\text{dBi} \approx 2.51$ was assumed with respect to the superposition of all the arrival directions.

On the site of the Pierre Auger Observatory the galactic noise is the limiting factor for the sensitivity of the detector used. Whereas on the site of the Forschungszentrum Karlsruhe the background emitted by the industrial environment is on average one order of magnitude higher.

The rural environment in Argentina offers very good conditions to detect the radio emission of high energy cosmic rays. The self-trigger is developed under bad conditions (Forschungszentrum Karlsruhe). The following analysis shows that the background influence is well understood and sufficiently suppressed. The conditions provided within the framework of the Pierre Auger Observatory will improve these methods and will

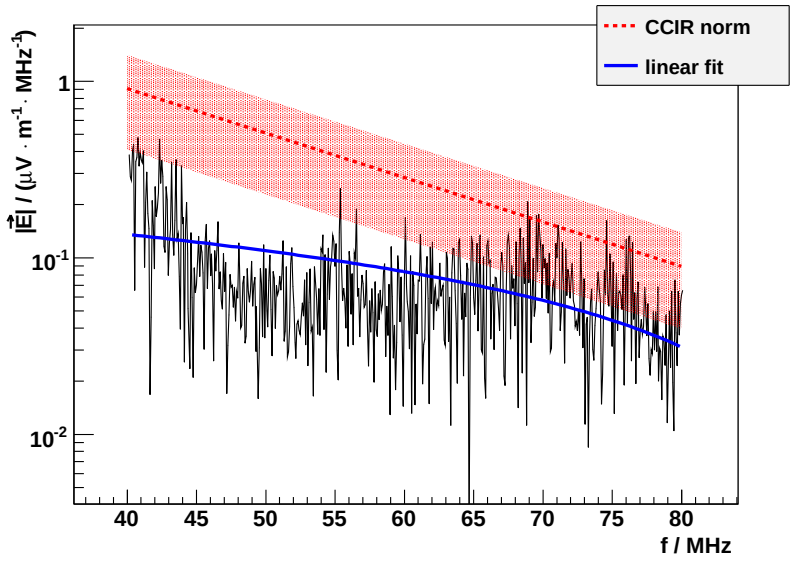

Figure 5.4: The comparison between the calibrated amplitude spectrum (black line), a linear fit to the data (solid blue line) and the estimated galactic noise limit (dashed red line) on the site of the Pierre Auger Observatory.

additionally allow to decrease the threshold of the self-trigger and to detect CRs with lower energy.

5.3 Data Selection

The development and results of the self-trigger system is based on externally triggered data from the KASCADE-Grande experiment.

A pre-selection of data with no ADC overflow was performed to fulfil the sub-sampling criteria. Signals larger than the dynamic range of the ADC module overload the analogue digital converter and an additional flag in the data is set. An up-sampling of these raw data is not possible and recorded events with time samples marked as ADC overflow are rejected for this analysis.

Training data were selected to develop the self-trigger strategy. A data taking period with available KASCADE-Grande reconstruction and quiet background conditions due to Christmas and New Year (holiday season: 2006 — 2007) were chosen. Afterwards, the resulting optimised self-trigger methods were applied to the **verification data** (antenna cluster D17 & D30) to verify the results. A description of the chosen data is summarised in table 5.1.

During the time period of the verification data D17 & D30 the KASCADE-Grande trigger had a total offline time of about one month due to technical problems. The technical configuration of the external trigger generated randomly triggered events during this time which were kept in the data set to increase the statistics of background events.

name of the data set	cluster no.	run no.	period	events
training data	D30	21 – 049	2006-12-12 – 2007-01-07	102,535
verification data D17	D17	12 – 185	2007-08-02 – 2008-01-21	787,203
verification data D30	D30	21 – 454	2006-12-12 – 2008-01-21	1,598,543

Table 5.1: The chosen data to develop (training data) and to verify (verification data D17 & D30) the self-trigger system.

5.4 Trigger Strategy

The self-trigger strategy is organised in a multi-level trigger system consisting of two main parts. First, the trigger constraints for each polarisation (channel) have to reduce the trigger rate on antenna level. A dynamic threshold is continuously compared with the recorded samples to detect a threshold exceeding. Additionally, all the characteristic pulse parameters are determined for the coincident constraints described in the following.

Second, the more complex constraints on cluster level have to accept coincident shower events and to reject background signals. At this stage of the trigger system, all the information about the determined parameters of the channel are available. Data from channels that contain numerous pulses are rechecked for possible shower signals in a given time window. The geometrical configuration of the set-up is used for the coincidence constraint.

A block diagram of the self-trigger system is shown in fig. 5.5 and discussed in the following. The digital methods used in this section (up-sampling, envelope calculation, and RFI suppression) are described in detail in sec. 3.4.

A typically recorded shower event of antenna cluster D30 after applied RFI suppression is illustrated in fig. 5.6. All the channels show a clear detectable pulse signature. Additional noise and small transient signals are visible in the north-south polarisation of antenna 300.

5.4.1 Channel Constraints

Data of each polarisation of the antennas are controlled by the channel trigger. Its challenge is to suppress and to reject background events at an early stage of data taking as well as to select and to accept shower signals. The channel constraints correspond to the central red rectangular as shown in fig. 5.5.

RFI and transient signals are the two main classes of background events. Thus, the continuous sub-sampled data flow per channel has to be split into time windows of $\Delta t = 25.6\,\mu s$ to apply the RFI suppression method with sufficient frequency resolution ($\Delta f \approx 40\,\mathrm{kHz}$).

The remaining background signatures (after RFI suppression) are transient signals which are characterised by a broadband spectrum. The continuous data flow is compared with a dynamic threshold and is accepted if the threshold is exceeded, otherwise the channel is rejected. The following quality and transient cuts will reject the remaining transient background signals. The determined positions in time of the detected pulses are needed for the following coincident constraints.

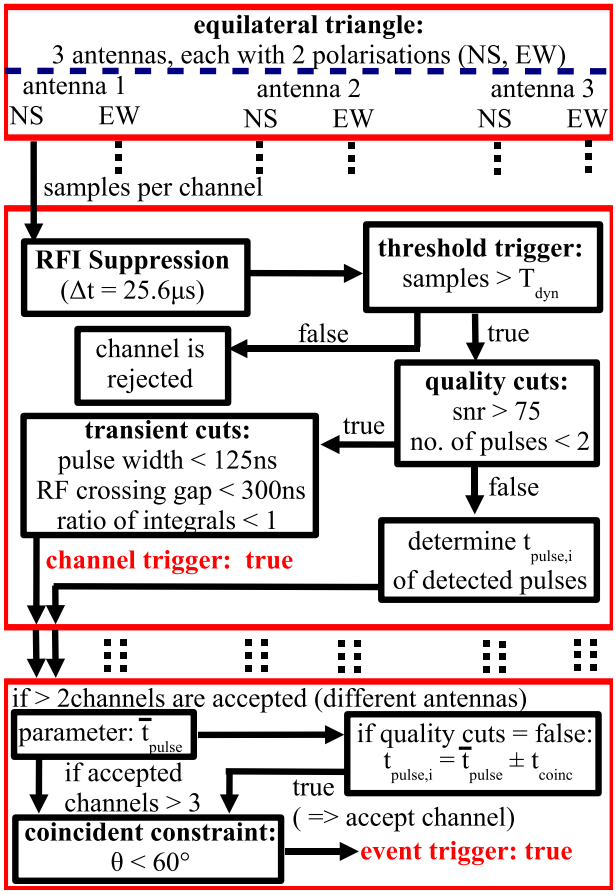

Figure 5.5: Block diagram for the minimal requirements of the self-trigger system. The three red rectangles correspond, from top to bottom, to the geometrical configuration of the antenna cluster, the channel trigger, and the coincidence trigger.

Dynamic Threshold

A dynamic threshold T_{dyn} has to be calculated on the basis of the continuous data flow over a sufficient time range. A time range that is short (several nano seconds) is sensitive to fast background fluctuations and might also miss the shower signal as it occurs as a transient signal. A long time range of hours will be sensitive to day-night-effects, but cannot follow strong background fluctuations (numerous background pulses in a short time range or solar flair).

In fact, the optimal time range for determining the dynamic threshold is strong dependent on the site of the detector (in the range of seconds). In the case of this analysis the externally triggered data have a defined time range. The recorded time windows do not correspond to a continuous data flow and the dynamic threshold is determined on the basis of the complete time window ($\Delta t = 25.6\,\mu\mathrm{s}$).

After RFI suppression the sub-sampled data per channel $s_{\mathrm{sub}}(t)$ are up-sampled $s_{\mathrm{up}}(t)$ and the squared envelope signal (Hilbert method) $s_{\mathrm{env}^2,\mathrm{up}}(t)$ is calculated. The squared data are proportional to the received power and are used to calculate the mean value

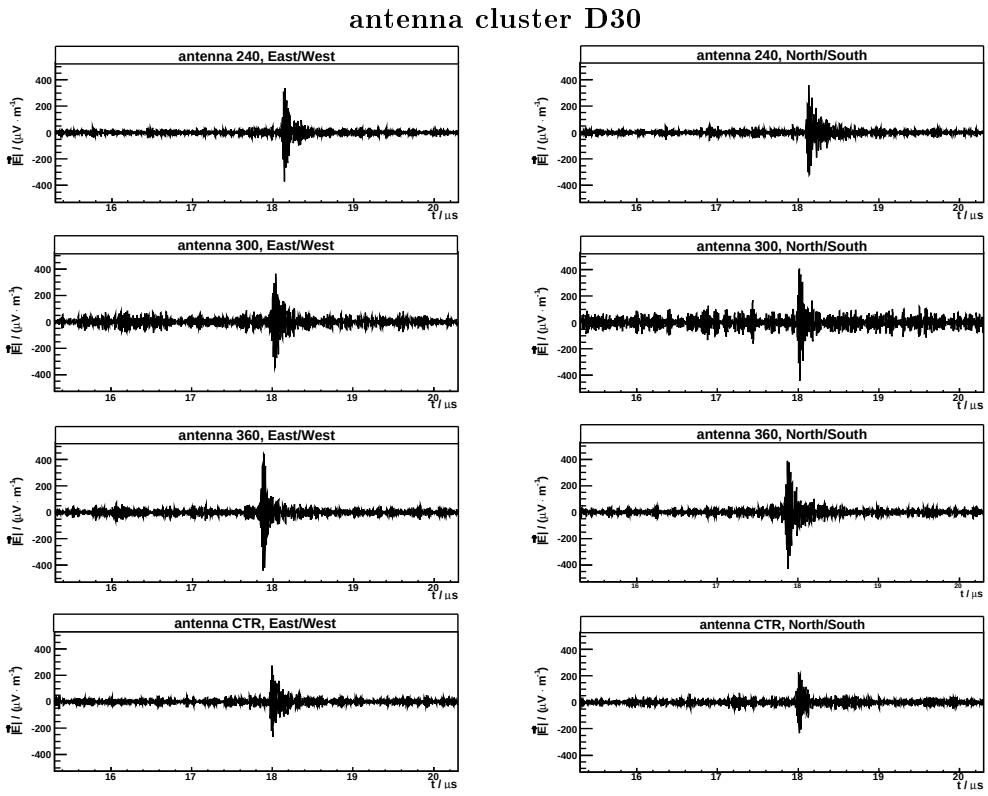

Figure 5.6: Typical time signatures of the radio emission of a cosmic ray air shower after RFI suppression on the site of LOPES$^{\mathrm{STAR}}$ in December 2006 ($E \approx 8 \cdot 10^{17}$ eV, $\theta \approx 60°$, $\varphi \approx 51°$).

$\bar{S}_{\mathrm{mean,env^2,up}}$ and its uncertainty $\sigma_{\bar{S}_{\mathrm{mean,env^2,up}}}$. Therefore, all the time samples (including the pulse itself) are taken into account, due to the fact that the time length of the pulse is much shorter than the recorded time window. A dynamic threshold $T_{\mathrm{dyn,env^2,up}}$ per channel is defined by eq. 5.3 and compared with $s_{\mathrm{env^2,up}}(t)$.

$$T_{\mathrm{dyn,env^2,up}} = S_{\mathrm{mean,env^2,up}} + 4.5 \cdot \sigma_{\bar{S}_{\mathrm{mean,env^2,up}}} \tag{5.3}$$

The empirical factor of 4.5 is iteratively derived from these investigations.

If the dynamic threshold is exceeded, the data of this channel are accepted, otherwise rejected (dynamic threshold trigger).

Quality Cuts

A very rough estimation of the data quality is performed by using the sub-sampled data after RFI suppression. The channel data $s_{\mathrm{sub}}(t)$ are squared and a sliding window over six neighboured time samples is performed to smooth the data. The peak value $\hat{S}_{\mathrm{peak,sub}}$, the mean value $\bar{S}_{\mathrm{mean,sub}}$ and its uncertainty $\sigma_{\bar{S}_{\mathrm{mean,sub}}}$ are determined. An empirically defined threshold $T_{\mathrm{thres,sub}}$ (eq. 5.4) is applied to count the raising edge of the samples exceeding this threshold to estimate the number of pulses per channel in

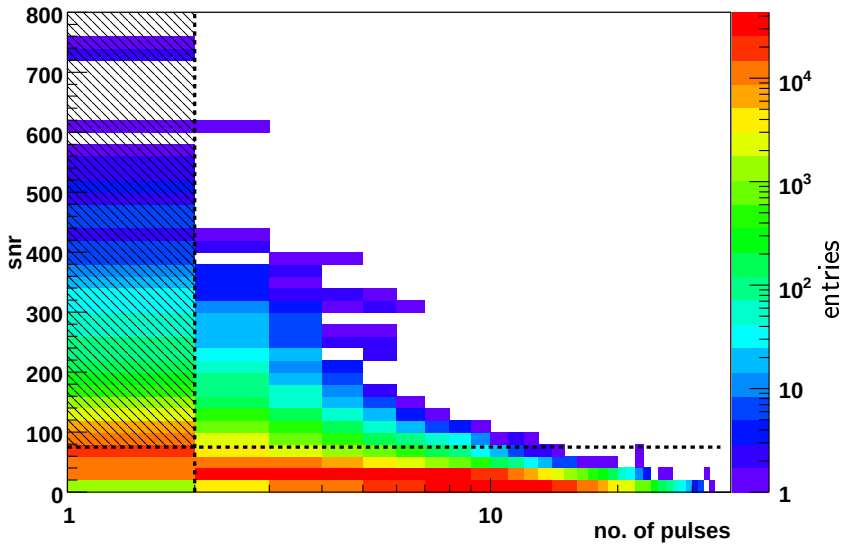

Figure 5.7: The quality cuts applied to each polarisation. The shaded part is accepted and contains all the shower events (one detected pulse), whereas 80 % of the background events are rejected.

that time window.
Note: The threshold $T_{\text{thres,sub}}$ has to be smaller than $T_{\text{dyn,env}^2\text{,up}}$ to count all the pulses.

$$T_{\text{thres,sub}} = \bar{S}_{\text{mean,sub}} + 2 \cdot \sigma_{\bar{S}_{\text{mean,sub}}} + \frac{\left(\hat{S}_{\text{peak,sub}} - \left(\bar{S}_{\text{mean,sub}} + 2 \cdot \sigma_{\bar{S}_{\text{mean,sub}}}\right)\right)}{4.0} \tag{5.4}$$

On the one hand equation 5.4 takes into account the noise due to an offset determined by $\bar{S}_{\text{mean,sub}}$ and $\sigma_{\bar{S}_{\text{mean,sub}}}$ and on the other hand an additional offset depending on $\hat{S}_{\text{peak,sub}}$ is considered to count dominant peaks and not small noisy peaks.

Furthermore, the signal-to-noise ratio (snr) of the squared peak value and the mean value of the complete time data is calculated (snr $\propto$ power).

An illustration of the calculated parameters of the training data is shown in fig. 5.7. A combination of two cuts is introduced to increase the quality of the data (quality cuts) and to reject more than 80 % of the background signals, whereas all the shower events are accepted.

$$\text{snr} > 75 \tag{5.5a}$$

$$\text{no. of pulses} < 2 \tag{5.5b}$$

Equation 5.5a allows to accept pulses with a good signal-to-noise ratio and to reject pulses comparable with noise in the data. Background sources often emit their characteristic signal periodically over a certain time. If several pulses are detected in the recorded time window, the defined cut (eq. 5.5b) rejects this channel.

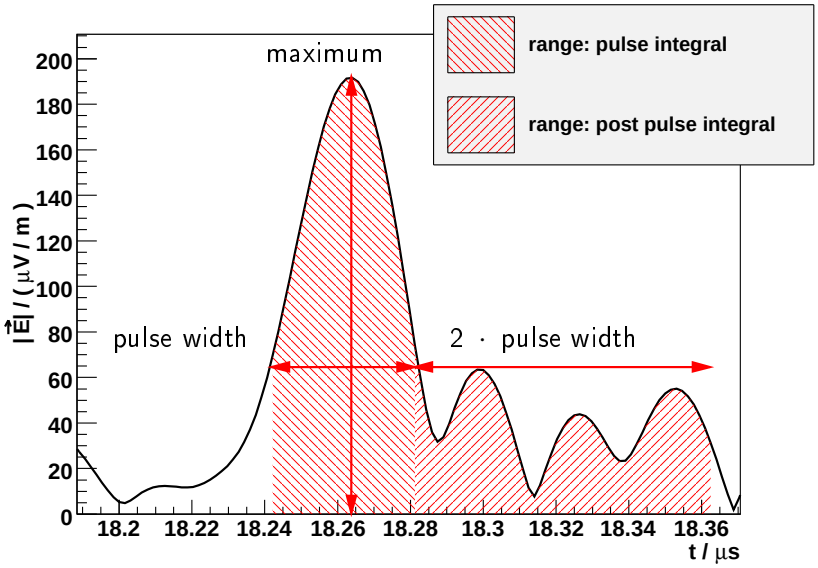

Figure 5.8: A squared envelope signal of one channel (shower event) with the characteristic parameters to distinguish between background and shower events.

Transient Cuts

Each channel that is accepted by the dynamic threshold trigger is processed further to determine the exact number of pulses and their position in time for the coincident constraints. Only the channels that are accepted by the quality cuts are analysed by the following transient cuts.

The remaining pulse in the data has to be characterised by parameters to distinguish between transient signals and radio pulses from high energy cosmic rays. Various pulse parameters were analysed, but only the most adequate ones are discussed here and are illustrated in fig. 5.8 and fig. 5.9.

pulse position The position of the pulse in the time window is determined by the position of the maximum and is used by the coincidence constraint to reject inclined arrival directions. In case of a precise reconstruction of the direction (triangulation) a constant fraction method ($f = 0.5$) is used. A comparison of both methods is presented in the analysis chapter 6.

pulse width The time length of a pulse is defined as the width at one third of the maximum of the peak value. Radio pulses from cosmic ray air showers are expected to be short in time. The recorded detector response function results from a convolution of the original pulse with the filter characteristics of the system. A pulse of a few nano seconds is expanded to a pulse width less than 100 ns due to the $40 - 80$ MHz filter used. In contrast, background sources often consist of longer pulses repeated frequently.

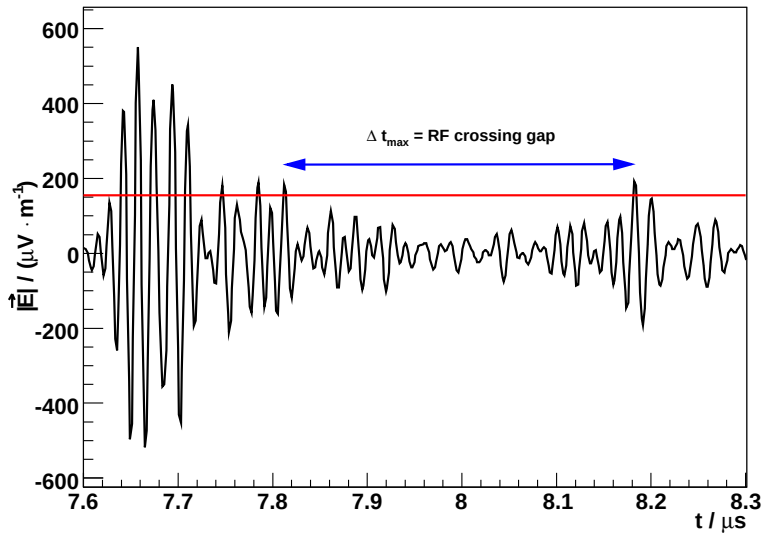

Figure 5.9: Definition of the RF crossing gap parameter. Only the maximal time $\Delta t_{\max}$ between the crossing of two raising edges of the RF signal is determined.

pulse integral The area of the squared envelope signal in the time range of the pulse width is an additional parameter to characterise the signal. The combination of the pulse integral with the pulse width makes a separation between high and flat pulses possible.

post pulse integral An integral of the post pulse time over twice the pulse width characterises well the noise in the data. The factor of two is empirically motivated. A shower event produces a signal as shown in fig. 5.8, whereas background data often include multiple pulses — small pulses around one dominant pulse. The ratio of $\frac{\text{post pulse integral}}{\text{pulse integral}}$ turned out to be a good estimator to reject noisy channels.

RF crossing gap A threshold $T_{\text{RF cross}}$ to determine this parameter is defined by the square root of the dynamic threshold $\left(T_{\text{RF cross}} = \sqrt{T_{\text{dyn,env}^2\text{,up}}}\right)$ and is compared to the up-sampled RF samples. The longest time period between the crossing of two raising edges defines the time value of the RF crossing gap as illustrated in fig. 5.9.

The integral ratio $\frac{\text{post pulse integral}}{\text{pulse integral}}$ versus pulse width is shown in fig. 5.10 for the training data. A concentration of events in the lower right corner is visible. These entries correspond to very wide time pulses, whereas the integral ratio points out that the detected pulses are large. A second peak is indicated in the upper left part of the distribution due to the fact that some background signatures start with a short dominant pulse followed by broad pulses (post pulse integral, ratio > 1). The expected radio signal lies in the intermediate zone corresponding to the green floor shown in figure 5.10.

The parameter RF crossing gap additionally controls the number of pulses in a precise way. Thus, the chosen cut of RF crossing gap $< 300\,\text{ns}$ in combination with the already

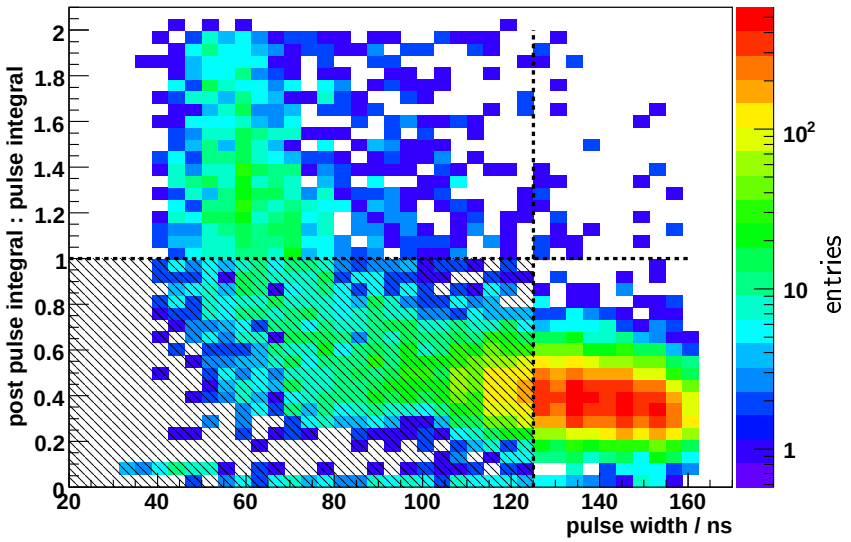

Figure 5.10: Parameters to reject transient background signals. The shaded part is accepted by the transient cuts (see eq. 5.6).

applied quality cuts makes sure that only one dominant pulse is within the recorded time window. The estimated amount of pulses is not unique on the basis of this parameter without considering additional quantities. In the case of background sources emitting pulses very frequently the RF crossing gap parameter always results in small values and does not reflect the recorded multi-pulses.

The discussed parameters as given in eq. 5.6 define the transient cuts. They are optimised to reject transient background signals and to accept shower events.

$$\text{pulse width} < 125\,\text{ns} \tag{5.6a}$$

$$\frac{\text{post pulse int egral}}{\text{pulse integral}} < 1 \tag{5.6b}$$

$$\text{RF crossing gap} < 300\,\text{ns} \tag{5.6c}$$

The channel trigger accepts a channel if the dynamic threshold is exceeded as well as the quality and the transient cuts are fulfilled. After applying the channel trigger to the training data 560 out of 102,535 events are accepted including all the shower events.

5.4.2 Cluster Constraints

In most cases the man-made background signals are emitted and reach the detector in parallel to the surface of the Earth ($\theta > 70°$). The radio emission of CRs reaches the Earth of all the zenith angles ($0° \leq \theta \leq 90°$). Taking into account the direction sensitivity of the LPDA only events with a zenith range $\theta < 60°$ are meaningful for

further analysis. The suppressed signals with $\theta > 60°$ are part of the detector concept to reduce man-made background at an early stage of the signal processing.
Note: The usage of an antenna type with higher sensitivity at larger zenith angles θ allows to increase the sensitivity range for more inclined shower events ($\theta > 60°$).

In a next step the arrival direction of the signal is determined by taking into account the geometry of the antenna cluster. As described in chapter 3 each LPDA is installed on a vertex of an equilateral triangle. This simple geometry allows a fast triangulation and an estimation of the arrival direction (azimuth and zenith).

The time differences of the triggered pulses of three LPDAs are calculated and compared with a given coincidence time t_{coinc} (coincidence trigger). Incoming signals from $\theta = 0°$ (vertical) are recorded simultaneously in all the channels. Signals with a larger zenith angle need more time to propagate through the antenna cluster. The maximal propagation time corresponds to the arrival direction perpendicular to one of the sides of the equilateral triangle. Thus, the coincidence time depends on the zenith and the azimuth angles $t_{\text{coinc}}(\theta, \varphi)$.

A sufficient description of the coincidence time is given by taking into account the height of the triangle, which corresponds to the shortest way to propagate through the antenna cluster. In this case the triangle is approximated as a circle and $t_{\text{coinc}}(\theta)$ follows equation 5.7 for all the azimuth angles.

$$t_{\text{coinc}}(\theta) = \frac{\sqrt{b^2 - \frac{b^2}{4}}}{c} \cdot \sin(\theta) \tag{5.7}$$

where θ is the zenith angle, b is the cluster baseline, and c is the speed of light. Due to the limited sensitivity of the LPDA only zenith angles less than 60° are used.

The cluster constraints of the self-trigger system correspond to the lower red rectangular as shown in fig. 5.5.

Coincidence Trigger

All the channels observe the signals in a defined time window synchronously and continuously. If two or more channels in a triangle with three LPDAs (trigger cell) fulfil the channel trigger conditions, the event is processed further. If one channel is rejected by the channel trigger due to detected background, the second polarisation may be accepted.
Note: It is assumed that the signals are received simultaneously in both polarisations when they reach the antennas.

So far, channels with one dominant pulse of an event are accepted. An estimation of the arrival direction is only possible with events containing one channel of each LPDA (triangulation within a trigger cell). The cosmic ray signal is superposed by the background and channels with multi-pulses are rejected by the channel trigger.

The coincidence trigger calculates the mean position of the pulse (point in time) $\bar{t}_{\text{pulse}}$ of all the accepted channels. The data from channels which are rejected by the quality cuts are rechecked in order to find out whether a clear pulse in the time range of $\bar{t}_{\text{pulse}} \pm t_{\text{coinc}}(\theta = 60°)$ is present or not. If one of the rejected channels contain a pulse in the data, this channel is additionally accepted by the channel trigger. The coincident constraint is applied to all the time positions of pulses of accepted channels.

Applying the coincidence trigger to the training data results in only 68 out of 560 accepted events. An additional cut on the reconstructed arrival direction to rejected events that fulfil $\theta > 60°$ results in a total number of 57 accepted events including the expected shower events.

5.5 Results

5.5.1 Correlations with KASCADE-Grande

The events accepted by the self-trigger are correlated with the reconstructed shower parameters from KASCADE-Grande. In order to perform such a correlation the time delay Δt between the LOPES$^{\mathrm{STAR}}$ and KASCADE-Grande event timestamp has to be known.

The incoming trigger signal is directly connected to the hardware trigger of cluster 13 inside the KASCADE-Grande DAQ. The position in time of this trigger corresponds to the true timestamp t_{event} of the air shower. t_{STAR} results in $t_{\mathrm{STAR}} = t_{\mathrm{event}} + \Delta\bar{t}_{\mathrm{STAR}}$, by taking into account the typical delay $\Delta\bar{t}_{\mathrm{STAR}}$ to transmit the trigger signal to the LOPES$^{\mathrm{STAR}}$ antenna clusters and to take the timestamp.

t_{event} is internally processed by KASCADE-Grande (event building as well as matching with the KASCADE-Array and Piccolo etc.) and delayed by $\Delta\bar{t}_{\mathrm{Grande}}$. This results in the recorded timestamp of KASCADE-Grande $t_{\mathrm{Grande}} = t_{\mathrm{event}} + \Delta\bar{t}_{\mathrm{Grande}}$.

These studies showed that the delays of different LOPES$^{\mathrm{STAR}}$ clusters are approximately equal ($\Delta\bar{t}_{\mathrm{STAR}} \approx \Delta t_{\mathrm{D17}} \approx \Delta t_{\mathrm{D19}} \approx \Delta t_{\mathrm{D30}}$). In addition, $\Delta\bar{t}_{\mathrm{Grande}} \gg \Delta\bar{t}_{\mathrm{STAR}}$ and $\Delta\bar{t}_{\mathrm{STAR}}$ is negligible. The measured coincidence time $\Delta t_{\mathrm{coinc}}$ results in:

$$\begin{aligned}
\Delta t_{\mathrm{coinc}} =& t_{\mathrm{Grande}} - t_{\mathrm{STAR}} && \text{(5.8a)}\\
=& t_{\mathrm{event}} + \Delta\bar{t}_{\mathrm{Grande}} - (t_{\mathrm{event}} + \Delta\bar{t}_{\mathrm{STAR}}) && \text{(5.8b)}\\
\approx& \Delta\bar{t}_{\mathrm{Grande}} && \text{(5.8c)}\\
=& (819778.269 \pm 0.656)\ \mu\mathrm{s}\ . && \text{(5.8d)}
\end{aligned}$$

The determined uncertainty of $\sigma_{\Delta t_{\mathrm{coinc}}} = 0.656\,\mu\mathrm{s}$ reflects the jitter in time of the GPS clock as well as the variation of the processing time of KASCADE-Grande.

The correlated timestamps reject falsely triggered events due to RFI on the trigger cable or random trigger signals during technical problems of KASCADE-Grande and those events which cannot be reconstructed (typically $\approx 9\,\%$ of the data).

training data The correlation of the self-triggered training data with the reconstructed data of KASCADE-Grande results in 57 accepted shower candidates from all the arrival directions and 52 shower candidates for $\theta < 60°$.

verification data 285 events for antenna cluster D17 and 779 events for D30 remain respectively after correlation with KASCADE-Grande and appliance of the $\theta < 60°$ cut. The time period of the verification data D30 is twice the time of the verification data D17. Thus the resulting amount of events differ by a factor of about 2.

5.5.2 Purity, Efficiency and Rejection

Direction Correlation

The correlated events are coincident and contain background and shower events. The arrival direction of the radio event and the direction delivered from KASCADE-Grande have to correspond within their uncertainties to identify shower events correctly, whereas background signals fulfil these constraints only by chance.

The direction correlation is performed by using the cuts described in eq. 5.9 with LOPES$^{\mathrm{STAR}}$ zenith angle θ_{STAR} and azimuth angle φ_{STAR} as well as the KASCADE-Grande zenith angle θ_{Grande} and azimuth angle $\varphi_{\mathrm{Grande}}$.

$$\theta_{\mathrm{STAR}} < 60^{\circ} \tag{5.9a}$$

$$\theta_{\mathrm{STAR}} - 2 \cdot \sigma_{\theta_{\mathrm{STAR}}} < \theta_{\mathrm{Grande}} < \theta_{\mathrm{STAR}} + 2 \cdot \sigma_{\theta_{\mathrm{STAR}}} \tag{5.9b}$$

$$\varphi_{\mathrm{STAR}} - 2 \cdot \sigma_{\varphi_{\mathrm{STAR}}} < \varphi_{\mathrm{Grande}} < \varphi_{\mathrm{STAR}} + 2 \cdot \sigma_{\varphi_{\mathrm{STAR}}} \tag{5.9c}$$

Purity

After correlation of the self-triggered events with the recorded timestamps of KASCADE-Grande the applied direction cuts (eq. 5.9) result in well-correlated extensive air showers (same timestamp and same arrival direction). The purity describes the ratio of accepted shower events to the total number of accepted events of the self-trigger. The total number of events can be estimated on the basis of the analysis results from KASCADE-Grande by taking into account the shower geometry and the geomagnetic angle, respectively.

training data 7 shower events out of 52 events remain after correlation of the timestamp and direction with the ones of KASCADE-Grande including $\theta < 60^{\circ}$. This corresponds to a purity of 14 % for the training data.

verification data 285 events and 779 events are accepted by antenna cluster D17 and D30 by the self-trigger including a cut on the zenith angle ($\theta < 60^{\circ}$), respectively. After correlation (timestamp and direction) 22 events (D17) and 34 events (D30) are identified as radio emission of cosmic rays. The purity results in 7 % (D17) and 5 % (D30) for the verification data.

The differences of the obtained purity reflect the influence of the individual background sources depending on the site of the antenna cluster. Emitted signals from uncorrelated or correlated background sources reach the detector horizontally from random azimuth directions. The channel trigger accepts shower-like background signals and the coincidence trigger accepts these signals by chance. The reconstructed arrival direction points to a random azimuth and zenith angle. In fact, this is the main reason for the low purity results and the falsely accepted background events. A detection site without the industrial environment (e.g. Pierre Auger Observatory) and advanced trigger levels will increase the purity.

Efficiency

A reliable efficiency analysis has to be based on detailed MC simulations for a full detector simulation as well as MC simulations for the radio emission of high energy cosmic rays.

data set name	cluster no.	accepted events	applied constraints
training data	D30	102,535	none (all the events)
		20,547	quality cuts per channel
		560	channel trigger
		68	+ coincidence trigger
		57	+ $\theta_{\mathrm{STAR}} < 60°$
		52	+ Grande: time correlated
		7	+ Grande: θ & φ correlated
verification data D17	D17	787,203	none (all the events)
		2,209	channel trigger
		1,226	+ coincidence trigger
		499	+ $\theta_{\mathrm{STAR}} < 60°$
		285	+ Grande: time correlated
		22	+ Grande: θ & φ correlated
verification data D30	D30	1,598,543	none (all the events)
		33,452	channel trigger
		1,676	+ coincidence trigger
		1,260	+ $\theta_{\mathrm{STAR}} < 60°$
		779	+ Grande: time correlated
		34	+ Grande: θ & φ correlated

Table 5.2: Summary of the accepted events in relation to the applied trigger constraints of the data sets used. The deviation of the rejection rates between the different data sets are due to the environmental effects and seasonal influences on each antenna cluster. None of the shower events are rejected by the applied constraints.

The shower simulation methods are available, but a sufficient detector simulation is not ready. In addition, the sensitive area of the detector array has to be determined by simulations as well. It is very complex to extract the sensitive area only based on the measured events due to the low particle flux at these high energies. Furthermore, the effect of the radio emission and its dependence on the geomagnetic angle have to be measured and simulated in detail to get reliable efficiencies.

The efficiency describes the ratio of the accepted shower events to the total number of shower events in the data set. The KASCADE-Grande reconstruction was used to determine the absolute number of observed shower events in each data set. Therefore, quality cuts were applied to the results of the reconstruction of KASCADE-Grande (Grande cuts). Only shower events that fulfil the quality constraints are used in the following. A detailed discussion of Grande cuts are presented in section 6.2.1.

The chosen Grande cuts are applied to the KASCADE-Grande data and result in 25 shower events (training data) which are detected in the particle detectors. 4 out of 25 shower events are accepted by the self-trigger on the basis of the radio emission and this corresponds to an efficiency of 16 % ($5 \cdot 10^{17}\,\mathrm{eV} < E < 10^{18}\,\mathrm{eV}$).

The 21 rejected shower events by LOPES$^{\mathrm{STAR}}$ were analysed further to understand the rejection of the self-trigger system in more detail. It turned out that most of the shower events showed no radio signal in the time domain. This results from large RFI

background at this time or from the arrival direction of the extensive air shower. If this direction is almost in parallel to the geomagnetic field then no radio emission is emitted (geomagnetic angle $\alpha \approx 0°$). Only two rejected events showed pulse signals in more than 2 channels (different antennas), but the influence of the background at this time does not make it possible to detect these pulses. The efficiency results in more than 90 % by only taking into account shower events with a sufficient signal-to-noise ratio.

The results from the efficiency of the verification data are the same as for the training data. The background conditions on the site of the Forschungszentrum Karlsruhe are bad and time dependent as described above. The RFI and transient signals increase the dynamic threshold all the time and the acceptance of signals from radio emission with an energy $E \leq 5 \cdot 10^{17}\,\mathrm{eV}$ and a low geomagnetic angle is not efficient. In addition, the area covered by the KASCADE-Grande experiment ($700 \times 700\,\mathrm{m}^2$) limits the reconstruction of primary particles of $E > 10^{18}\,\mathrm{eV}$.

Rejection

The rejection r is defined as unity minus the ratio of the accepted events n to the total number of events m: $r = 1 - \frac{n}{m}$. The accepted events are defined in this context as the number of self-triggered events with no additional cuts.

training data The self-trigger accepted 68 out of 102,535 events, corresponding to a rejection of $r = 99.93\,\%$.

verification data The verification data of antenna cluster D17 consist of 787,203 events. After applying the self-trigger 1,226 events are accepted, corresponding to a rejection of $r = 99.79\,\%$. Antenna cluster D30 has 1,598,543 events in the verification data and 1,676 events are accepted from the self-trigger, corresponding to a rejection of $r = 99.92\,\%$.

The self-trigger method is not over-optimised on the training data due to the almost equal rejection value compared with verification data D30. The discrepancy of the rejection value of the verification data D17 and D30 reflects the different background conditions of the two antenna clusters on the site of the Forschungszentrum Karlsruhe.

5.5.3 Trigger Rates

The trigger rate of the first trigger level is important for the following data reduction in a multi-level trigger system.

Table 5.2 summarises the accepted number of events in relation to the different trigger constraints. The remaining events of the verification data D30 are about twice the number of accepted events of the verification data D17 due to the different observation times at the two antenna clusters. The deviation of the different rejections for the applied trigger cuts between the three data sets reflects the individual background situation on each antenna cluster.

Cluster Rate

There are two ways to calculate a mean trigger rate per antenna cluster on externally triggered data.

One is to analyse the complete time period of the verification data and to assume that the given trigger selects all the extensive air showers. Additionally, it is expected that the energy threshold of the external trigger is much lower than the detection threshold of the radio emission. Thus, most of the external triggers are random RFI and transient records. The recorded background events of almost 6 and 13 months, respectively, describe well the environmental influences on the antenna clusters D17 and D30. Applying the self-trigger conditions to this data corresponds to work a continuous data flow. In this case the mean trigger rate results in $\bar{f}_{\mathrm{D17,cont}} \approx 98\,\mu\mathrm{Hz}$ (D17) and $\bar{f}_{\mathrm{D30,cont}} \approx 78\,\mu\mathrm{Hz}$ (D30) for the verification data.

The other way to determine the mean trigger rate of the self-trigger is to combine the n externally triggered time windows $\Delta t = 25.6\,\mu\mathrm{s}$ with a virtual observation time $t_{\mathrm{virt}} = n \cdot \Delta t$. After applying the self-trigger to the combined verification data the trigger rate results in $\bar{f}_{\mathrm{D17,virt}} \approx 60\,\mathrm{Hz}$ (D17) and $\bar{f}_{\mathrm{D30,virt}} \approx 40\,\mathrm{Hz}$ (D30), whereas the rates are defined by the ratio of accepted events to t_{virt}.

The real trigger rates per cluster will lie in between these two results and have to be measured on the field. In addition, the geometrical effects of the external trigger cluster 13 from KASCADE-Grande are not taken into account.

Channel Rate

The channel trigger rate can be directly considered as the external trigger rate of KASCADE-Grande $\bar{f}_{\mathrm{channel,cont}} = \bar{f}_{\mathrm{cluster\ 13}} \approx 50\,\mathrm{mHz}$.

In case of the virtual observation time the trigger rate per channel results in $\bar{f}_{\mathrm{channel,virt}} \approx 7.3\,\mathrm{kHz}$. The channel trigger rate reflects the background conditions and can easily be decreased on the sites with lower background, e.g. the Pierre Auger Observatory.

A random coincidence trigger rate of three uncorrelated trigger sources (trigger cell per antenna cluster) is given by eq. 5.10.

$$
\begin{aligned}
f_{\mathrm{coinc,random}} =& f_{\mathrm{channel}}^3 \cdot t_{\mathrm{coinc}}^2(\theta) && \text{(5.10a)}\\
=& \left(7.3\,\mathrm{kHz}\right)^3 \cdot \left(215\,\mathrm{ns}\right)^2 && \text{(5.10b)}\\
\approx& 18\,\mathrm{mHz} && \text{(5.10c)}
\end{aligned}
$$

where t_{coinc} is given by eq. 5.7 with a baseline $b_{\mathrm{D30}} = 65\,\mathrm{m}$ and a zenith angle $\theta = 60°$. The randomly triggered events from all the directions are negligible compared to the cluster trigger rates.

Equation 5.10 is only valid for uncorrelated trigger sources, e.g. independent machines, which emit several signals in a time window less than t_{coinc}. If these signals are accepted by the channel trigger (transient cuts) then the coincidence trigger is additionally fulfilled. But a reconstruction of the arrival direction results in an inclined direction and the triggered event is identified as background and is rejected.

5.5.4 Threshold Characteristics

The behaviour of the dynamic threshold (see eq. 5.3) for each channel describes the characteristics of the self-trigger. It is sensitive to the background influence and defines the energy threshold for radio detection of extensive air showers.

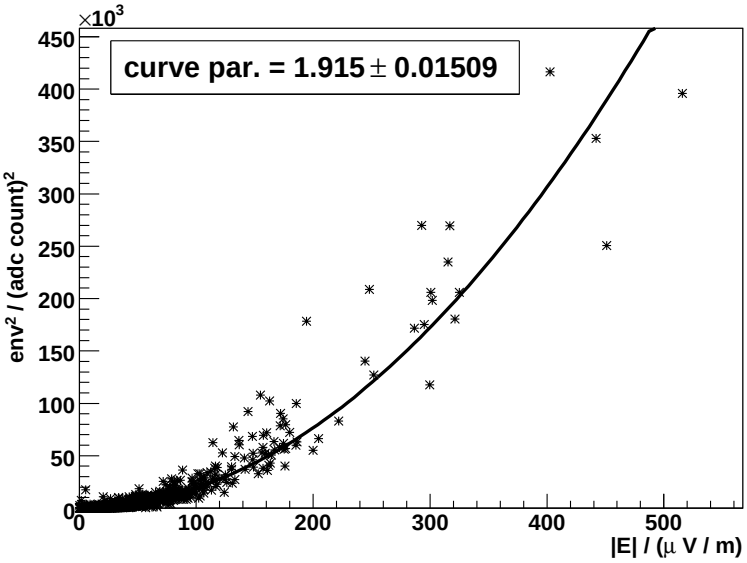

Figure 5.11: Calibration curve to convert the threshold of the channel trigger in units of ADC counts into an electric field strength. The solid black line corresponds to a parabolic fit ($y = \text{curve} \cdot x^2$).

Conversion

The dynamic threshold is calculated and compared with the squared envelope signal after RFI suppression. A conversion factor for the threshold in the unit of squared ADC count into the unit of field strength is necessary for quantitative conclusions. The distribution of the threshold calibration is shown in figure 5.11 where the squared envelope samples versus the absolutely calibrated samples are given. A parabolic connection between the squared envelope signal and the time samples is expected due to the squaring of the envelope. A parabolic fit function (see eq. 5.11) is applied to the data and illustrated as the solid black line in fig. 5.11 as well.

$$\text{env}^2 = \text{curve} \cdot |\text{E}|^2 \tag{5.11a}$$

$$\text{curve} = (1.915 \pm 0.015) \left(\frac{\text{ADC}}{\frac{\mu\text{V}}{\text{m}}} \right)^2 \tag{5.11b}$$

The deviation of the curve parameter from 2 results from the manipulation of the amplitude spectrum and the applied window function during Fourier transform (calibration processes).

The curve parameter resulting from the fit (eq. 5.11) is obviously dependent on the bandwidth of LOPES$^{\text{STAR}}$. The effective bandwidth $\Delta f_{\text{eff}} = 42.02\,\text{MHz}$ has to be taken into account to normalise the dynamic threshold and to compare the dynamic threshold with other experiments.

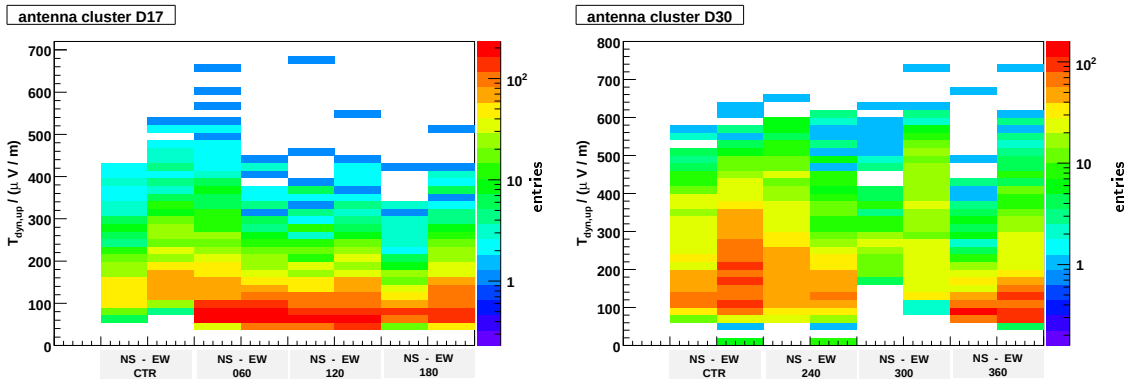

Figure 5.12: The distribution of the calibrated dynamic threshold versus the observed channels in antenna cluster D17 (left fig.) and D30 (right fig.).

Distribution of Dynamic Thresholds

The distribution of the calibrated dynamic threshold is illustrated for all the channels in fig. 5.12 for antenna cluster D17 (left hand fig.) and D30 (right hand fig.). Each entry corresponds to a positive channel trigger condition of the verification data. The threshold calibration was performed by using eq. 5.11 without normalisation.

Antenna Cluster D17 The distribution of the left hand fig. 5.12 shows that most of the calculated thresholds result in $T_{\mathrm{dyn,up,D17}} \approx 80\,\frac{\mu\mathrm{V}}{\mathrm{m}}$ due to the background influence. Antenna cluster D17 is located at the east edge of the Forschungszentrum Karlsruhe and at this position a lower background is expected (compare with right hand fig. (D30)).

The threshold behaviour for the CTR antenna differs from the rest due to less entries in this column. More transient signals have been detected and rejected in these channels by the channel trigger. In fact, the DAQ PC in antenna cluster D17 is located in the nearby KASCADE-Grande station 17 next to the CTR antenna. In the earlier days of LOPES$^{\mathrm{STAR}}$ this antenna cluster was the first experimental site with an old type of PC (DAQ computer) equipped with poor electromagnetic shielding.

Antenna Cluster D30 Antenna cluster D30 has a different distribution of the calibrated dynamic threshold (right hand fig. 5.12). The mean threshold results in $T_{\mathrm{dyn,up,D30}} \approx 100\,\frac{\mu\mathrm{V}}{\mathrm{m}}$, whereas the EW channels of CTR and 300 antenna show a spread to larger values. The cluster is located inside the area of the Forschungszentrum Karlsruhe.

The gap around $100\,\frac{\mu\mathrm{V}}{\mathrm{m}}$ for both polarisations of the antenna 300 is explained by the transient rejection of the channel trigger. This antenna is located next to a large computing centre, and next to an exhauster for the air conditioning of this centre giving rise to the dynamic threshold.

5.5.5 Conclusion and Outlook

Conclusion

The worst possible background conditions one can think of when developing a radio self-trigger system are given on the site of the Forschungszentrum Karlsruhe due to the industrial environment. The challenge to suppress enough background events and not to saturate the electronics is faced by the features of the self-trigger system discussed. The surrounding background signals could be identified and could be sufficiently suppressed by the self-trigger.

The plausibly motivated and optimised parameters reject RFI and transient signals on each channel per antenna to more than 99.9 %. The channel trigger methods are easy to extend for further parameters due to possible changes in background characteristics.

The accepted radio emission signals and shower like background signals in each channel are further analysed by the cluster trigger. It rejects highly inclined and coincident man-made signals ($\theta > 60°$) and all the non-coincident events as well. The cluster trigger also takes the rejected channels with multi-pulses (channel trigger) into account and searches the characteristic signal at the expected time positions. In fact, the chosen coincident constraint is optimised for the layout of the antenna array and has to be adapted for large-scale arrays.

The resulting purity (6 %), efficiency (90 %) and rejection (99.9 %) show that the self-trigger system rejects RFI and transient signals per channel and cluster in a sufficient way. The industrial environment on the site of the Forschungszentrum Karlsruhe complicates the trigger system and increases the rates, whereas on the site of the Pierre Auger Observatory purity and efficiency will increase due to the lower background of one order of magnitude (factor 100 in receiving power).

The calibration and normalisation of the dynamic threshold makes a comparison with different sites and experimental installations convenient and transparent. In addition, the threshold monitoring of each channel allows an easy cross-comparison with alternative self-trigger approaches.

The proof-of-principle of a working radio self-trigger system is obtained by the discussed investigations. The area covered by KASCADE-Grande limits the statistics of shower events to an energy of $E \leq 10^{18}$ eV. The energy range of the Pierre Auger Observatory as well as the much better background conditions make the site in Argentina attractive for the future of radio detection of extensive air showers.

A hardware design of the discussed method is necessary to achieve a fast and efficient self-trigger in a stand-alone application. An analogue electronic approach is too inflexible. Therefore, Field Programmable Gate Arrays (FPGAs) are selected for the hardware of the self-trigger. The presented self-trigger strategy can be transferred in a simple way to an FPGA algorithm.

Outlook

In the future large-scale arrays of radio detectors will be installed. It is necessary to equip each single antenna with a channel trigger including the RFI suppression and transient cuts. The information of the channel triggers are transmitted to the following coincidence trigger via wireless communication. The coincidence constraints are based on all the information of the channel triggers and the geometry of the array.

An existing hardware[3] with a digital signal processor (DSP) and FPGA is re-used to implement a prototype version of the discussed self-trigger methods. The optimised implementation of the trigger algorithms are in progress and first verification measurements are planned on the site of the Forschungszentrum Karlsruhe for autumn 2008. In a next step a measurement campaign on the site of the Pierre Auger Observatory with three LPDAs is planned for winter 2008. The FPGA based prototype self-trigger has to prove the experimental practicability under environmental conditions of the two sites.

[3]Developed at the Institute of Data Processing and Electronics, Forschungszentrum Karlsruhe.

Chapter 6

Data Analysis

6.1 Introduction

The radio signals measured with LOPES$^{\mathrm{STAR}}$ are absolutely calibrated and are recorded in coincidence with the KASCADE-Grande experiment. The chosen positions of the LOPES$^{\mathrm{STAR}}$ antennas per cluster strongly depend on the local environment and infrastructure of the Forschungszentrum Karlsruhe. The possibilities of LOPES$^{\mathrm{STAR}}$, in its prototype phase, are limited but provide a starting point for future radio detectors and point out the potential of the radio detection techniques.

This chapter presents the data selection of shower events that fulfil the applied quality constraints on the reconstructed data of both experiments, LOPES$^{\mathrm{STAR}}$ and KASCADE-Grande. Furthermore, the parametrisation of the field strength is described and compared with previous approaches. Finally, techniques to reconstruct air showers on an event-by-event basis are presented.

6.2 Data Selection

The applied data selection is based on the verification data (D17 & D30, see table 5.1). Additional quality cuts on KASCADE-Grande and LOPES$^{\mathrm{STAR}}$ are chosen to optimise the reconstruction discussed in the following.

6.2.1 Quality Cuts

KASCADE-Grande Cuts

The final KASCADE-Grande reconstruction results in more than 26 quantities describing geometry and properties of the individual air shower as well as the working condition of the experiment. Standard quality cuts, listed in table 6.1 (Grande cuts), to ensure a high quality and a well reconstruction of the air shower were chosen as used in the analysis of KASCADE-Grande.

The estimated energy of the primary particle follows the well-established parametrisation by the number of muons (N_μ), electrons (N_e), and the zenith angle (θ_{Grande}) as given in eq. 6.1a [Womm 07]. The expected uncertainty of this energy estimation is in the range of $\frac{\sigma_E}{E} \approx 40\,\%$. Background observations on the site of the Forschungszentrum

related to the working status of KASCADE-Grande

condition	explanation
$I_{active}\,\&\,1 = 1$	KASCADE-Array is active
Hit7 > 8	cluster 13 is active
$Flag_{ANKA} < 4$	status of the nearby synchrotron source ANKA to reject background induced events
Quality Flag > 0	internal quality flag is fulfilled
$N_{Grande\ stations} > 0$	number of involved active stations

related to the reconstruction of KASCADE-Grande

condition	explanation
$N_\mu > 11111$	total number of muons is successfully reconstructed
$N_e > 11111$	total number of electrons is successfully reconstructed
$\theta_{Grande} < 45°$	standard reconstruction is uncertain (for $\theta > 45°$)
$-600\,\mathrm{m} < x_{Grande} < 100\,\mathrm{m}$	position of the shower core lies in the field of KASCADE-Grande (x coordinate)
$-600\,\mathrm{m} < y_{Grande} < 100\,\mathrm{m}$	same for the y coordinate
$1.4 > Age_{Grande} > 0.4$	cut on the shower age, which results from the fit to the lateral distribution of the electrons (NKG fit, see chapter 2), empiric parameter range

Table 6.1: Overview of the Grande cuts to obtain well reconstructed shower events from KASCADE-Grande. The conditions of the working status guarantee that the KASCADE-Grande experiment is in a proper working mode. In addition, the reconstruction was successful and results in well reconstructed shower parameters if the remaining conditions are fulfilled.

Karlsruhe point out that a sufficient signal-to-noise ratio for the discussed self-trigger is expected from cosmic ray events with $E > 10^{17.5}\,\mathrm{eV}$ (energy cut, see eq. 6.1b).

$$\begin{aligned}\log_{10}(E) =& 0.319 \cdot \log_{10}(N_e) + 0.709 \cdot \log_{10}(N_\mu) \\ &+ \frac{1.236}{\cos(\theta_{Grande})} + 0.238 \ \ [\log_{10}(\mathrm{GeV})] \qquad (6.1a)\\ E >& 10^{8.5}\,\mathrm{GeV} = 10^{17.5}\,\mathrm{eV} \qquad (6.1b)\end{aligned}$$

LOPES^{STAR} Cuts

The events accepted by the self-trigger conditions are correlated by timestamp and arrival direction with the events accepted by the Grande cuts. The defined conditions of the self-trigger and the correlation (timestamp and arrival direction) ensure that only well reconstructed shower events are finally accepted.

verification data		
D17	D30	applied cuts
22	34	self-trigger + Grande: time & direction correlation
6	14	+ Grande cuts
3	7	+ $E > 10^{17.5}$ eV

Table 6.2: Accepted number of events after applying the described cuts. The resulting 10 radio events correspond to 9 shower events, reconstructed by KASCADE-Grande. One individual shower event was separately detected in antenna cluster D17 & D30.

6.2.2 Event Statistics

The amount of events accepted after application of the quality cuts are listed in table 6.2. The first row shows the accepted events after applying the self-trigger as well as the correlation of the data by timestamp and arrival direction. In the following rows the accepted events of the KASCADE-Grande quality cuts (Grande cuts) as well as the energy cut ($E > 10^{17.5}$ eV) are given.

The remaining 10 radio events with their reconstructed quantities yield a good reconstruction and are related to 9 extensive air showers, reconstructed by KASCADE-Grande. One of the radio events was observed in both antenna cluster D17 & D30 and, therefore, counted twice. An additional shower event was detected by all 10 LOPES$^{\mathrm{STAR}}$ antennas, but rejected by the Grande cuts due to the inclined arrival direction. Nevertheless, this shower event is used later for a comparison with MC simulations.

The number of events is limited by the size of the instrumented area and the short observation time as well as the low particle flux at these high energies (5 events/month are expected according to the cosmic ray flux and the effective area of the clusters). The discussed analysis is limited by the event statistics, but it demonstrates the potential and advantages of the radio detection technique.
Note: The radio data of antenna cluster D19 are recorded for all the external trigger signals from KASCADE-Grande during the period in which the verification data were taken.

6.2.3 Distribution of the Shower Cores

The impact point or position of the shower core on the ground in the reference frame of KASCADE-Grande is shown in fig. 6.1 (positions derived from KASCADE-Grande). The open symbols (D17: □, D30: ○) mark the positions of the accepted events from the self-trigger including the correlation (timestamp and arrival direction) with KASCADE-Grande, whereas the other symbols (D17: +, D19: •, D30: ×) mark the core positions of the remaining events after the Grande cuts. The illustrated positions of the shower core are spread homogeneously over the equipped area and, as expected, are slightly shifted towards the external trigger (cluster 13) of KASCADE-Grande.

A radio signal of a cosmic ray air shower is detected in all the antennas, the so-called golden event, if all the introduced symbols match at one position. Due to the limited observation time such golden events are only detected twice and marked with the red dashed circle (I and II in fig. 6.1). The red dashed circle (II) on the left hand side marks

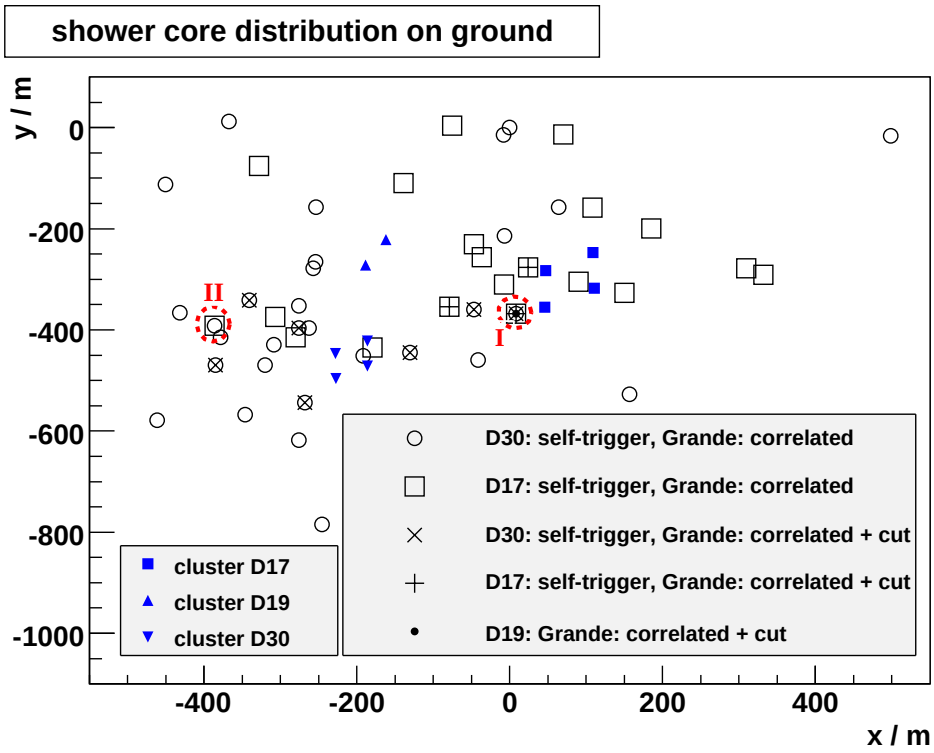

Figure 6.1: Distribution of the shower cores for different quality cuts and separated by the LOPES$^{\mathrm{STAR}}$ antenna clusters. The coordinates of each shower core are reconstructed by KASCADE-Grande. Two events are recorded from all 10 LOPES$^{\mathrm{STAR}}$ antennas and are marked with a red circle (I & II) — golden events.

a position of a shower core which was detected by the self-trigger in all 10 LOPES$^{\mathrm{STAR}}$ antennas but rejected by a quality cut on the zenith angle (Grande cuts).
Note: Position II is not marked with • due to the Grande cuts, but the raw data of antenna cluster D19 are recorded anyhow.

6.3 Parametrisation of the Field Strength

A parametrisation of the observed radio pulse allows a systematic comparison with other experiments. The determined parameters in combination with the reconstructed geometry of the air shower allow an estimation of the primary energy. Therefore, all the radio events accepted by the applied quality cuts are used to parametrise the field strength by taking into account different effects of the shower geometry and the energy of the primary particle. The peak value of the detected pulse in each polarisation ($|\vec{E}_{\mathrm{EW}}|$ and $|\vec{E}_{\mathrm{NS}}|$) is combined by vectorial addition $|\vec{E}| = |\sqrt{|\vec{E}_{\mathrm{NS}}|^2 + |\vec{E}_{\mathrm{EW}}|^2}|$ and divided by the effective bandwidth $\Delta f_{\mathrm{eff}} = 42.02\,\mathrm{MHz}$. The resulting quantity ϵ in $\left[\frac{\mu\mathrm{V}}{\mathrm{m}\cdot\mathrm{MHz}}\right]$, ϵ_{NS} and ϵ_{EW}, respectively, is correlated to the observed radio pulse and is used in the present analysis.

6.3.1 First Approaches

The investigated approaches in previous experiments to parametrise the measured field strength [Alla 71, Hueg 05b, Horn 06, Nehl 08a] have several characteristics of the primary particle in common:

energy E The observed field strength scales linearly with the energy E of the primary particle due to coherent radio emission.

geomagnetic angle α The angle between the shower axis and the geomagnetic field is named geomagnetic angle and is a function of the arrival direction $\alpha(\theta, \varphi)$. In the model of the geosynchrotron emission $\sin(\alpha)$ characterises the strength of the Lorentz force $\vec{F}_L = e\vec{v} \times \vec{B}$ due to the cross product, where $|\vec{v}| \approx c$ is the speed of light and $\vec{B}$ is the strength of the magnetic field of the Earth.

scale parameter d_0 The field strength decreases rapidly with increasing distance perpendicularly to the shower axis (reference frame of the shower). The cited measurements and simulations showed that an exponential function with a scale parameter d_0 parametrises this behaviour well. d_0 and its dependency on the energy, if any, is an important quantity to define the spacing of future detectors to observe radio emission. The lateral spread parameter R of the radio emission in the coordinate system on the observation level is related to d_0 by the zenith angle of the primary particle: $R = \frac{d_0}{\cos(\theta)}$.

zenith angle θ The main dependence on the zenith angle is given by the geomagnetic angle α. The arrival direction of the shower (θ and φ) and the direction of the magentic field lines have to be known in order to determine α. In addition, the zenith angle determines the footprint of the shower on the observation level.

The previous parametrisations used a $\cos(\theta)$ dependence on the zenith angle. The emitted radio signal is polarised in a plane perpendicularly to the Poynting vector. And the measured field strength corresponds to a projection of the electric field onto the sensitive antenna plane. LOPES$^{\mathrm{STAR}}$ measures the projection of the north-south & east-west polarisation due to the arrival direction (azimuth angle), but the vertical component is suppressed by the antenna. The missing vertical component may be included by taking into account the direction sensitivity of the antenna used (calibration). Thus, a $\cos(\theta)$ parametrisation may be not necessary.

Furthermore, the attenuation length of an electromagnetic wave in the atmosphere ($1\,\mathrm{MHz} < f < 100\,\mathrm{MHz}$) is much higher than the mean free path of the particles in an extensive air shower. This is the advantage of the radio detection technique to record radio emission on the ground, whereas the electromagnetic component of the shower has died out [Petr 07].

6.3.2 Recent Approaches

One of the advantages of LOPES$^{\mathrm{STAR}}$ is the observation of the north-south & east-west component of the polarisation at one position at the same time. The dual-polarised measurements are used for the parametrisation of the total field strength and additionally

allow to verify the parametrisations of previous studies as given in eq. 2.2 and eq. 2.3, respectively [Alla 71, Horn 06].

A general parametrisation follows eq. 6.2 and takes into account the previous approaches (only ϵ_{EW}) and is the starting equation to parametrise the total field strength ϵ. The function has to be adapted to the data to find the best solution.

$$\begin{aligned}\epsilon_{\text{tot or EW}} = C \cdot \cos(\theta) \cdot (C_\alpha \pm \sin(\alpha \pm \phi_\alpha)) \\ \cdot \exp\left(-\frac{d_{\mathrm{axis}}}{d_0}\right) \cdot \left(\frac{E}{\mathrm{GeV}}\right)^{C_E} \left[\frac{\mu\mathrm{V}}{\mathrm{m}\cdot\mathrm{MHz}}\right]\end{aligned} \tag{6.2}$$

Where ϵ_{tot} and ϵ_{EW} are the parameters correlated to the measured radio peak of the combined channels and only the east-west component, respectively, C is a proportional constant, θ is the zenith angle, $(C_\alpha \pm \sin(\alpha \pm \phi_\alpha))$ describes the dependence on the geomagnetic angle α with an additional phase ϕ_α, an exponential function corresponds to the lateral decrease including the scale parameter d_0, and a power law with an exponent C_E, which has to be close to unity (coherent signal), describes the dependence on the energy of the primary particle.

The Method

An iterative procedure to determine the parameters and their uncertainties was performed by using the minuit package of root [Brun 97] (TMinuit, v5.18.00) with the internal MIGRAD algorithm. The χ^2 function follows eq. 6.3, in which the index data corresponds to the measured and calibrated data, whereas the index par corresponds to the chosen parametrisation (eq. 6.2). The difference between the data and the model was then minimised by the minuit algorithm to find the best parameters describing the measured data.

$$\chi^2 = \left(\frac{\epsilon_{\mathrm{data}} - \epsilon_{\mathrm{par}}}{\sigma_{\epsilon_{\mathrm{data}}}}\right)^2 \tag{6.3}$$

The uncertainties of the measured signals per polarisation were estimated by taking into account the noise level in each channel. Therefore, the mean noise level $|\vec{E}_{\mathrm{noise,pol}}|$ and its uncertainty $|\bar{\vec{\sigma}}_{E_{\mathrm{noise,pol}}}|$ in the recorded time window excluding the detected shower pulse per channel (polarisation) were determined based on the envelope signal. The influences of background processes and the noise level are estimated at $\sigma_{\mathrm{noise,pol}} = |\vec{E}_{\mathrm{noise,pol}}| + 5 \cdot |\bar{\vec{\sigma}}_{\vec{E}_{\mathrm{noise,pol}}}|$. In addition, the uncertainty of the calibration has to be taken into account and results in 7.4 % related to the peak value.

The totally estimated uncertainty of the data per channel results in $\sigma^2 = \sigma^2_{\mathrm{noise,pol}} + \sigma^2_{\mathrm{calib,pol}}$ and additionally has to be divided by the effective bandwidth Δf_{eff}.

Both polarisations per LPDA are combined per vectorial addition $\epsilon = \frac{|\sqrt{|\vec{E}_{\mathrm{NS}}|^2 + |\vec{E}_{\mathrm{EW}}|^2}|}{\Delta f_{\mathrm{eff}}}$ and the uncertainties are calculated by Gaussian error propagation.

6.3.3 Signals of the East-West Polarised Component

A comparison with the previous experiments is performed on the basis of the east-west polarised component measured by LOPES$^{\mathrm{STAR}}$. This study is separated into one part

that takes the zenith dependency into account (as well as the previous approaches) and another part that neglects it.

With $\cos(\theta)$ dependence:

The best parametrisation and its resulting parameters as well as its uncertainties are given in eq. 6.4 for the comparison with the previous approaches. The final $\chi^2 \approx 37$ corresponds to a probability of about 18 % by taking into account the number of degree of freedom ndf = 30.

$$\begin{aligned}\epsilon_{\mathrm{EW}} = &(0.5 \pm 0.3) \cdot \cos(\theta) \cdot ((7.1 \pm 3.6) - \sin(\alpha)) \\ &\cdot \exp\left(-\frac{d_{\mathrm{axis}}}{(122 \pm 12)\,\mathrm{m}}\right) \cdot \left(\frac{E}{\mathrm{GeV}}\right)^{1.24\pm0.01} \left[\frac{\mu\mathrm{V}}{\mathrm{m}\cdot\mathrm{MHz}}\right]\end{aligned} \tag{6.4}$$

The constant factor of (0.5 ± 0.3) with its uncertainty of 60 % shows that the measured signal might be overestimated. The geomagnetic angle is described by $((7.1 \pm 3.6) - \sin(\alpha))$. A parametrisation, like for the LOPES30 data [Horn 06, Nehl 08a], that depends on $(1-\cos(\alpha))$ is not consistent with the given statistics. Higher event statistics are needed to verify the previous parametrisations.

Without $\cos(\theta)$ dependence:

The best parametrisation without the θ dependence is given in eq. 6.5. The final $\chi^2 \approx 37$ corresponds to a probability of about 20 % by taking into account the number of degree of freedom ndf = 31.

$$\begin{aligned}\epsilon_{\mathrm{EW}} = &(2.2 \pm 0.3) \cdot (1 + \cos(\alpha)) \\ &\cdot \exp\left(-\frac{d_{\mathrm{axis}}}{(120 \pm 12)\,\mathrm{m}}\right) \cdot \left(\frac{E}{\mathrm{GeV}}\right)^{1.15\pm0.04} \left[\frac{\mu\mathrm{V}}{\mathrm{m}\cdot\mathrm{MHz}}\right]\end{aligned} \tag{6.5}$$

Assuming no $\cos(\theta)$ dependence on the zenith angle and choosing a fixed α dependence result in the same χ^2 value and an increased probability. The chosen model describes the data better due to the smaller uncertainties of the parameters. Any parametrisation with more parameters did not improve the probability of the fit. Again, a higher shower statistics is needed to optimise the parametrisation of the measured radio pulses.

Results

The best found parametrisations are presented for the east-west polarised component of the electric field. None of the previous parametrisations are consistent with the given statistics. The main reasons for that is the low event statistics. The large uncertainties in the calibration of the previous experiments might be an additional effect. The ongoing measurements in coincidence with KASCADE-Grande will allow more detailed investigations with much higher event statistics.

The best parametrisation of the LOPES$^{\mathrm{STAR}}$ data shows no dependence on the zenith angle θ and parametrises the geomagnetic angle by $(1 + \cos(\alpha))$. The scale parameter d_0 results in $d_{0,\mathrm{EW}} = (121 \pm 12)\,\mathrm{m}$ for the parametrisation of the east-west polarised signals.

6.3.4 Signals of the North-South & East-West Polarised Component

The quantity ϵ is related to the radio pulse and used to parametrise the measured signals. For the first time dual-polarised measurements can be parametrised with the help of the reconstruction from a well calibrated extensive air shower experiment. The first parametrisation takes into account a dependence on $\cos(\theta)$, whereas the second approach neglects it.

With $\cos(\theta)$ dependence:

The best parametrisation and its resulting parameters as well as its uncertainties are given in eq. 6.6. The final $\chi^2 \approx 28$ corresponds to a probability of about 14 % by taking into account the number of degree of freedom ndf = 21.

$$\begin{aligned}\epsilon = &(9.1 \pm 5.5) \cdot \cos(\theta) \cdot ((1.1 \pm 0.05) - \sin(\alpha + (0.43 \pm 0.15))) \\ &\cdot \exp\left(-\frac{d_{\text{axis}}}{(137 \pm 16)\,\text{m}}\right) \cdot \left(\frac{E}{\text{GeV}}\right)^{1.71 \pm 0.02} \left[\frac{\mu\text{V}}{\text{m} \cdot \text{MHz}}\right]\end{aligned} \tag{6.6}$$

The constant factor (9.1 ± 5.5) with an uncertainty of 60 % and the deviation from unity of the exponent (1.71 ± 0.02) of the energy behaviour reflect the low event statistics and the energy uncertainty of the primary particles $\frac{\sigma_E}{E} \approx 40\,\%$. The parametrisation of the geomagnetic angle shows a sinus dependence due to the small phase (0.43 ± 0.15) rad. Again, the event statistics is too low to obtain significant results.

Without $\cos(\theta)$ dependence:

The best parametrisation and its resulting parameters without the θ dependence is given in eq. 6.7. The final $\chi^2 \approx 27$ corresponds to a probability of about 14 % by taking into account the number of degree of freedom ndf = 22 due to one more fixed parameter compared to eq. 6.6.

$$\begin{aligned}\epsilon = &(4.4 \pm 1.3) \cdot ((1.08 \pm 0.07) - \sin(\alpha)) \\ &\cdot \exp\left(-\frac{d_{\text{axis}}}{(138 \pm 20)\,\text{m}}\right) \cdot \left(\frac{E}{\text{GeV}}\right)^{1.6 \pm 0.3} \left[\frac{\mu\text{V}}{\text{m} \cdot \text{MHz}}\right]\end{aligned} \tag{6.7}$$

Small uncertainties of the parameters are obtained by this approach. The resulting uncertainty of the energy behaviour (1.6 ± 0.3) (18 %) is again related to the energy uncertainty of KASCADE-Grande. Higher event statistics has to verify eq. 6.7.

The parametrisation of eq. 6.7 describes best the observed radio emission of extensive air showers with LOPES$^{\text{STAR}}$.

6.3.5 Results

The correlations of the dual-polarised measurements of LOPES$^{\text{STAR}}$ with the well calibrated results from KASCADE-Grande are limited due to the low event statistics. The parametrisation of the measured radio pulses is an important step to understand radio emission in detail.

The dependence of the geomagnetic angle α might be described by $(1 - \sin(\alpha))$. Both approaches, eq. 6.6 and 6.7, result in low uncertainties of 5 % and 6 %, respectively. The scale parameter d_0 results in $d_0 = (137 \pm 18)$ m.

The event statistics does not allow to verify previous parametrisations of the radio emission based on signals of the east-west polarised components of the radio pulses.

LOPES$^{\mathrm{STAR}}$ has to be seen as a prototype detector for large-scale arrays. Thus, this analysis points out the possibilities of the detector system and helps to design future detectors. The limiting factor of the presented parametrisation of the field strength is the low event statistics due to the small area equipped on the site of the Forschungszentrum Karlsruhe and the limited time of measurement.

6.4 Shower Reconstruction

The reconstruction of shower quantities based on the recorded LOPES$^{\mathrm{STAR}}$ data are performed on an event-by-event basis. The first part of this section discusses the reconstruction of the arrival direction of the primary particles and an estimation of the angular resolution of LOPES$^{\mathrm{STAR}}$ is presented. Furthermore, the distributions of the shower quantities are shown and compared with the expectations of the geosynchrotron model. The last part of this section is dedicated to the golden events and the comparison with detailed Monte Carlo simulations for these events.

The digital methods used in this section (RFI suppression, up-sampling, and envelope calculation) are described in detail in sec. 3.4.

6.4.1 Direction Reconstruction

Several methods to reconstruct the arrival direction on the basis of radio data are possible.

Beam-forming is a common method of radio astronomy and is also available in the analysis framework of LOPES30 [Baeh 08, Rohl 04]. Beam-forming takes advantage of interference to change the directionality of the antenna array by shifting the individual time data per channel by a estimated time constant Δt_{bf} to maximise the coherence. An assumption of the expected shower front has to be made and the pointing accuracy increases with increasing number of antennas used. The method allows to use low signal-to-noise data which show no significant signal in the time domain. Furthermore, the time base of all the time samples used have to be known very precisely in order to achieve an accurate angular resolution (this is valid for any reconstruction method of the arrival direction).

The three LOPES$^{\mathrm{STAR}}$ antenna clusters record their own GPS timestamp and the systems are synchronised not better than 100 ns (accuracy is given by the manufacturer), but within a cluster the accuracy is better than 5 ns. Thus, beam-forming over all the clusters reach an angular resolution not better than the reconstruction of KASCADE-Grande of $\Delta\theta \approx \Delta\varphi \approx 2^{\circ}$.

Each LOPES$^{\mathrm{STAR}}$ cluster digitises the time samples in phase with the same 80 MHz clock. In addition, all the cables have the same length and all the electronic components are identical in construction. Thus, the delay of the received signal, caused by the hardware, corresponds to a constant delay and is identical for all the channels in all the

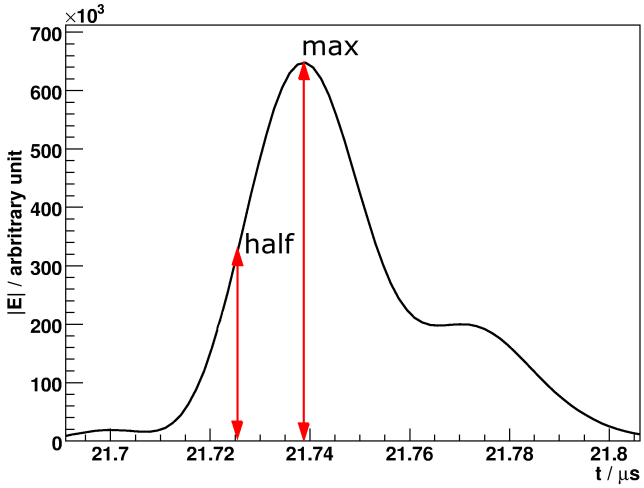

Figure 6.2: Two constraints to define the time position of the pulse: Rising edge at half the height (half) or at full height (max).

antenna clusters. An identical and constant offset in the time data has no effect on the reconstruction of the arrival direction.

The approximation of a plane shower front is used as simplification for the reconstruction of the direction. Monte Carlo (MC) simulations and other analyses pointed out a spherical shower front with a radius of several kilometres [Hueg 05b, Nigl 08]. However, the assumption is a good approximation due to the short baseline b in the clusters $b_{\mathrm{D17}} = 70\,\mathrm{m}$ and $b_{\mathrm{D30}} = 65\,\mathrm{m}$. In fact, the assumption of a plane shower front is only valid for the reconstruction of the arrival direction based on the data of a single antenna cluster as performed in this analysis. A reconstruction of a spherical shower front with only four points on the ground is not satisfying. The simplification of the arrival direction due to a plane shower front might also be seen as a starting point for further and more complex algorithms (e.g. with a larger antenna array).

The reconstruction of the direction with LOPES$^{\mathrm{STAR}}$ is based on the `SdPlaneFit` module of the Pierre Auger Observatory analysis framework – Offline [Roth 05]. The analytical formulae are adapted to the coordinate grid and the angle definition of the reference frame of KASCADE-Grande. The timing accuracy of the position of the pulse is chosen to be 12.5 ns with respect to the approximation of the plane shower front and the parametrisation of the RF signal.

Position in Time of the Radio Pulse

The definition of the position in time of the detected pulse has to be robust against background influences and different shower geometries. The rising edge of the envelope provides such conditions. The filter response function and especially the rising edge are mainly dominated by the characteristics of the band-pass filter (short rise time).

The envelope signal is calculated and the position in time of the radio pulse is defined by a constant fraction method (factor $f = 0.5$) of the rising edge. Various factors

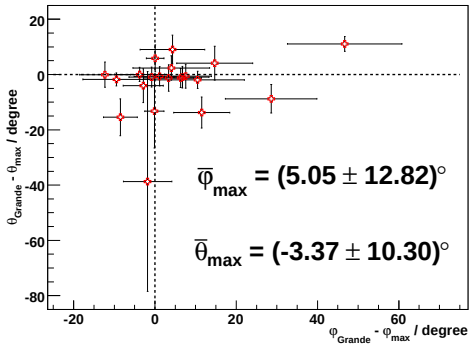

Figure 6.3: Difference of the reconstructed arrival directions (φ and θ) of KASCADE-Grande and LOPES$^{\mathrm{STAR}}$ and their uncertainties (max method).

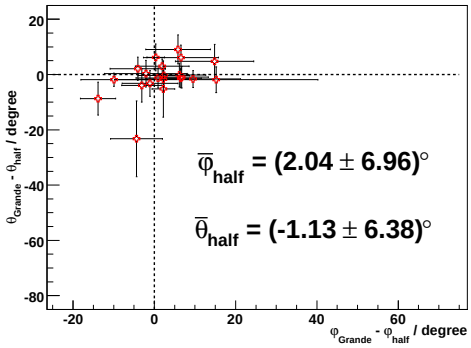

Figure 6.4: Difference of the reconstructed arrival directions of KASCADE-Grande and LOPES$^{\mathrm{STAR}}$ for the half method.

$0 < f \leq 1$ were analysed to find an optimal and robust constant fraction factor f. In fig. 6.2 is shown the iteratively derived factor $f = 0.5$ (half) and — for comparison — the maximum (max) $f = 1$ (typical choice).
Note: Only radio pulses detected by the self-trigger (snr > 75) are used for the reconstruction of the arrival direction.

Angular Resolution

The angular resolution of the LOPES$^{\mathrm{STAR}}$ antenna clusters (D17 & D30) are based on a well reconstructed data selection. The arrival direction of the radio events was reconstructed twice, once with the max method and once with the half method (see fig. 6.2).

The resulting arrival direction of each method was then subtracted from the one given by the reconstruction of KASCADE-Grande, due to the same arrival direction (within 0.5°) of the secondary particles and the radio emission [Nigl 08].

max method Fig. 6.3 shows the differences in arrival directions (zenith angle $\Delta\theta$ versus azimuth angle $\Delta\varphi$) reconstructed by KASCADE-Grande and LOPES$^{\mathrm{STAR}}$. The angular resolution results in $\Delta\bar{\varphi}_{\mathrm{max}} = (5.05 \pm 12.82)^\circ$ and $\Delta\bar{\theta}_{\mathrm{max}} = (-3.37 \pm 10.30)^\circ$ for the max method.

half method The more accurate half method reconstructs the arrival direction by taking the time position of the pulse at half its height into account. In fig. 6.4 the difference of $\Delta\theta$ versus $\Delta\varphi$ is illustrated. The angular resolution results in $\Delta\bar{\varphi}_{\mathrm{half}} = (2.04 \pm 6.96)^\circ$ and $\Delta\bar{\theta}_{\mathrm{half}} = (-1.13 \pm 6.38)^\circ$ for the half method.

The comparison between the max method and the half method points out that the angular resolution is more precise for the absolute reconstruction of direction by using the half method. Both methods have a systematic offset and an uncertainty in the order of the statistical error of the reconstructed direction. The offset and the uncertainty of

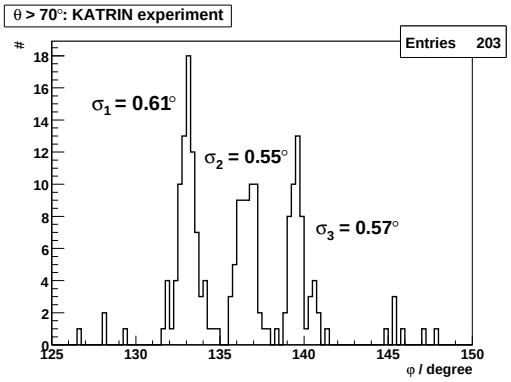

Figure 6.5: Antenna cluster D17 detects background events from the KATRIN experiment located in the south-east.

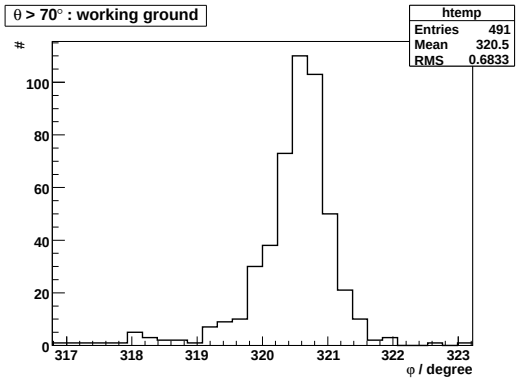

Figure 6.6: A well-known working ground in the north-west of antenna cluster D17 which shows a clear excess in the background distribution.

the half method is better by a factor of two than by the max method. In the following, the half method is used to reconstruct the arrival directions.

The systematic offset and its uncertainty are mainly dominated by the assumption of a plane shower front and the low number of antennas to calculate the arrival direction as the following section will show. In fact, the calculation of the incoming direction with triangulation is a fast and efficient way to start a more complex and more advanced reconstruction of the direction. In the case of using an antenna array with much more antennas then beam-forming should be the choice to achieve a high angular resolution [Nigl 08].

A further method to get a physical limit of the angular resolution is discussed in the following.

Physical Limit of the Angular Resolution

Sounding to horizontal background sources is possible for each antenna cluster. In this context the background sources are assumed to be locally fixed sources (e.g. industrial machines or working grounds) for the measurement period. The analysis is based on the externally triggered verification data without applied Grande cuts, as listed in table 5.1. The accepted events by the self-trigger with a zenith angle $\theta > 70°$ are investigated further. The LOPES$^{\mathrm{STAR}}$ antenna clusters D17 and D30 are investigated separately.
Note: The detected background events are randomly recorded due to the external trigger signal from KASCADE-Grande.

The direction of the source depends only on the azimuth angle, whereas the zenith angle is expected to be horizontal (within the uncertainty of the reconstruction). The absolute azimuth position of the source does not have to be known precisely, but the position of the source has to be constant during the time of measurement. A statistical analysis of the reconstructed azimuth angle results in an estimation of the angular resolution.

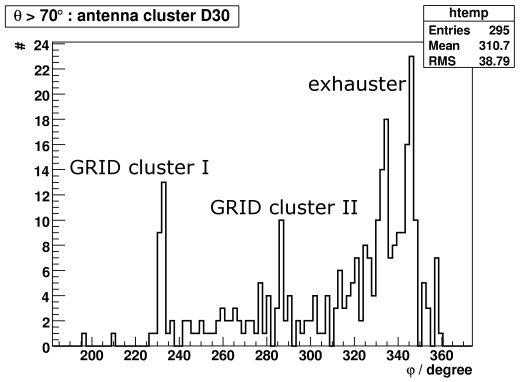

Figure 6.7: The western side of antenna cluster D30 which receives background signals from GRID clusters and their cooling exhauster.

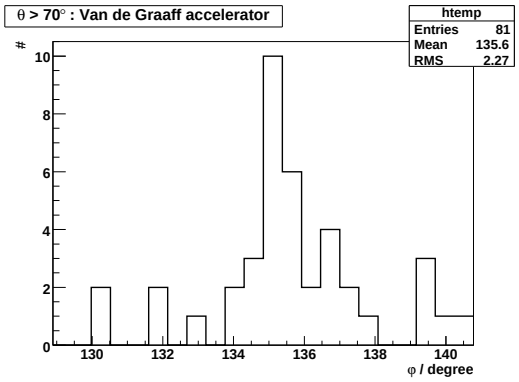

Figure 6.8: Sounding of antenna cluster D30 to a nearby particle experiment with a Van de Graaff accelerator.

This method may be improved, if an artificial transmitter with an adequate arrival direction ($0° \leq \theta < 70°$) is used instead with a distance to the antennas that fulfils far field approximation. On the one hand this allows to optimise the LPDA direction sensitivity related to the arrival direction (high suppression of inclined signals). On the other hand the emitted artificial signal is well understood and the curvature of the signal front is well defined.

antenna cluster D17 Two dominant background sources are detected in these data.

One is the KArlsruher TRItium und Neutrino experiment (KATRIN) in the south-west direction. Fig. 6.5 illustrates this background source from the point of view of the four LPDAs (D17). Three separable sources emitting their signals. The detected directions result in a mean angular resolution of $\Delta\varphi \approx 0.6°$.

The angular resolution is also limited by the dimension of the transmitter source. The area of the KATRIN experiment is located about 150 m away and cover an area of about $100 \times 50\,\mathrm{m}^2$.

The other background source is located about 150 m in the north-west direction of the antenna cluster D17 and covers a small area of about ($125 \times 125\,\mathrm{m}^2$) which is used by an outside company. As pictured in fig. 6.6 the mean azimuth direction corresponds to the direction of this area. The angular resolution results in $\Delta\varphi \approx 0.7°$.

antenna cluster D30 The western side of the cluster is located next to an institute (distance < 25 m) which provides the housing of GRID FZKA[1]. The cooling system of the GRID clusters (exhausters, see fig. 6.7) is located next to the building and is also visible in fig. 3.2 on the upper left hand side. The angular resolution of the two main peaks corresponds to $\Delta\varphi < 1°$ and the exhauster sounding results

[1]Computer cluster which offers online computation or storage in a worldwide sub-network (grid).

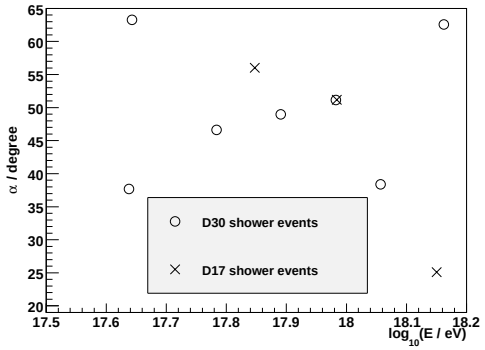

Figure 6.9: Distribution of the geomagnetic angle α versus the primary energy E.

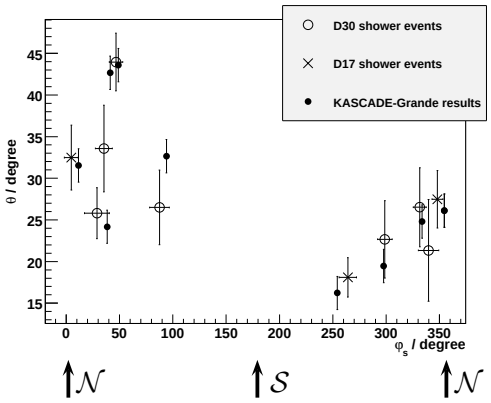

Figure 6.10: Arrival direction of shower events with their reconstructed uncertainties.

in $\Delta\varphi < 2°$. The dimension of the background source is small but the distance is very short.

A nearby particle experiment with a Van de Graaff accelerator is located in the south-west direction of the cluster (about 100 m). The angular resolution is shown in fig. 6.8 and results in $\Delta\varphi \approx 2.3°$. The shape of this distribution points to multiple background sources which might be separated by better statistics. The statistics for that direction sounding is limited, due to the fact that this experiment was shut down during the measurement period of the verification data used.

Results

The comparison of both antenna clusters shows that an angular resolution of $\Delta\varphi \approx 0.6°$ is achievable by using triangulation with signals of three or four antennas. This method does not allow to determine the angular resolution of the zenith angle ($\theta \approx 90°$ within the uncertainties). The chosen simplification of the shower front results in a systematic offset of the reconstructed arrival direction, whereas the angular resolution might reflect the influence of environmental effects on the receiving properties of the LPDA (scattering of the electromagnetic waves and the corresponding delayed receiving times). In fact, if the real shower front of the radio emission of extensive air showers is better understood then the radio technique could easily achieve a more precise resolution of the arrival direction compared to particle detectors.

6.4.2 Geomagnetic Angle and Primary Energy

The 10 radio events accepted by the applied quality cuts show a distribution of the energy and the geomagnetic angle as illustrated in fig. 6.9 for the antenna clusters D17 (×) and D30 (○). The match of both symbols corresponds to the double-detected shower event in antenna cluster D17 & D30.

The geomagnetic angle α is defined as the angle between the magnetic field of the Earth and the shower axis. The shower axis is reconstructed by taking the position of

the shower core and the arrival direction from KASCADE-Grande into account, whereas the geomagnetic field lines point to the south with a zenith angle $\theta \approx 25°$ on the site of the Forschungszentrum Karlsruhe[2] [Maus 05].

The radio signal in the observed polarisations depends on the geomagnetic angle α as described in the geosynchrotron model. In fact, most of the radio signals are observed for $\alpha > 40°$ as a function of the energy of the primary particle. The data shown in figure 6.9 might also hint to the more effective radio observations for higher energies of the primary particles, due to the expected linear increase of the field strength with the energy (geosynchrotron model).

6.4.3 Arrival Direction

The distribution of the arrival directions of showers based on the LOPES$^{\mathrm{STAR}}$ and KASCADE-Grande reconstruction is shown in fig. 6.10. The arrival directions of the detected events from antenna cluster D17 ($\times$) and from D30 ($\circ$) are calculated on the basis of the measured radio signal with the statistical uncertainties from the shower plane fit. The illustrated arrival directions from KASCADE-Grande ($\bullet$) result from the reconstruction of the particle detectors with an uncertainty of $\pm 2°$ for zenith and azimuth direction.

No events are detected arriving from the south due to the orientation of the geomagnetic field ($\varphi = 180°, \theta = 25°$) which is almost in parallel to the shower axis for these directions. For such incidences the contribution to radio emission is small and for low energy particles negligible and not detected by the self-trigger. This confirms that the radio emission of cosmic ray air showers is mainly dominated by a geomagnetic emission mechanism.
Note: Events with $\theta > 45°$ are rejected by the applied Grande cuts.

6.4.4 Golden Events

Fig. 6.1 illustrates the distribution of the shower cores on the ground. In particular, there are two shower events that are detected by all 10 LOPES$^{\mathrm{STAR}}$ antennas which are marks as golden events. The golden event with the mark II was rejected by the reconstruction of KASCADE-Grande due to the inclined zenith angle. A summary of the main characteristics of the selected golden events are given in table 6.3 and are discussed in the following.

Reconstruction of the Shower Core with Radio

The position of the shower cores are reconstructed by KASCADE-Grande. If the shower impact point is within the area covered by the antenna arrays (D17, D19 and D30) then the position of the shower core can be reconstructed on the basis of the radio data. The barycentre of all the measured signals (per antenna: combined north-south & east-west signal) is calculated (see fig. 6.11 and 6.12).

For simplification, it is assumed that the lateral distribution behaves linearly. The resulting position of the shower core can be taken as a starting value for further methods.

[2] On the site of the Pierre Auger Observatory the magnetic field lines pointing to the south with a zenith angle $\theta \approx 55°$

		golden event I	golden event II
energy	$\log_{10}(E/\mathrm{GeV})$	≈ 8.98	≈ 9.44
azimuth angle	$\varphi_{\mathrm{STAR,D17}}/degree$	348 ± 5	129 ± 2
	$\varphi_{\mathrm{STAR,D30}}/degree$	340 ± 10	126 ± 3
	$\bar{\varphi}_{\mathrm{STAR}}/degree$	345 ± 6	128 ± 2
	$\varphi_{\mathrm{Grande}}/degree$	355 ± 2	129 ± 2
zenith angle	$\theta_{\mathrm{STAR,D17}}/degree$	27 ± 3	53 ± 5
	$\theta_{\mathrm{STAR,D30}}/degree$	21 ± 6	64 ± 10
	$\bar{\theta}_{\mathrm{STAR}}/degree$	25 ± 3	57 ± 6
	$\theta_{\mathrm{Grande}}/degree$	26 ± 2	59 ± 2
shower core	$x_{\mathrm{STAR}}/\mathrm{m}$	3 ± 10	-106 ± 5
	$x_{\mathrm{Grande}}/\mathrm{m}$	8 ± 7	-386 ± 7
	$y_{\mathrm{STAR}}/\mathrm{m}$	-327 ± 6	-362 ± 4
	$y_{\mathrm{Grande}}/\mathrm{m}$	-368 ± 7	-392 ± 7
geomagnetic angle	$\alpha/degree$	≈ 51	≈ 46

Table 6.3: Main characteristics of the two golden events.

The barycentre for the x and y coordinate in the reference frame of KASCADE-Grande follows eq. 6.8.

$$x_{\mathrm{bary}} = \frac{\sum_i \left|\vec{E}_i\right| \cdot x_{\mathrm{ant},i}}{\sum_j \left|\vec{E}_j\right|} \qquad y_{\mathrm{bary}} = \frac{\sum_i \left|\vec{E}_i\right| \cdot y_{\mathrm{ant},i}}{\sum_j \left|\vec{E}_j\right|} \tag{6.8}$$

where $\left|\vec{E}\right|$ are the total measured electric field strength (per antenna) and x_{ant} and y_{ant} are the corresponding coordinates of the position in the observation plane.

The indicated error bars in fig. 6.11 and 6.12 correspond to the uncertainty of the measured field strength as a result from the performed calibration. The uncertainty of the absolute field strength have to be taken into account for comparisons with quantities that are measured by different antenna cluster.

The final uncertainties for the calculated barycentres result from Gaussian error propagation by taking into account the error of the absolute field strength and the uncertainty of the antenna position (0.5 m). The uncertainty of the shower core from KASCADE-Grande is fixed at 7 m for the x and y coordinate.

The antenna density of the covered area has an important influence when using this method. If the observed area is not covered with a regular structure then the distributions of the field strength versus the ground position of the antennas is not filled homogeneously. The missing points on the ground mainly increase the uncertainty of the calculated barycentres.

Furthermore, positions of the shower core which are located outside the covered area are shifted inside the antenna array by this method.

golden event I A comparison of the position of the core derived from the reconstruction of KASCADE-Grande with the calculated barycentre gives an estimation of the systematic uncertainties of this method (see fig. 6.11).

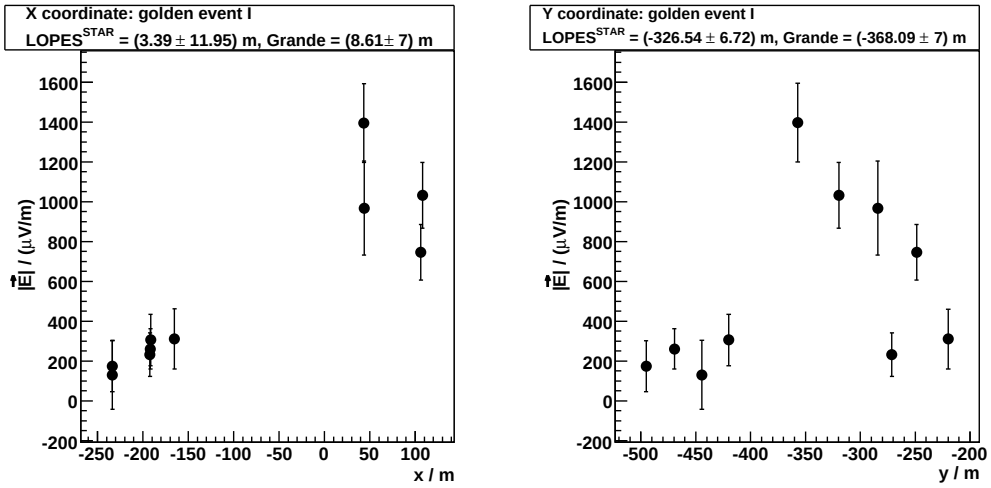

Figure 6.11: Determined position of the shower core on the basis of the recorded radio signal of 10 LOPES$^{\mathrm{STAR}}$ antennas (see fig. 6.1, dashed red circle I).

$$x_{\mathrm{bary,star,I}} = (3 \pm 10)\,\mathrm{m} \qquad y_{\mathrm{bary,star,I}} = (-327 \pm 6)\,\mathrm{m}$$
$$x_{\mathrm{Grande,I}} = (9 \pm 7)\,\mathrm{m} \qquad y_{\mathrm{Grande,I}} = (-368 \pm 7)\,\mathrm{m}$$

The large uncertainty for the x coordinate corresponds to the irregular grid structure of the antenna positions on the ground. The expected position of the shower core is close to one antenna of cluster D17 and the clusters D19 and D30 are located almost at the same x coordinate. Therefore, the distribution of the x coordinate shows an uncovered range around $-100\,\mathrm{m} < x < 25\,\mathrm{m}$ but covers a range of 350 m in total. The results from the x coordinates match within their uncertainties for the LOPES$^{\mathrm{STAR}}$ and KASCADE-Grande reconstruction.

The distribution of the y coordinate covers a range of almost 300 m with the 10 LOPES$^{\mathrm{STAR}}$ antennas. The resulting position of the shower core has an uncertainty in the range of the uncertainty of KASCADE-Grande. The relative deviation of both reconstructions of the y coordinate is less then 12 %.

golden event II The second selected golden event as shown in fig. 6.12 was rejected by the Grande cuts ($\theta < 45°$). The reconstruction of KASCADE-Grande showed that N_μ and N_e are determined with a large uncertainty (needed for an estimation of the energy), but the position of the shower core is precise.

The reconstructed direction from radio results in $\theta_{\mathrm{star}} \approx 58°$ and $\varphi_{\mathrm{star}} = 128°$ and the reconstructed direction of KASCADE-Grande results in $\theta_{\mathrm{Grande}} \approx 59°$ and $\varphi \approx 129°$. A trustable calibration of the radio data can be performed for $\theta \lesssim 60°$ which is fulfilled for that shower event.

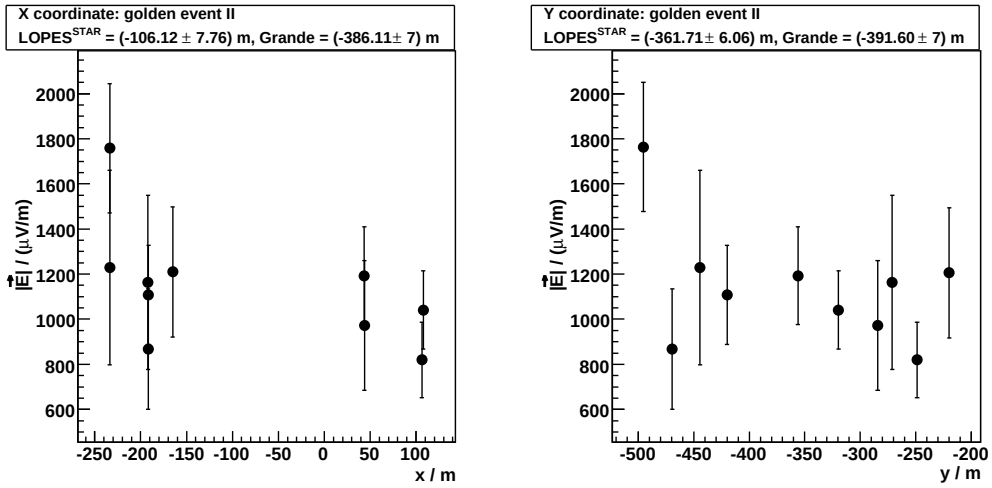

Figure 6.12: Determined position of the shower core on the basis of the recorded radio signal of 10 LOPES$^{\mathrm{STAR}}$ antennas (see fig. 6.1, dashed red circle II).

$$x_{\mathrm{bary,star,II}} = (-106 \pm 5)\,\mathrm{m} \qquad y_{\mathrm{bary,star,II}} = (-362 \pm 4)\,\mathrm{m}$$
$$x_{\mathrm{Grande,II}} = (-386 \pm 7)\,\mathrm{m} \qquad y_{\mathrm{Grande,II}} = (-392 \pm 7)\,\mathrm{m}$$

The barycentre for the x coordinate is shifted about 200 m away compared with the result from KASCADE-Grande. The reconstructed direction and position of the shower core are well reconstructed by KASCADE-Grande for that particular shower event. The real position of the shower core was located outside the area covered by the antennas and shifted toward this area.

The reconstruction of the y coordinate differs less then 7 %.

Results

The comparison of the calculated positions of the shower core from LOPES$^{\mathrm{STAR}}$ and KASCADE-Grande showed that this method works reasonable as a first (fast) guess, which was also shown by other experiments [Ardo 06].

The disadvantage of this method results from the assumption that the real impact point of the shower core has to be located inside the covered area. Otherwise the method itself will shift the position of the core by an unknown factor inside the observed area. Furthermore, the barycentre method assumes a linear decrease of the lateral distribution of the radio emission, which is not fulfilled (see next paragraph). If the lateral distribution function is experimentally determined then this method might be improved by fitting the distribution directly.

Lateral Distribution

The two golden events were selected to investigate the Lateral Distribution Function (LDF) in more detail. In this context the LDF is defined by the dependence on the

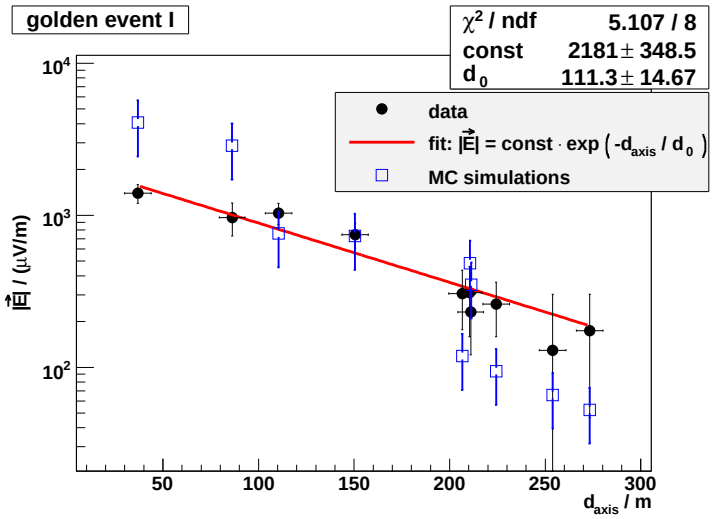

Figure 6.13: The lateral distribution functions (LDF) of the golden event I: Measured data (black dots), applied fit (red line), and MC simulations (blue squares).

detected peak height of the radio pulse versus the distance of the antennas to the shower axis. An exponential decrease of the electromagnetic emission of the shower signal by increased distance perpendicular to the shower axis (shower coordinates) is expected from theory as well as from other experimental results [Nehl 08a, Hueg 05b].

The illustrated error bars (fig. 6.13 – 6.18) for the field strength result from the sum of the calibration uncertainties and an estimated influence of the background noise at the individual time samples. The error bars for the perpendicular distance to the shower axis (d_{axis}) result from the error propagation of calculating d_{axis} with the given shower axis and an uncertainty of 7 m (KASCADE-Grande).

The simulated shower events, presented here, are calculated with REAS2 [Hueg 07]. The Monte Carlo (MC) radio simulation uses the particle MC simulation tool CORSIKA [Heck 98] for the electron & positron distributions and determines the radio emission by calculating the geosynchrotron emission from the charged particles in the air shower.

The quantities of the reconstruction of KASCADE-Grande and a typical uncertainty of the energy of $\frac{\sigma_E}{E} \approx 40\,\%$ is taken into account for the radio simulations. With respect to shower-to-shower fluctuations, 150 shower profiles assuming primary protons were calculated. Out of these profiles a typical shower event was selected for the comparisons with the golden events [Hueg 08].

golden event I The lateral distribution of the golden event I is illustrated in fig. 6.13 (black dots). The antenna signal corresponds to the absolutely calibrated and combined signal of the north-south & east-west polarised component (per antenna). A fit of an exponential decrease of the radio emission with increasing distance to the shower axis d_{axis} results in a scale parameter $d_{0,\text{I}} = (116.6 \pm 12.3)\,\text{m}$ (solid red curve).

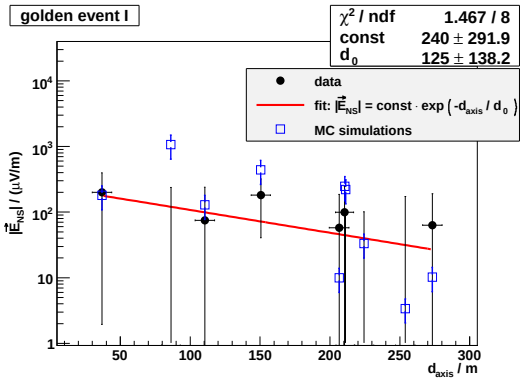

Figure 6.14: LDF for the north-south polarised component (black dots) with an MC shower simulation (blue squares) and an exponential fit to the data (red line).

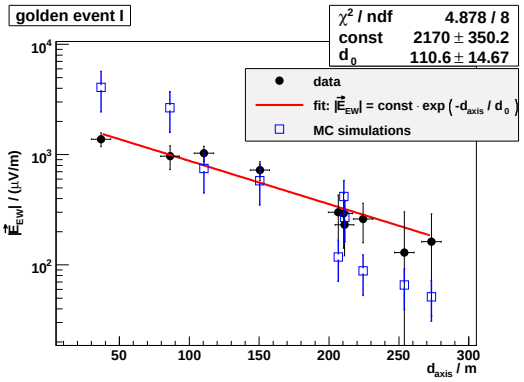

Figure 6.15: East-west polarisation: LDF for a selected event (black dots) as well as the corresponding MC simulation (blue squares) and an exponential fit (red line).

Additionally, an MC simulation for a typical shower event is pictured (blue squares). In the range close to the shower axis ($d_{\text{axis}} < 100\,\text{m}$) the simulation seems to overestimate the measured signal. The simulation within the range of $100\,\text{m} < d_{\text{axis}} < 210\,\text{m}$ matches the measured data within their uncertainties, whereas the simulation significantly differs for $d_{\text{axis}} > 210\,\text{m}$.

Fig. 6.14 shows the signal of the north-south polarised component versus the distance to the shower axis (d_{axis}) as well as fig. 6.15 for the signal of the east-west polarised component (black dots). The applied exponential fit is pictured with the solid red line and results in a scale parameter of $d_{0,\text{I,NS}} = (128.6 \pm 94.6)\,\text{m}$ and $d_{0,\text{I,ES}} = (115.8 \pm 12.3)\,\text{m}$, respectively.

Most of the radio emission is expected to be detected in the east-west polarisation due to the arrival direction ($\varphi \approx 355°$ and $\theta \approx 26°$) and the resulting geomagnetic angle $\alpha \approx 46°$. The data and simulations illustrated for the north-south polarisation (see fig. 6.14) and the east-west polarisation (see fig. 6.15) confirm this assumption.

The differences between the data and the simulations (east-west) behave very similarly as the combined signal of both polarisations, due to the dominant signal in this polarisation, whereas the distribution of the signal in the north-south polarisation is very low for the measured and simulated antenna positions. Furthermore, the radio pulses measured in the north-south channel differs by a factor of 10 from the signals in the east-west channel and is reproduced by the simulations. This result again confirms the geosynchrotron model.

golden event II Shower event II was rejected by the Grande cuts. A detailed analysis of the full reconstruction of this event points out that the reconstructed position and arrival direction is trustable but the estimated energy based on the muon and electron number might be wrong. A falsely reconstructed energy results only in a proportional factor (shift) of the simulated field strength, due to the fact that

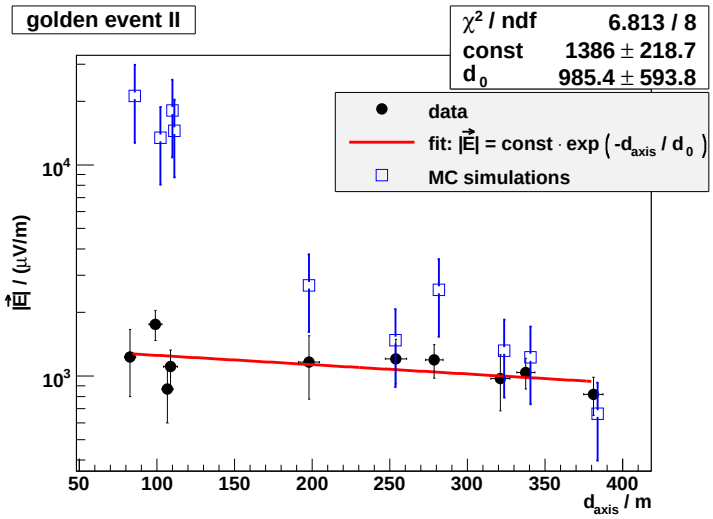

Figure 6.16: The lateral distribution functions (LDF) of the golden event II: Measured data (black dots), applied fit (red line), and MC simulations (blue squares).

the radio emission of the primary particle scales linearly with the primary energy $\left(|\vec{E}| \propto \left(\frac{E}{10^{17}\,\mathrm{eV}}\right)^{\approx 1}\right.$ parametrisation of the radio emission, see eq. 2.1$\left.\right)$.
Note: No shift to the simulated field strength was applied for the comparison of the measured and simulated data for any golden event.

The lateral distribution of the combined polarisation signals are illustrated in fig. 6.16 (black dots). The scale parameter $d_{0,\mathrm{II}}$ from the exponential fit results in $d_{0,\mathrm{II}} = (985 \pm 594)\,\mathrm{m}$. The lateral distribution for each measured signal per polarisation is shown in fig. 6.17 and fig. 6.18, respectively.

The scale parameters per polarisation result in $d_{0,\mathrm{II,NS}} = (912 \pm 534)\,\mathrm{m}$ and $d_{0,\mathrm{II,EW}} \approx (4600 \pm 4 \cdot 10^4)\,\mathrm{m}$. The results of the fit from $d_{0,\mathrm{II,EW}}$ are misleading due to the low received signal in the east-west polarisation. The large uncertainties of the scale parameter of all three fits are due to the positions of the antennas in relation to the position of the shower core. The fit is applied to data that correspond to the tail of the exponential function and the uncertainty increases.

Additionally, a comparison with the MC simulation is illustrated (blue squares). Most of the simulated and measured data points match within their uncertainties for $d_{\mathrm{axis}} > 200\,\mathrm{m}$. It seems that the simulation overestimates the shower signals close to the shower axis ($d_{\mathrm{axis}} < 120\,\mathrm{m}$) for the combined signal and per polarised component measured as well.

The golden event II was reconstructed with a arrival direction of $\varphi \approx 129°$ and $\theta \approx 60°$. Due to the reconstructed azimuth angle the main part of the shower signal is expected to be measured in the north-south polarised component and corresponds to fig. 6.17 and fig. 6.18, respectively. The correspondence between the measured data and the simulations confirms again the assumption of the geosynchrotron model.

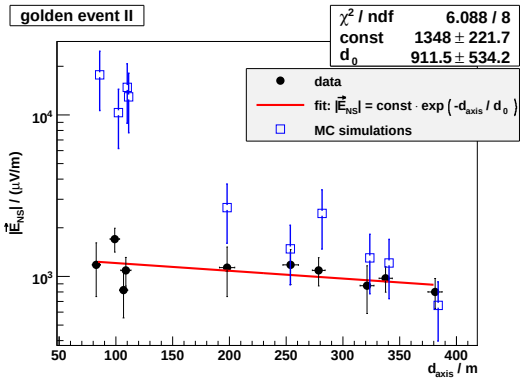

Figure 6.17: LDF for the north-south polarised component (black dots) with an MC shower simulation (blue squares) and an exponential fit to the data (red line)

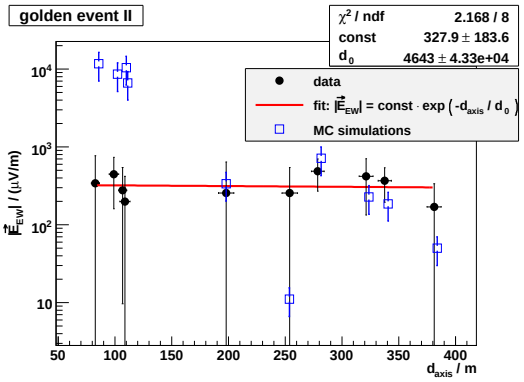

Figure 6.18: East-west polarisation: LDF for a selected event (black dots) as well as the corresponding MC simulation (blue squares) and an exponential fit (red line).

Results

An area of about $300 \times 350\,\mathrm{m}^2$ is covered by the LOPES$^{\mathrm{STAR}}$ antenna clusters to investigate lateral distributions. The industrial environment on the site of the Forschungszentrum Karlsruhe defines possible antenna positions, which does not allow an installation on a regular grid. An estimation of the effective area of the three antenna clusters of LOPES$^{\mathrm{STAR}}$ on the basis of the distribution of detected and well-reconstructed shower events results in $600 \times 800\,\mathrm{m}^2$.

The three LOPES$^{\mathrm{STAR}}$ antenna clusters recorded one golden event, which was accepted by the self-trigger as well as by the Grande cuts. The comparison of simulations with measured signals of the total field strength as well as of each polarisation differs significantly. Antenna signals close to the shower axis are overestimated by the simulations. This effect seems to increase with increasing zenith angle. The mean scale parameter d_0 results in $d_{0,\mathrm{I}} = (116 \pm 12)\,\mathrm{m}$ for zenith angle $< 40°$.

A second selected golden event was accepted by the self-trigger and rejected by the Grande cuts due to the inclined arrival direction ($\theta \approx 60°$). Simulated shower signals close to the shower axis are again overestimated compared with the measured data. The mean scale parameter d_0 results in a very large value with an uncertainty of more than 56 %. Past investigations showed significantly differences between measured signals and simulated signals with REAS2 [Nehl 08a].

More shower events with observed signals in the north-south & east-west polarisation are needed to improve the verification of the MC simulations. The comparison of the measured signals with the simulation results in a good correspondence at lateral distances of about 50 m to 350 m and helps to improve the understanding of the radio emission of extensive air showers.

6.5 Results

Ten radio events are finally accepted by all the quality cuts applied to the reconstruction of KASCADE-Grande and LOPES$^{\mathrm{STAR}}$ and are used for the analysis.

The reconstruction of the arrival direction in this thesis is based on the assumption of a planar shower front. The point in time of the detected radio pulse is determined with a constant fraction method of half the height.

A challenge is to parametrise the observed radio emission of high energy cosmic rays. LOPES$^{\mathrm{STAR}}$ records the north-south & east-west polarised component of the electric field and thereby obtains a more precise measurement of the emitted signal compared with previous experiments.

In a first step a parametrisation to verify pervious approaches was tried out without success, due to the low event statistics and limited measurement period.

In a next step the measured total field strength with the combined polarised signals was parametrised. The best parametrisation and its fit take the dependence on the geomagnetic angle α as $(1 - \sin(\alpha))$ into account and disregard the dependence on the zenith angle θ and result in a scale parameter $d_0 = (137 \pm 18)\,\mathrm{m}$. These results have to be proven by an analysis of the ongoing measurements of LOPES$^{\mathrm{STAR}}$ and KASCADE-Grande.

LOPES$^{\mathrm{STAR}}$ achieves an angular resolution of about $\Delta\varphi \approx \Delta\theta \approx 7^\circ$ with a systematic offset of about $\Delta\varphi \approx 2^\circ$ and $\Delta\theta \approx -1^\circ$ on the basis of the observed shower events. The uncertainty and the offset are dominated by the assumption of a planar shower front and the limited number of antennas.

A second method to estimate the angular resolution by triangulation with such a detector is based on rejected and highly inclined background events ($\theta \approx 90^\circ$) from locally fixed sources (e.g. machines, working grounds). Assuming additionally that the absolute position and the exact shape of the signal front is constant for the time of measurement, LOPES$^{\mathrm{STAR}}$ achieves an angular resolution of $\Delta\varphi \approx 0.6^\circ$.

The selected radio events verify the expectation of the geosynchrotron model that less shower events are expected from an arrival direction of the south, due to the direction of the geomagnetic field on the site of the Forschungszentrum Karlsruhe.

A reconstruction of the position of the shower core on the basis of the radio data is possible by calculating the barycentre with the measured signals on the ground. The method is limited by the sensitive area of the detector and will produce false positions if the real position of the shower core is located outside the equipped area.

Two shower events are recorded by all 10 LPDAs and are selected for an investigation of the lateral distribution and a comparison with their Monte Carlo simulations. The analysis showed that the measured signals are qualitatively reproduces by the simulations. Signals close to the shower axis are overestimated. A further comparison of each signal (north-south and east-west polarised component) with the simulated signal (per polarisation) additionally verifies the geosynchrotron model.

Chapter 7

Summary and Outlook

LOPES$^{\mathrm{STAR}}$ is a prototype detector for future experiments including a trigger system on the observation of radio emission of ultra-high energy cosmic rays. Absolutely calibrated measurements of the north-south & east-west polarised components of the electric field in combination with well-established particle detectors were performed.

An installation of 10 logarithmic-periodic dipole antennas has been set-up on the site of the Forschungszentrum Karlsruhe in Germany and inside the area of the KASCADE-Grande experiment to observe the north-south and east-west polarisation in parallel. An external trigger signal starts the data acquisition of LOPES$^{\mathrm{STAR}}$ for cosmic rays with an energy of $E > 10^{16}\,\mathrm{eV}$.

Furthermore, three additional antennas were installed on the site of the Pierre Auger Observatory in Argentina to investigate the environmental conditions and the background influences on the system. On the site of the Pierre Auger Observatory the amplitude in the noise spectrum is one order of magnitude lower than on the site of the Forschungszentrum Karlsruhe which is dominated by an industrial character of this area. The site of the Pierre Auger Observatory is forseen for a large-scale antenna array in order to observe radio emission of the ultra-high energy cosmic rays in the near future.

The presented results are based on background investigations in the framework of the Pierre Auger Observatory as well as on the coincident measurements of LOPES$^{\mathrm{STAR}}$ and KASCADE-Grande. The radio emission of cosmic rays was observed in a frequency range of $40-80\,\mathrm{MHz}$ by logarithmic-periodic dipole antennas, whereas the KASCADE-Grande experiment measures the secondary particles of extensive air showers. The developed methods and algorithms in the context of the calibration, the trigger system, and the data analysis are now standard tools for the analysis of radio pulses in air shower (e.g. in the LOPES collaboration) and can be transferred to future experiments.

The detector system used is absolutely calibrated and cross-checked by applying two different calibration procedures. On the one hand precise laboratory measurements of each component used in the signal chain were performed and combined with the characteristics of the cables used to describe the experimental configuration (Step-by-Step method). On the other hand an external reference source was used to emit a well-defined electric field, which was received by the LOPES$^{\mathrm{STAR}}$ antennas, manipulated by the complete signal chain, and finally stored on hard disc (End-to-End method).

A detailed comparison showed that the frequency dependent calibration constants match for both methods within their uncertainties of about 30 %. The total uncertainty of the measured field strength results in $\sigma_{|\vec{E}|} = 7.2\,\%$ for LOPES$^{\mathrm{STAR}}$ by the Step-by-Step method.

The background conditions on the site of the Forschungszentrum Karlsruhe are dominated by transient signals and radio frequency interferences. The presented self-trigger

sufficiently suppresses these background signals on each channel (polarisation) per antenna. The chosen parameters to describe the signals are plausibly motivated and are easy to extend. The accepted radio emission signals and shower-like background signals in each channel are further analysed by a so-called cluster trigger. It rejects highly inclined and coincident man-made signals (zenith angle $\theta > 60°$) and rejects all the non-coincident events as well.

The resulting purity (6 %), efficiency (90 %) and rejection (99.9 %) prove that the trigger system rejects background signals per channel and cluster in a sufficient way. The achieved (false) trigger rates at the Forschungszentrum Karlsruhe will decrease on the site of the Pierre Auger Observatory due to the one order of magnitude better background conditions. In addition, the power per polarisation received is proportional to E^2 described by the geosynchrotron model and the trigger efficiency quadratically increases with increasing energy of the primary particle.

The proof-of-principle of the self-trigger system is obtained by the presented studies. The event statistics is restricted to events with an energy of $E \leq 10^{18}\,\mathrm{eV}$, due to the area covered by KASCADE-Grande ($700 \times 700\,\mathrm{m}^2$) and to the limited time of measurement for with the actual LOPES$^{\mathrm{STAR}}$ configuration. The observed energy range of the Pierre Auger Observatory makes the site in Argentina attractive for the future ($E > 10^{18}\,\mathrm{eV}$).

An existing hardware with a digital signal processor and a programmable logical hardware is re-used to implement a prototype version of the discussed self-trigger system. The optimised implementation of the trigger algorithms are in progress and first measurements to verify the strategy are planned on the site of the Forschungszentrum Karlsruhe for autumn 2008. In a next step measurements on the site of the Pierre Auger Observatory with three antennas are planned for late 2008. The hardware based prototype self-trigger has to prove the experimental practicability under environmental conditions of the two sites.

Quality cuts are applied to the reconstruction of KASCADE-Grande and LOPES$^{\mathrm{STAR}}$ to select well reconstructed shower events. Ten radio events are finally accepted by all the quality cuts and are used for further investigations.

The received radio pulse is correlated to the combined peak values of the north-south & east-west polarised component. A parametrisation of the radio emission depending on the geomagnetic angle α, the energy of the primary particle E, and the scale parameter d_0 was performed. The best fit results in a scale parameter of $d_0 = (137 \pm 18)\,\mathrm{m}$ and a linear dependence on the primary energy E.

The achieved angular resolution of the azimuth angle φ and the zenith angle θ results in $\Delta\varphi \approx \Delta\theta \approx 7°$ with a systematic offset of $\Delta\varphi \approx 2°$ and $\Delta\theta \approx -1°$ on the basis of the selected shower events. The uncertainty and the offset are dominated by the assumption of a planar shower front.

A second independent method is used to calculate the angular resolution. The resolution was estimated on the basis of rejected and highly inclined background events ($\theta \approx 90°$) from locally fixed sources (e.g. machines, working grounds). In addition, it is assumed that the absolute position and the exact shape of the signal front are constant for the time of measurement. The investigations show that LOPES$^{\mathrm{STAR}}$ achieves an angular resolution of $\Delta\varphi \approx 0.6°$.

The selected shower events fulfil all the quality cuts and verify the expectation of the geosynchrotron model that less shower events are observed from southern arrival direc-

tions, due to the orientation of the geomagnetic field on the site of the Forschungszentrum Karlsruhe.

Two events are observed from all 10 LOPES$^{\mathrm{STAR}}$ antennas and are used to investigate the lateral distribution on an event-by-event basis and for a detailed comparison with Monte Carlo simulations. The lateral distribution is defined by the dependence on the detected peak height of the radio pulse versus the distance of the antennas to the shower axis. The analysis showed that the measured signal is qualitatively reproduced, except antennas close to the shoer axis were overestimated. Nevertheless, this investigation confirms the geosynchrotron model. The second shower event is highly inclined and the correlation is not significant.

LOPES$^{\mathrm{STAR}}$ is an absolutely calibrated detector to observe the radio emission of cosmic rays. The presented self-trigger system rejects transient signals as well as radio frequency interferences and accepts the radio signals from extensive air showers. Thus, LOPES$^{\mathrm{STAR}}$ is an important building block on the path to the upcoming antenna array of a few tens of km^2. This is necessary in order to understand in more detail the effect of the radio emission of cosmic rays and their correlation with the parameters of the air shower. The presented results are used in the planned radio detector within the framework of the Pierre Auger Observatory and will contribute to verify the geosynchrotron model of extensive air showers at energies above 10^{18} eV.

List of Figures

List of Tables

Bibliography

[Abra 04] J. Abraham *et al.* "Properties and performance of the prototype instrument for the Pierre Auger Observatory". *Nuclear Instruments and Methods A*, Vol. 523, pp. 50–95, 2004.

[Agli 93] M. Aglietta *et al.* "UHE cosmic ray event reconstruction by the electromagnetic detector of EAS-TOP". *Nuclear Instruments and Methods A*, Vol. 336, pp. 310–321, 1993.

[Alla 71] H. R. Allan. "Radio Emission from Extensive Air Showers". *Progress in Elementary Partition and Cosmic Ray Physics*, Vol. 10, p. 171, 1971.

[Anto 03] T. Antoni *et al.* "The Cosmic-Ray Experiment KASCADE". *Nuclear Instruments and Methods A*, Vol. 513, p. 490, 2003.

[Ardo 05] D. Ardouin *et al.* "Radio-Detection Signature of High Energy Cosmic Rays by the CODALEMA Experiment". *Nuclear Instruments and Methods in Physics Research Section A*, Vol. 555, p. 148, 2005.

[Ardo 06] D. Ardouin *et al.* "Radioelectric Field Features of Extensive Air Showers Observed with CODALEMA". *Astroparticle Physics*, Vol. 26, p. 341, 2006.

[Asch 07] T. Asch *et al.* "Trigger Strategy for Radio Detection of Atmospheric Air Showers with LOPES$^{\mathrm{STAR}}$". *Proc. 30th ICRC*, No. 923, 2007.

[Aska 62] G. A. Askaryan. "Excess Negative Charge of an Electron-Photon Shower And Its Coherent Radio Emission". *Soviet Physics: Journal of Experimental and Theoretical Physics*, Vol. 14, pp. 441–443, 1962.

[Aska 65] G. A. Askaryan. "Coherent Radio Emission from Cosmic Showers in air and in dense Media". *Soviet Physics JETP*, Vol. 21, p. 658, 1965.

[Auge 39] P. Auger *et al.* "Extensive Cosmic-Ray Showers". *Review of Modern Physics*, Vol. 11, No. 3-4, pp. 288–291, 1939.

[Baeh 08] L. Baehren. 2008. private communication.

[Bier 87] P. L. Biermann and P. A. Strittmatter. "Synchrotron emission from shock waves in active galactic nuclei". *Astrophysical Journal*, Vol. 322, pp. 643–649, 1987.

[Bird 93] D. J. Bird *et al.* "Evidence for correlated changes in the spectrum and composition of cosmic rays at extremely high energies". *Physical Review Letters*, Vol. 71, No. 21, pp. 3401–3404, 1993.

[Blue 03] J. Bluemer *et al.* "Cosmic rays at the highest energies and the Pierre Auger Observatory". *Journal of Physics G: Nuclear and Particle Physics*, Vol. 29, pp. 867–79, 2003.

[Brac 00] R. N. Bracewell. *The Fourier transform and its applications.* Ronald N. Bracewell. Boston : McGraw Hill, 2000.

[Brun 97] R. Brun and F. Rademakers. "ROOT - An Object Oriented Data Analysis Framework". *Nuclear Instruments and Methods in Physics Research Section A*, Vol. 389, pp. 81–86, 1997.

[Buit 07] S. Buitink *et al.* "Amplified radio emission from cosmic ray air showers in thunderstorms". *Astronomy and Astrophysics*, Vol. 467, No. 2, pp. 385–394, 2007.

[Cand 02] J. Candia *et al.* "Turbulent diffusion and drift in galactic magnetic fields and the explanation of the knee in the cosmic ray spectrum". *Journal of High Energy Physics*, Vol. 12, pp. 033–033, 2002.

[Coss 08] F. Cossavella. 2008. private communication.

[Falc 03] H. Falcke and P. W. Gorham. "Detecting Radio Emission from Cosmic Ray Air Showers and Neutrino with a Digital Radio Telescope". *Astroparticle Physics*, Vol. 19, p. 477, 2003.

[Falc 05] H. Falcke *et al.* "Detection and imaging of atmospheric radio flashes from cosmic ray air showers". *Nature*, Vol. 435, pp. 313–316, 2005.

[Ferm 49] E. Fermi. "On the Origin of the Cosmic Radiation". *Physical Review*, Vol. 75, No. 8, pp. 1169–1174, 1949.

[Frig 05] M. Frigo and S. G. Johnson. "The Design and Implementation of FFTW3". *Proceedings of the IEEE*, Vol. 93, No. 2, pp. 216–231, 2005.

[Gais 77] T. K. Gaisser and A. M. Hillas. *Proceedings of the 15th ICRC*, Vol. 8, p. 353, 1977.

[Gemm 06] H. Gemmeke *et al.* "Advanced detection methods of radio signals from cosmic rays for KASCADE-Grande and Auger". *International Journal of Modern Physics A*, Vol. 21, p. 242, 2006.

[Grei 56] K. Greisen. *Progress in Cosmic Ray Physics*, Vol. 3, 1956.

[Grei 66] K. Greisen. "End to the Cosmic-Ray Spectrum? ". *Physical Review Letters*, Vol. 16, No. 17, pp. 748–750, 1966.

[Hake 06] A. Hakenjos. *Kalibration eines astronomischen Radioantennenfeldes durch eine externe Quelle.* Master's thesis, IK, Froschungszentrum Karlsruhe, 2006.

[Haun 03a] A. Haungs *et al.* "Energy spectrum and mass composition of high-energy cosmic rays". *Reports on Progress in Physics*, Vol. 66, No. 7, pp. 1145–1206, 2003.

[Haun 03b] A. Haungs *et al.* "The KASCADE-Grande Experiment". *Proc. 28th ICRC*, 2003.

[Haze 69] W. E. Hazen *et al.* "Polarization of Radio Pulses from Extensive Air Showers". *Physical Review Letters*, Vol. 22, No. 1, pp. 35–37, 1969.

[Heck 98] D. Heck *et al.* "CORSIKA: a Monte Carlo code to simulate extensive air showers". *FZKA Report 6019*, 1998.

[Heit 49] W. Heitler. "Theory of Meson Production". *Review of Modern Physics*, Vol. 21, No. 1, pp. 113–121, 1949.

[Hess 12] V. F. Hess. "Über Beobachtungen der durchdringenden Strahlung bei sieben Freiballonfahrten". *Physikalische Zeitschrift*, Vol. 13, pp. 1084–1091, 1912.

[Horn 06] A. Horneffer. *Measuring Radio Emission from Cosmic Ray Air Showers with a Digital Radio Telescope.* PhD thesis, University Bonn, 2006.

[Hueg 05a] T. Huege and H. Falcke. "Radio emission from cosmic ray air showers". *Astronomy and Astrophysics*, Vol. 430, No. 3, pp. 779–798, 2005.

[Hueg 05b] T. Huege and H. Falcke. "Radio emission from cosmic ray air showers: Simulation results and parametrization". *Astroparticle Physics*, Vol. 24, pp. 116–136, 2005.

[Hueg 07] T. Huege *et al.* "Monte Carlo simulations of geosynchrotron radio emission from CORSIKA-simulated air showers". *Astroparticle Physics*, Vol. 27, pp. 392–405, 2007.

[Hueg 08] T. Huege. 2008. private communication.

[Jell 65] J. V. Jelly *et al.* "Radio Pulses from Extensive Cosmic-Ray Air Showers". *Nature*, Vol. 205, pp. 327–328, 1965.

[Kahn 66] F. D. Kahn and I. Lerche. "Radiation from Cosmic Ray Air Showers". *Proceedings of the Royal Society of London. Series A*, Vol. 289, No. 1417, pp. 206–213, 1966.

[Kalm 06] N. Kalmykov *et al.* "EAS radio emission characteristics in the framework of the excess charge and synchrotron mechanisms". *Nuclear Physics B*, Vol. 151, pp. 347–350, 2006.

[Kama 58] K. Kamata and J. Nishimura. "The Lateral and the Angular Structure Functions of Electron Showers". *Progress of Theoretical Physics Supplements*, Vol. 6, pp. 93–155, 1958.

[Krom 08] O. Krömer. *Empfangssystem zur Radioobservation hochenergetischer kosmischer Schauer und sein Verhalten bei Selbsttriggerung.* PhD thesis, University Karlsruhe, 2008.

[Kuli 59] G. Kulikov and G. Khristiansen. "On the Size Spectrum of Extensive Air Showers". *Soviet Physics JETP*, Vol. 35, p. 441, 1959.

[Marc 05] D. D. Marco and T. Stanev. "On the shape of the ultrahigh energy cosmic ray spectrum". *Physical Review D*, Vol. 72, No. 8, p. 081301, 2005.

[Maus 05] S. Maus and S. Macmillan. "10th Generation International Geomagnetic Reference Field". *EOS Transactions*, Vol. 86, pp. 159–159, 2005.

[Moli 47] G. Molière. "Therorie der Streuung schneller geladener Teilchen I. Einzelstreuung am abgeschirmten Coulomb-Feld". *Zeitschrift für Naturforschung*, Vol. 2a, 1947.

[Moli 48] G. Molière. "Theorie der Streuung schneller geladener Teilchen II. Mehrfach- und Vielfachstreuung". *Zeitschrift für Naturforschung*, Vol. 3a, 1948.

[Nava 04] G. Navarra *et al.* "KASCADE-Grande: a large acceptance, high-resolution cosmic-ray detector up to 10^{18} eV". *Nuclear Instruments and Methods A*, Vol. 518, pp. 207–209, 2004.

[Nehl 08a] S. Nehls. *Calibrated Measurements of the Radio Emission of Cosmic Ray Air Showers.* PhD thesis, University Karlsruhe, 2008.

[Nehl 08b] S. Nehls *et al.* "Amplitude calibration of a digital radio antenna array for measuring cosmic ray air showers". *Nuclear Instruments and Methods in Physics Research Section A*, Vol. 589, pp. 350–361, 2008.

[Nerl 05] F. Nerling. *Description of Cherenkov light production in extensive air showers.* PhD thesis, University Karlsruhe, 2005.

[Nigl 08] A. Nigl *et al.* "Direction identification in radio images of cosmic-ray air showers detected with LOPES and KASCADE". *Astronomy and Astrophysics*, Vol. 487, No. 2, pp. 781–788, 2008.

[Nutt 81] A. Nuttall. "Some windows with very good sidelobe behaviour". *Acoustics, Speech, and Signal Processing, IEEE Transactions on*, Vol. 29, No. 1, pp. 84–91, 1981.

[Nyqu 02] H. Nyquist. "Certain Topics in Telegraph Transmission Theory". *Proc. IEEE*, Vol. 90, No. 2, 2002.

[Penz 65] A. A. Penzias and R. W. Wilson. "A Measurement of Excess Antenna Temperature at 4080 Mc/s.". *Astrophysical Journal*, Vol. 142, pp. 419–421, 1965.

[Petr 07] J. Petrovic *et al.* "Radio emission of highly inclined cosmic ray air showers measured with LOPES". *Astronomy and Astrophysics*, Vol. 462, No. 1, pp. 389–395, 2007.

[Pier 07] F. D. Pierro. *Measurement of particle energy above 10^{16} eV: technique and uncertainties of the cosmic ray experiment KASCADE-Grande.* PhD thesis, Politecnico di Torino, 2007.

[Ptus 05] V. S. Ptuskin and V. N. Zirakashvili. "On the spectrum of high-energy cosmic rays produced by supernova remnants in the presence of strong cosmic-ray streaming instability and wave dissipation". *Astronomy and Astrophysics*, Vol. 429, No. 3, pp. 755–765, 2005.

[Rohl 04] K. Rohlfs and T. L. Wilson. *Tools of Radio Astronomy.* Springer, 2004.

[Roth 02] K. Rothammel and A. Krischke. *Rothammels Antennenbuch.* DARC, 2002.

[Roth 05] M. Roth *et al. Offline Reference Manual, SD Reconstruction.* 2005. Auger internal note.

[Scho 08] O. Scholten *et al.* "A Macroscopic Description of Coherent Geo-Magnetic Radiation from Cosmic Ray Air Showers". *Astroparticle Physics*, Vol. 29, pp. 94–103, 2008.

[Shan 98] C. Shannon. "Communication In The Presence Of Noise". *Proceedings of the IEEE*, Vol. 86, No. 2, pp. 447–457, 1998.

[Sing 07] K. Singh. 2007. private communication.

[Stan 04] T. Stanev. *High Energy Cosmic Rays.* Springer, 2004.

[Ulri 03] H. Ulrich *et al.* "Energy Spectra of Cosmic Rays in the Knee region". *Nuclear Physics B Proceedings Supplements*, Vol. 122, pp. 218–221, 2003.

[Week 01] T. C. Weekes. "Radio pulses from cosmic ray air showers". *American Institute of Physics, First international workshop on the radio detection of high energy particles*, Vol. 579, No. 1, pp. 3–13, 2001.

[Womm 07] M. Wommer. *Bestimmung des Energiespektrums und der mittleren Masse kosmischer Strahlung mit dem KASCADE-Grande-Experiment.* Master's thesis, IK & IEKP, Forschungszentrum Karlsruhe, 2007.

[Zats 66] G. Zatsepin and V. Kuz'min. "Upper Limit of the Spectrum of Cosmic Rays". *Journal of Experimental and Theoretical Physics Letters*, Vol. 4, p. 78ff, 1966.

Acknowledgements

The work of the last three years for this thesis cannot possibly be handled by one person alone. Many people contributed to the final version of this dissertation.

I express my gratitude towards Prof. Dr. Hartmut Gemmeke for giving me the opportunity to write my dissertation at the Institute of Data Processing and Electronics at the Forschungszentrum Karlsruhe. I thank him for supervising my thesis, for the discussions, and his support during my work. I am also thankful to Prof. Dr. Johannes Blümer, who accepted the co-supervision of this dissertation.

I thank everybody of the LOPES and the Pierre Auger collaboration for great teamwork and the support in many different ways. I would especially like to thank Dr. Andreas Haungs and all the people of the KASCADE-Grande collaboration for being able to use the reconstruction of KASCADE-Grande and for the external trigger used. Furthermore, I thank Dr. Tim Huege for helpful discussions and the performed shower simulations.

In addition, I thank my colleagues Dietmar Bormann, Lars Petzold and Adrian Schmidt for discussions and support in electronics. I am also thankful to everybody of the Institute of Data Processing and Electronics for the nice coffee breaks.

I would like to thank my family and especially Eva Bettini for their friendly words and help, as well as Karin van der Wijst and Mario Bettini.

The list of people that additionally should be mentioned is far too long and so I only say: **Thank you**.